Structural characterization of recombinant fibrillar human Islet Amyloid Polypeptide by solid-state Nuclear Magnetic Resonance Spectroscopy

Inaugural-Dissertation

zur Erlangung des Doktorgrades
der Mathematisch-Naturwissenschaftlichen Fakultät
der Heinrich-Heine-Universität Düsseldorf

vorgelegt von

Franziska Weirich
aus Aachen

Düsseldorf, Juli 2017

aus dem Institut für Physikalische Biologie
der Heinrich-Heine-Universität Düsseldorf

Gedruckt mit der Genehmigung der
Mathematisch-Naturwissenschaftlichen Fakultät der
Heinrich-Heine-Universität Düsseldorf

Berichterstatter:

1. Prof. Dr. Henrike Heise

2. Dr. Manuel Etzkorn

Tag der mündlichen Prüfung:
13.07.2017

Contents

List of Figures

Zusammenfassung

In der vorliegenden Dissertation wurde die Methode der Festkörper-NMR-Spektroskopie auf eine spezifische Fragestellung aus dem Bereich der Proteinfehlfaltungskrankheiten angewendet. Zu den Krankheiten, die mit der Fehlfaltung von Proteinen zusammenhängen, gehören unter anderem Diabetes Mellitus Typ 2, die Alzheimersche Demenz und die Parkinson-Krankheit. Das gemeinsame Kennzeichen dieser Gruppe von Krankheiten ist die extrazelluläre Ablagerung von fehlgefalteten Proteinen, entweder lokal in einem betroffenen Organ, oder systemisch im ganzen Körper. Der Prozess der Proteinfehlfaltung führt häufig zu der Bildung von unlöslichen, amyloiden Fibrillen. Amyloide Fibrillen, die aus verschiedenen Proteinen gebildet wurden, weisen eine geordnete, repetitive Struktur auf, die einen hohen Anteil an β-Sekundärstruktur hat. Die Aufklärung der Fibrillenstrukturen verschiedener Proteine auf molekularer Ebene ist einer der Forschungsschwerpunkte im Rahmen der Erforschung der Proteinfehlfaltungskrankheiten.

Das Thema der vorliegenden Dissertation war die Untersuchung der Struktur von fibrillärem Amylin, oder auch Islet-Amyloid-Polypeptid (IAPP), mittels Festkörper-NMR-Spektroskopie. IAPP besteht aus 37 Aminosäureresten und wird zusammen mit Insulin von den β-Zellen der Bauchspeicheldrüse gebildet. In physiologischer Form ist IAPP löslich und intrinsisch ungeordnet, jedoch hat es eine starke Tendenz zur Aggregation und zur Bildung unlöslicher Fibrillen. Amyloidablagerungen in der Bauchspeicheldrüse, die hauptsächlich aus IAPP bestehen, korrelieren mit Diabetes Mellitus Typ 2 (DM2) und finden sich in 90$\%$ der von DM2 betroffenen Patienten. Humanes IAPP hat eine Disulfidbrücke im N-Terminus und einen amidierten C-Terminus. Das in dieser Studie rekombinant hergestellte Peptid verfügt über die Disulfidbrücke, jedoch über einen freien C-terminus. Es wird somit als IAPP$_{COOH}$ bezeichnet.
Für die Untersuchung von fibrillären Strukturen eignet sich die Festkörper-NMR-Spektroskopie, da diese Methode es ermöglicht, Fibrillen aus Proteinen voller Länge zu untersuchen. Für diese Art von Proben sind sowohl Kristallstrukturanalyse als auch Flüssig-NMR-Spektroskopie nicht geeignet, da die Proben nicht kristallin und zudem nicht löslich sind. Die Untersuchung von Biomolekülen mit NMR-Spektroskopie basiert auf der Detektion der NMR-aktiven Isotope ^{1}H, ^{13}C, und ^{15}N. Informationen zu Sekundär- und Tertiärstruktur des Proteins sind in den chemischen Verschiebungen und in der Stärke von Dipolkopplungen enthalten. Die NMR-Experimente an fibrillärem IAPP haben zu einer vollständigen Zuordnung der Resonanzsignale in den NMR-Spektren geführt. Mit den so erhaltenen chemischen Verschiebungen wurde eine Analyse der Sekundär-

struktur durchgeführt. Für die Hauptkonformation wurden drei β-Stränge gefunden, die auch das amyloidogene Segment ^{22}NFGAILS^{28} enthalten. Der N-Terminus zeigte bei Temperaturen um 0 °C gut aufgelöste und intensive Signale. Diese verbreiterten sich bei Kühlung auf -170 °C stark und waren nicht mehr zu detektieren. Diese Ergebnisse wurden 2016 im Journal PLoS One veröffentlicht.

Darauffolgende Experimente zielten auf das Finden von räumlichen dipolaren Kopplungen, die Informationen über die Tertiärstruktur der Moleküle in der Fibrille enthalten. Dafür wurden zwei neue Proben hergestellt, die auf einer Verdünnung der ^{13}C markierten Kerne in der Probe basieren. Die Verdünnung der markierten Spins ermöglicht die Detektion von schwachen dipolaren Kopplungen, die in einer voll markierten Probe durch den Effekt der *Dipolar Truncation* überschattet werden.

Zusätzlich wurden ^{13}C-^{13}C Korrelationsexperimente mit langer Mischzeit an einer voll markierten und einer verdünnt markierten (1:4) Probe durchgeführt, ebenfalls mit dem Ziel, räumliche Kontakte zu detektieren. Es wurden vier Korrelationen beobachtet, die einen Aufschluss über die räumliche Struktur der IAPP Moleküle in der Fibrille geben können. Diese vier noch uneindeutigen Korrelationen wurden als begrenzende Bedingungen für eine erste Strukturberechnung mit dem Programm Cyana verwendet.
Zudem wurden, basierend auf der zuvor durchgeführten Sekundärstrukturanalayse und aufgrund variierender Intensitätsverteilungen von Cα-Cβ Korrelationen in PDSD Spektren, zwei weitere mögliche Strukturmodelle erstellt.

Abstract

In this thesis, the method of solid-state Nuclear Magnetic Resonance spectroscopy was applied to solve a specific question from the field of protein misfolding diseases. Representatives of protein misfolding diseases are diabetes mellitus type II, Alzheimer´s disease, and Parkinson´s disease. A hallmark of protein misfolding diseases is the extracellular deposition of misfolded proteins, either localized in affected tissue, or systemic throughout the body. The process of protein misfolding leads in many cases to the formation of insoluble amyloid fibrils. Amyloid fibrils formed by a range of different proteins show a highly ordered and repetitive structure, which is rich in β-sheet content. Elucidation of fibril structures on the molecular level is one of the central research topics in the field of protein misfolding diseases.

The topic of this dissertation was the structural characterization of fibrillar human Islet-Amyloid-Polypeptide (IAPP) by solid-state NMR. IAPP is a 37 amino acid residue peptide that is co-secreted with insulin by pancreatic β-cells. IAPP is soluble and intrinsically disordered in its physiological form, however it shows a high propensity to aggregation and fibril formation. Pancreatic amyloid deposits, which consist mainly of IAPP, correlate with type II diabetes mellitus and are found in 90$\%$ of individuals affected by T2DM. Human IAPP has an oxidized disulfide bridge in its N-terminus and an amidated C-terminus. In this thesis, recombinantly expressed IAPP with an intact disulfide bridge, but without an amidated C-terminus, was used. It is denoted as IAPP$_{COOH}$. Solid-state NMR is a versatile tool to study the structure of fibrils built from full length proteins. These samples are not amenable to X-ray crystallography or liquid-state NMR, because they are non-crystalline and insoluble. Solid-state NMR studies on biomolecules are based on the NMR-active isotopes ^{1}H, ^{13}C, and ^{15}N, employing isotope labelling strategies. Information on secondary and tertiary structure is contained in chemical shifts and strengths of dipolar couplings.
A full site-specific resonance assignment was achieved from the ssNMR study on fibrillar IAPP. An analysis of secondary structure was performed based on the chemical shifts. One major conformation was observed, consisting of three β-strands. The amyloidogenic segment ^{22}NFGAILS^{28} was also found to be part of a β-strand. Furthermore, the N-terminus showed well resolved and intense peaks at 0 °C, that broadened below detectability upon freezing to -170 °C. These results have been published in the journal PLoS One in 2016.

Following experiments aimed at the detection of through-space dipolar couplings, which contain information on the tertiary structure of the molecules within the fibril. Two more samples were pre-

pared, applying a labelling approach that yields a diluted distribution of ^{13}C spins in the samples. The dilution of NMR-active spins enables the detection of weak through-space dipolar couplings, which are attenuated in uniformly labelled samples by the effect of dipolar truncation.

Complementary, long mixing time ^{13}C-^{13}C correlation experiments were performed on a diluted (1:4) and an uniformly labelled sample. Four ambiguous long-range cross-peaks were observed in these spectra. They could contain information on the tertiary fold of the molecules within the fibrils. Four ambiguous distance restraints were created from these cross-peaks and used in a first structure calculation with the computer program Cyana.
Moreover, based on the analysis of secondary structure and the varying intensity of Cα-Cβ cross-peaks in short mixing time PDSD spectra, two more structural models were created.

1. Introduction

Protein misfolding, amyloid formation, and the diseases associated with these phenomena have become a topic of high relevance in recent years. Today, around 50 diseases are known to be associated with protein misfolding and amyloid aggregation. Increasing prevalence of affiliated disorders, as type II diabetes mellitus (T2DM), Alzheimer´s disease (AD), or Parkinson´s disease, make it a topic of high relevance in modern societies. The number of individuals suffering from a protein misfolding disorder increases due to ageing society, modern nutritional habits, and missing physical exercise [1].

Each amyloid associated disease is characterized by misfolding and aggregation of a distinct peptide or protein, which is not pathologic in its native, soluble form. The final product of the aggregation process is in many cases a highly organized and repetitive structure, an amyloid fibril. This elongated, unbranched, and rod-like species is found in organ tissue of affected individuals, when the disease is progressed [2]. The name amyloid was given in the late 19th century, when a starch-like composition of the fibrils was assumed. In the beginning of the 20th century, the proteinaceous origin of the amyloid fibril was shown by enhanced staining methods, and later, the highly organized molecular structure, high in β-sheet content, detected by X-ray diffraction analysis [3]. Intriguingly, the underlying repetitive structure appeared to have the same characteristics for amyloid fibrils built from a range of different polypeptide sequences.

An aggregated state represents a state of minimum free energy and is the theoretically most stable state for the majority of proteins or peptides [4]. The aggregated conformation is energetically favorable, due to a minimum of free energy that is reached. However, it is shielded by a high-energy barrier and there are cellular processes, as chaperone molecules or clearance mechanisms, that help to prevent proteins from adopting it. These cellular processes for control of protein homoeostasis are overchallenged in protein misfolding diseases [5]. The aggregated protein can not fulfill its physiological function anymore. Additionally, intermediate and end products of the aggregation process are known to be toxic to cells. Protein misfolding therefore leads to depletion of cellular function, cell death, and reduction of functional tissue volume [6].

Protein misfolding diseases are studied by many research groups and from a range of perspectives. In our group, the structural aspects of fibrillar aggregates are studied by solid-state nuclear magnetic resonance spectroscopy (ssNMR). Characterization of the structure of fibrillar aggregates gained attention, because a strong structural analogy in mature amyloid fibrils has been found, even though there is no analogy in sequence or length along the proteins involved in amyloid diseases [7].

Amyloid fibrils have a highly organized and homogeneous core structure, which is rich in β-sheet

content. Conformationally equal molecules are stacked on top of each other and build an elongated fiber structure. The homogeneity results from the templating property of fibrillar structures. Their conformation is self-propagating, i.e. fibrils act as seeds on soluble monomers and cause soluble monomers to adopt the same pathological conformation as themselves [8]. Templates furthermore act as catalysts on soluble monomers and reduce the activation energy of the misfolding pathway.

There is another intriguing property of fibrils, called polymorphism. One amino acid sequence is able to sample a number of distinct fibrillar conformations. Polymorphism can arise due to structural variation on the molecular level, or on the macromolecular level due to a different packing of monomers or protofibrils into mature fibrils. The fibril itself is made up of homogeneous building-blocks, but a compilation of fibrils shows heterogeneity in the majority of cases [9].

Solid-state NMR is one method of choice to study a full-length peptide or protein in fibrillar form [10]. In recent years, several high-resolution structures of fibrils have been published, based on ssNMR data [11, 12, 13, 14, 15]. Data derived from ssNMR experiments can contain information on secondary, tertiary and quaternary structure of a protein or macromolecule. The secondary structure is examined by analysis of the obtained backbone chemical shifts, the tertiary structure may be revealed by finding through-space long-range contacts in spectra, and the quatnerary structure accordingly by finding long-range contacts in between sub-units or domains. Methodology is improving steadily in solid-state NMR, on the technical side, as well as on the side of sample preparation.

The naturally low abundant NMR-active isotopes ^{13}C and ^{15}N play an important role in biomolecular NMR. They can be introduced into the recombinantly expressed protein sample by growing *E.coli* cells in minimal medium that contains ^{13}C labelled glucose and ^{15}N labelled NH_4Cl as sole carbon and nitrogen sources. In addition to this uniform labelling approach, the ^{13}C spin-labels can be distributed in the sample according to the experimental needs by various labelling strategies. These are mostly used to reduce spectral crowding or to reduce the effect of dipolar truncation, i.e. the attenuation of a weak dipolar coupling in vicinity of a strong dipolar coupling [16]. Furthermore, labelled and unlabelled molecules can be mixed, to obtain a diluted sample. We have recently reviewed strategies for biomolecular solid-state NMR, i.e. labelling strategies, as well as recoupling sequences, in a book chapter in *Modern Methods in Solid-State NMR. A Practitioner's Guide*, that will be published in autumn 2017 [17].

In this thesis, the structure of the 37 amino acid residue peptide Islet Amyloid Polypeptide (IAPP) was characterized in its fibrillar form by solid-state NMR. The aggregation of IAPP is associated with type II diabetes mellitus and amyloid IAPP deposits are found in pancreatic β-cells of more than 90 $\%$ of type II diabetes mellitus (T2DM) patients [18]. The physiologically active form of IAPP in humans has an amidated C-terminus and an intramolecular disulfide bridge in the N-terminus. Here, fibrillar aggregates of recombinant IAPP in its free acid form ($IAPP_{COOH}$) and with an intact disulfide bridge have been studied. A full site-specific resonance assignment was obtained from solid-state NMR experiments, and an analysis of secondary structure was performed. Results

have been published in PLoS One in 2016 [19].
Following the results mentioned above, more experiments were conducted in order to find structurally important long-range contacts in spectra. These are indispensable restraints for a structure calculation based on NMR data. A labelling approach was applied which results in a diluted distribution of ^{13}C labels in the sample. The dilution of spins reduces strong dipolar couplings and enables to observe weak dipolar couplings, which may contain information on through-space contacts. With this labelling approach, two samples were prepared and examined with several long mixing time PDSD spectra.
Additionally, an uniformly and diluted labelled sample were examined further, also with long mixing time (> 500 ms) PDSD experiments. First ambiguous distance constraints were found experimentally, and the restraints were used for an initial structure calculation with the computer program Cyana [20].
Based on the experimental results, three different structural models are proposed. Possible labelling schemes are proposed for future studies, which can be applied to converge to the best fitting model.

1.1 Structural aspects of amyloid fibrils

Structures of fibrils formed from different proteins have been studied intensely in recent years, applying a range of biophysical methods. Among these methods are X-ray fibre diffraction, X-ray crystallography of crystallized fragments, solid-state nuclear magnetic resonance (ssNMR), electron paramagnetic resonance (EPR), atomic force microscopy (AFM), electron-microscopy (EM), and recently also cryo-electron microscopy (cryo-EM) [21, 22, 23, 24, 25, 26, 27].
On the microscopic scale, amyloid fibrils appear as long, rod-like and unbranched species, 5 to 10 nm in width and with a length ranging up to the μm scale [28]. Some fibrils additionally show a regular twist around their long axis. Amyloid fibrils show a cross-β diffraction pattern upon irradiation with X-rays [21]. This pattern arises from β-sheets, which are made up of single β-strands that run perpendicular to the long fibril axis. The β-strands are stacked on top of each other with an inter-strand distance of 4.8 Å. This causes the first reflection in the diffraction pattern. Mostly, two or more β-strands are found per layer of the fibril. The distance in between these strands ranges from 6 Å to 10 Å and causes a second reflection in the diffraction pattern [29, 6]. The stacked β-strands are connected by inter-molecular hydrogen bonds. Side chains face either inside the fibril core and build an interface, also called steric-zipper, or they stick out and are in contact with the surrounding environment [22]. A model showing a parallel in-register arrangement of β-strands within a fibril is shown in Figure 1.1.
Most structural models agree on the in-register, parallel arrangement of β-strands within the β-sheets. Still, there remain big differences in the models presented, regarding lengths of β-strands, packing of side-chains in fibril cores, staggering of β-strands, and the number of symmetric or asymmetric monomers per fibril layer. These differences do not only appear in between struc-

tures formed from different proteins, but also in between structures of fibrils from the same amino acid sequence. Additionally, structures found for fibrils built from segments of aggregation prone sequences do not necessarily resemble the structure of fibrils built from full-length proteins [30]. Polymorphism is observed either on the molecular level, due to a different fold of the molecules, or on the macro-molecular level, due to the parallel or anti-parallel arrangement of β-strands along the fibril axis, the running direction of strands related to each other and facing of the side chains within one layer of the fibril [22].

Hairpin models with two β-strands per molecule have been widely accepted. However, recent publications of molecular fibril structures do not support this generic motif, but a much more complex packing of shorter β-strands [12, 31, 13, 14, 15]. The implementation and validation of efficient biophysical methods to study fibrils of full-length protein on the molecular level is an important aspect on the way to gain a more complete knowledge on the field of protein misfolding diseases. The two most established methods for studying protein structures on the molecular level are liquid-state NMR spectroscopy and X-ray crystallography. Both methods cannot be applied to amyloid fibrils of full-length proteins. Liquid state-NMR is excluded, because amyloid fibrils are insoluble and do not tumble in solution on the time-scales required for liquid-state NMR spectroscopy. X-ray crystallography is not applicable due to the non-crystalline character of fibrils [10]. Short fragments of fibril forming sequences, i.e. up to six amino acid residues in length, were successfully crystallized and studied by X-ray crystallography [22]. These studies have given insights on possible fibrillar core motifs. However, the motifs of crystals do not necessarily resemble the structures of fibrils built from full-length proteins [30]. Therefore, such core motifs have to be validated also on fibrils formed from full-length proteins. Even if polymorphism has shown us, that there is not only one, general fibril structure, it is intriguing to investigate, if common structural motifs are present for fibrils built from different full-length proteins. For this aim, solid-state NMR is a powerful technique to study fibrillar aggregates on the molecular level [10].

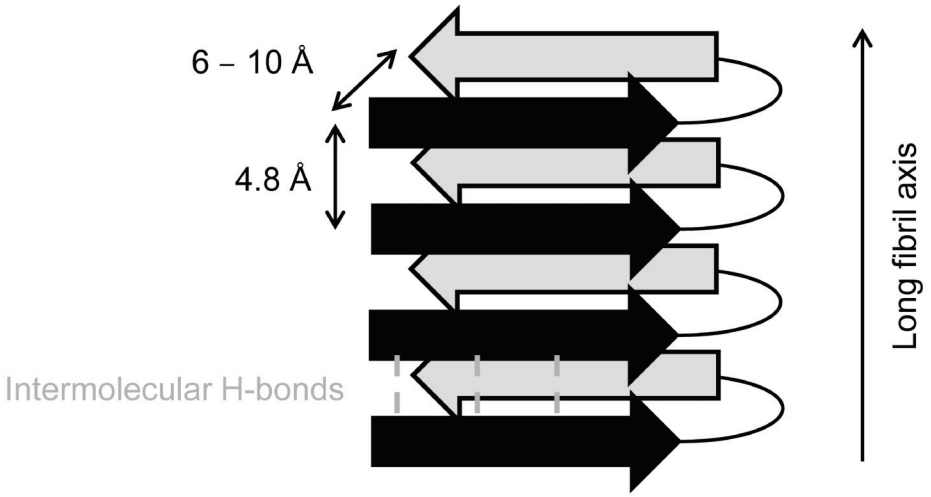

Figure 1.1: *Model of parallel-in-register β-strand arrangement in fibrils*

1.1.1 Fibril formation

Most amyloid fibrils show a repetitive and highly ordered structure. The mechanisms of fibril growth, which have been defined so far, can explain the homogeneous conformation of monomers within one fibril, as well as the occurrence of polymorphism within one sample grown from equal monomers [8]. The mechanisms of fibril growth are shown in Figure 1.2.

Aggregation starts with the formation of condensed particles from soluble molecules. This is the

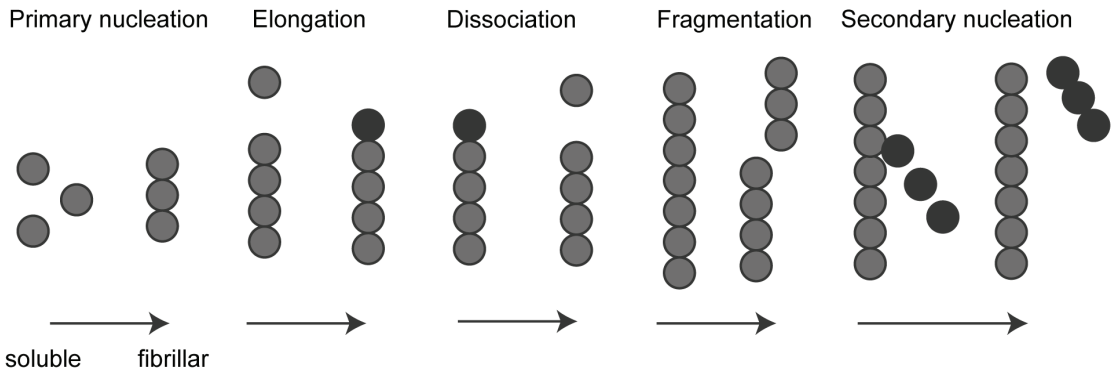

Figure 1.2: *Mechanisms of amyloid formation, as adapted from [32]. The primary processes shown are primary nucleation, fibril growth by attachment of monomeric protein to the end of a fibril, and dissociation of monomers from fibrils. The secondary processes are fibril fragmentation and secondary nucleation.*

moment of nucleation and the processes that lead to nucleation are under investigation. Amplification fibrillar structures includes elongation of fibrils by attachment of monomers to open fibril ends, or secondary nucleation. Elongation by monomer attachment to open fibril ends propagates one equal molecular conformation. Consequently, fragmentation of fibrils propagates one homogeneous fibril structure, because it doubles the amount of open fibril ends that serve as templates. Secondary nucleation does not necessarily propagate the same conformation and it might be a reason for polymorphism. Secondary nucleation is the lateral attachment of a soluble monomer to a fibril surface, which leads to the formation of a new nucleus. The fibril surface is acting as a catalyst for nucleation, but not as a template. The process includes the detachment of the newly formed nucleus or protofibril from the fibril surface [32].

For the production of homogeneous fibril samples *in-vitro*, growth mechanisms that propagate the same molecular conformation are highly desirable. Seeding and sonication are two methods that are widely applied for this aim. Preformed fibrils are added as seeds to soluble monomers in the process called seeding. The monomers are supposed to attach to the fibril ends and take over the same molecular conformation. Sonication of the preformed fibrils promotes fragmentation and produces more fibril ends [33, 34].

1.2 Islet Amyloid Polypeptide

Islet Amyloid Polypeptide (IAPP, Amylin) is a 37 amino acid residue peptide, which is produced by pancreatic β-cells and co-stored with insulin in insulin secretory granules [5]. Upon insulin secretion, co-secretion of IAPP from β-cells occurs [35]. The physiological functions of IAPP described so far are related to glucose and energy homeostasis, control of gastric emptying and satiety, and also modulation of insulin secretion and action [36].
IAPP is derived from a 89 aa residue pre-prohormone that is cleaved to yield the 67-residue pro-IAPP. The mature 37 residue peptide requires further processing and post-translational modifications, i.e. amidation of the C-terminus and formation of an intramolecular disulfide bridge [37]. The N-terminal intra-molecular disulfide bridge spans from residues Cys-2 to Cys-7. At physiological pH, IAPP is slightly positively charged, because of residues Lys-1, Arg-11, and His-18. Despite the charged residues, IAPP is also a partly hydrophobic peptide with 16 residues that carry a hydrophobic side chain. These hydrophobic residues do not cluster in a certain region of the peptide. The sequence of mature human IAPP is shown in Figure 1.3.

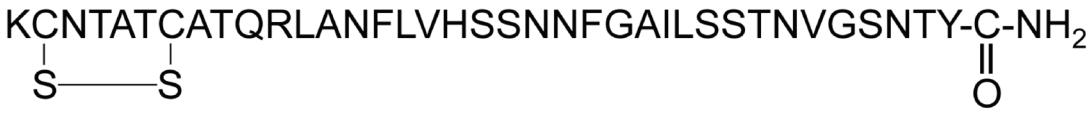

Figure 1.3: *The sequence of mature human IAPP with oxidized intra-molecular disulfide bridge and amidated C-terminus.*

IAPP is highly prone to form cytotoxic aggregates IAPP is an intrinsically disordered peptide, i.e. in its physiological, soluble form it does not adopt a compact globular structure [38]. It is stored in secretory granules at pH 6 [39], an environment that favors the protonated state of His-18 and contributes to stabilization of the soluble monomer, due to electrostatic repulsion [40]. Additionally, co-storing of IAPP and insulin in the granules stabilizes the soluble form of IAPP.
The sequence of human IAPP is highly prone to aggregation and formation of insoluble, cytotoxic amyloid aggregates and fibrils [41]. It is denoted as one of the most amyloidogenic sequences known [42]. The presence of pancreatic islet amyloid deposits is a hallmark of type II diabetes mellitus (T2DM) and correlates with the failure and death of pancreatic β-cells [43]. The mechanisms of cytotoxicity of islet amyloid are under investigation and a range of, possibly concurrent, mechanisms has been found [44]. Disruption of membrane structural integrity by fibrils or their precursors is an important toxic mechanism [45, 46]. Furthermore, many intracellular dysfunctions, as endoplasmatic reticulum stress or hindrance of the autophagy process, are described [37]. As in other amyloid associated diseases, the mature fibril itself is not considered the main toxic species, but rather the highly reactive, transient oligomer species, that forms during the process of aggregation [28].

Rodent IAPP does not form amyloid IAPP has been found in all mammals studied so far and its sequence is strongly conserved [47]. While IAPP of humans, non-human primates and cats forms islet amyloid, it has been found that rodent IAPP does not form islet amyloid. Moreover, rodents do not develop spontaneous T2DM [43]. The IAPP primary structure of three different species is shown in Figure 1.4. Comparing the sequences in Figure 1.4, it becomes obvious that main differences in between amyloidogenic human and non-amyloidogenic rat IAPP manifest in the segment spanning residues (20-29). Here, three proline residues are found in rat IAPP, at positions 25, 28, and 29. Proline imposes a restriction on backbone conformational freedom and is known to be a β-sheet breaker. The aggregation properties of segment (20-29) have attracted attention of researchers, as it was first believed to be the only amyloidogenic segment in the sequence of human IAPP [47]. However, other fibril forming segments of hIAPP were identified. Namely, it was found that also segments (8-20), (30-37), and even the N-terminus (1-8) are able to fibrilize [48, 49, 50].

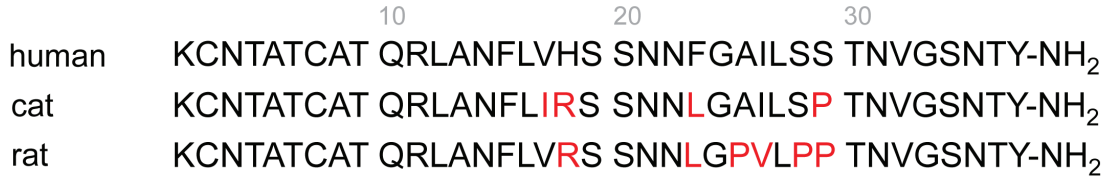

Figure 1.4: *Primary structure of human, cat and rat IAPP. Sequential differences are marked by red residues. Cat IAPP is able to form amyloid, while rat IAPP does not form amyloid.*

1.3 Structural studies on IAPP fibrils

Fibrils formed by IAPP have been studied by different biophysical techniques and insights were combined to build several structural models. In the models described, synthetic IAPP was used and fibrillized. Figure 1.5 shows the β-strand regions as defined in the studies mentioned.

The cross-β diffraction pattern was demonstrated in 2004 by X-ray and electron diffraction studies [51]. In the same year, EPR spectroscopists found evidence for an in-register-parallel arrangement of β-strands in the fibrils [25]. These results and prior insights from electron microscopy [52] were combined in 2005 to a serpentine-model [53]. The authors proposed a β-serpentine fold composed of three β-strands, separated by two turns. Notably, segment (22-27) forms a β-strand in this model.

A highly cited structural model based on a solid-state NMR study was published in 2007 [33]. It confirms the in-register-parallel arrangement by distance constraints gained from dipolar recoupling experiments. In addition, inter-strand side-chain contacts of residues from opposing β-strands were observed. The deduced structural model is made up of two β-strands per monomer. They are located at positions (8-17) and (28-37), and separated by a non-constrained loop. A symmetric dimer model was proposed, with a C_2 symmetry about the long fibril axis. The inner

β-sheets are composed of segments (28-37) and the outer sheets of segments (8-17). The N-terminus is not constrained in this model [33].
Soon after, in 2008, a model based on the crystallized segments ^{21}NNFGAIL^{27} and ^{28}SSTNVG^{33} was proposed. It also contains two β-strands per monomer, located at positions (8-17) and (24-37), and also assumes a symmetric dimer as subunit, with a C_2 symmetry about the long fibril axis. The β-sheets composed of residues (24-37) build the dry steric zipper interface in between two symmetric monomers in one fibril layer [54]. Compared to the ssNMR model, the mating inner sheets comprise 4 additional residues, are located closer to each other, and also the packing of side chains differs.
The fourth model, published in 2012, arose from continuation of the EPR studies from 2004 [25, 55]. This EPR-based model proposes two β-strands at positions (12-19) and (31-36). The prominent aspect of this model is a stagger of the two strands about 3 peptide layers [55]. Such a stagger was not described by the remaining studies.
The last model to mention here is based on an amide ^{1}H solvent protection study [56]. Residues 26-Ile and 27-Leu were found to be protected, i.e. conformationally constrained, by this method. These residues show a higher protection than the loop residues and are therefore assigned to the second β-strand in this model, which is also a β-hairpin model.
There is an overall agreement on the presence of two β-strands per monomer [33, 54, 55, 56], with the serpentine-model being the only exception [53]. The exact length and position of the strands differs in the models described. These differences might be due to polymorphism, caused by different sample preparation methods [9, 57, 6]. As the location of the secondary structure elements differ in between the models, there is most likely a polymorphism on the molecular level present. This shows that different segments of the sequence are able to independently form β-strands. Regarding the controversial amyloidogenic sequence (20-29), it is intriguing, that it is mostly regarded as part of a random coil loop.

IAPP can be stabilized by a binding protein In the group of Dr. Wolfgang Hoyer, the β-binding protein HI18 was designed by phage-display, that binds monomeric, oligomeric, and fibrillar IAPP and inhibits aggregation [58]. Among others, it is used for the efficient recombinant expression of IAPP in *E. coli* cells. It prevents the formation of toxic aggregates during expression and is cleaved-off proteolytically during purification [59]. A solution-state NMR characterization revealed that two HI18 molecules bind one IAPP molecule, and bound IAPP forms a β-hairpin structure, with two β-strands at positions (12-18) and (22-28). In contrast to the fibrillar structure, the stabilizing hydrogen bonds are formed in between the two β-strands of one IAPP molecule. The hydrophobic side-chains of IAPP are sequestered by the β-wrapins. The side-chain interactions with the surrounding HI18 dimer impede interactions in between single IAPP molecules and prevent aggregation. Notably, the amyloidogenic region (22-28) forms a β-strand in this construct.

Figure 1.5: *Location of β-strands in IAPP fibrils as found in different studies. The arrows show the β-strand regions. a) Represents the serpentine model [53], b) the solid-state NMR model [33], c) the model based on crystallized segments [54], d) the EPR model with staggering about 3 fibril layers [55], and e) the model derived from ^{1}H solvent protection [56]. The β-strands indicated in f) belong to a study of IAPP bound to an aggregation inhibitor protein [58].*

1.4 Solid-state NMR spectroscopy of proteins

Nuclear magnetic resonance spectroscopy provides a tool to study the three-dimensional structure of proteins at atomic resolution [60]. Solid-state NMR describes the nuclear magnetic resonance spectroscopy of samples that are insoluble and of high molecular weight and do therefore tumble slowly or not at all in solution. The correlation time of such samples, i.e. the average time for the rotation around one radian, is not on the timescale applicable for liquid-state (solution-state) NMR [61]. As a result of the reduced isotropic tumbling, anisotropic interactions, as chemical shift anisotropy (CSA) and dipolar couplings, are not averaged out as in liquid-state NMR. In first instance, this causes line-broadening and a loss in sensitivity [10]. However, magic-angle spinning (MAS) has been developed to overcome these obstacles.

The anisotropic interactions present in solid-state NMR are chemical shift anisotropy, dipolar couplings, and quadrupolar interactions. The quadrupolar interactions are only present in the case of nuclei with a spin quantum number $I > \frac{1}{2}$ and not further described here.

Chemical shift anisotropy and dipolar couplings are not only averaged out by MAS, but can also be re-introduced by recoupling sequences or matching MAS frequencies, to extract the information contained in these interactions, as distances or orientations. In structural biomolecular NMR, dipolar couplings are qualitatively used for the transfer of magnetization along desired pathways within a spin-network. Quantitatively they can be exploited to gain information on inter-nuclear distances. The size of a dipolar coupling is inversely proportional to the third power of the inter-nuclear distance, i.e. r^{-3}. The magnitude of a dipolar coupling can be quantified and related to a distance information in between the coupled nuclei [17].

Before focusing on the distinct features of solid-state NMR, a short introduction on the principles of NMR is given. This introduction is based on the textbooks by Malcolm H. Levitt [62], James Keeler [63], and John Cavanagh et al. [60].

1.4.1 Principles of NMR

Nuclear spin and Zeeman interaction An intrinsic property of elementary particles as electrons, protons and neutrons is a nuclear spin angular momentum $\vec{I}$. It is described by the nuclear spin quantum number I. The angular momentum is a vector quantity, and its direction may be defined as the spin polarization axis. The nuclear angular momentum can take values defined by $|\vec{I}| = \sqrt{I(I+1)}\hbar$. The z-component of the nuclear spin angular momentum is defined by

$$I_z = \hbar \cdot m \tag{1.1}$$

m is the magnetic quantum number, which takes the values in between -I and +I in steps of one. In a strong external magnetic field $\vec{B_0}$, the spin vector can adopt $(2I+1)$ orientations along the z-axis. These orientations correspond to energy levels, the nuclear Zeeman levels. The energy levels are defined by the following equation

$$E_m = -m\hbar\gamma B_0 \tag{1.2}$$

Spin-$\frac{1}{2}$ nuclei Spins with $I = \frac{1}{2}$ have two Zeeman energy levels in an external magnetic field $\vec{B_0}$. The two energy levels of spin $\frac{1}{2}$ nuclei are denoted as α for $m = +\frac{1}{2}$ and β for $m = -\frac{1}{2}$ states.

$$E_\alpha = -\frac{1}{2}\hbar\gamma B_0 \tag{1.3}$$

and

$$E_\beta = +\frac{1}{2}\hbar\gamma B_0 \tag{1.4}$$

The energy difference ΔE between these two levels is

$$\Delta E = h\gamma\frac{B_0}{2\pi} \tag{1.5}$$

This energy difference can be written in frequency units, when applying the relationship of energy of a photon with its frequency: $E = h \cdot \nu$.

$$\begin{aligned} & h \cdot \nu = \Delta E = h\gamma\frac{B_0}{2\pi} \\ \Leftrightarrow\ & \nu = \gamma\frac{B_0}{2\pi} \qquad |\omega = 2\pi\nu \\ \Leftrightarrow\ & \omega = \gamma B_0 \end{aligned} \tag{1.6}$$

The energy difference of the two Zeeman levels of a spin-half nucleus is proportional to the Larmor frequency of that nucleus. An radio-frequency pulse of this frequency enables to induce transitions in between the energy levels.

Larmor frequency Spin and magnetic properties of the particle are linked to each other. The magnetic moment $\vec{\mu}$ is proportional to the spin angular momentum and the constant of proportionality is the gyromagnetic ratio γ.

$$\vec{\mu} = \gamma\hbar\vec{I} \tag{1.7}$$

γ can take positive and negative values (see Table 1.1). Thus, the magnetic moment $\vec{\mu}$ can point along or in opposite direction of the spin polarization axis. The nuclear magnetic moment $\vec{\mu}$ experiences a torque, when placed into an external magnetic field $\vec{B_0}$. The torque $\vec{M}$ is determined by the following equation.

$$\begin{aligned} \vec{M} &= \vec{\mu} \times \vec{B_0} \\ &= \gamma\hbar\vec{I} \times \vec{B_0} \end{aligned} \tag{1.8}$$

The torque causes the magnetic moment to precess about the magnetic field. The frequency of precession is the Larmor frequency ω_0. It is defined in the following equation.

$$\omega_0 = -\gamma \cdot B_0 \tag{1.9}$$

In Figure 1.6, the two possible orientations of a spin-$\frac{1}{2}$ nucleus in an external field $\vec{B_0}$ are shown, as well as the precession on a cone around the external magnetic field.

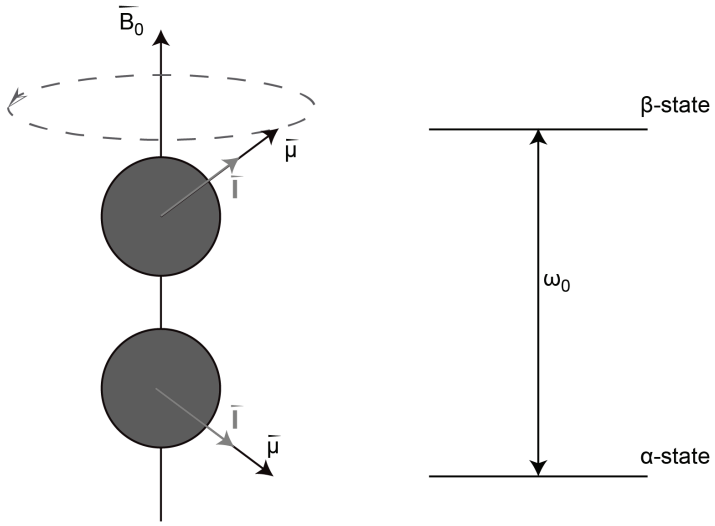

Figure 1.6: *Two orientations of a spin-$\frac{1}{2}$ nucleus in a strong external magnetic field. On the left side, the precession of the spins magnetic moment around the external field on a cone is illustrated. The two possible orientations, spin-up or spin-down are shown. The energy difference between the two states is proportional to the Larmor frequency of the nucleus.*

Isotopes in biomolecular NMR Protein NMR relies mainly on the NMR active nuclei ^{1}H, ^{13}C, and ^{15}N. Specific studies, as studies on membrane interactions, also employ the phosphorous isotope ^{31}P [64]. ^{17}O is the only NMR active oxygen isotope, however its spin $5/2$ makes it more difficult to study, as quadrupolar interactions cause line-broadening. The NMR related properties of the nuclei mentioned are listed in Table 1.1.

The low natural abundance isotopes ^{13}C and ^{15}N are incorporated into the recombinantly expressed protein samples by different labelling techniques. The labelling approaches are based on providing either fully ^{13}C-labelled glucose, or specifically ^{13}C labelled glucose as sole carbon source to the M9 medium. Additionally, specifically labelled or unlabelled amino acids can be added directly to the expression medium. As nitrogen source, mainly ^{15}N labelled $^{15}NH_4Cl$ is used [17].

The highly natural abundant ^{1}H nuclei form a strongly coupled proton network in organic samples. The effect of the strongly dipolar coupled proton spins is described in the following section. One approach to decrease the effect of dipolar coupled protons is the substitution of ^{1}H nuclei by their isotope ^{2}H. In a deuterated sample, the deuterons are not detected, but their diluting effect on the proton network leads to decreased line-broadening [65, 66].

1.4.2 Anisotropic interactions

Due to the reduced or absent isotropic tumbling of proteins or macromolecular complexes in solution, orientation dependent interactions are not averaged out in samples applicable for solid-state NMR. The two anisotropic interactions of spin-$1/2$ nuclei in ssNMR are described below,

Isotope	Spin	Natural abundance	γ in $10^6 rad/(s \cdot T)$	NMR frequency at 14.1 T
^{1}H	$1/2$	99.99 %	267.52	600.34 MHz
^{2}H	1	0.012 %	41.07	92.16 MHz
^{13}C	$1/2$	1.07 %	67.28	150.98 MHz
^{15}N	$1/2$	0.37 %	-27.13	- 60.88 MHz
^{17}O	$5/2$	0.04 %	-36.28	- 81.41 MHz
^{31}P	$1/2$	100 %	108.39	243.23 MHz

Table 1.1: *Properties of relevant NMR active nuclei, adapted from M. Levitt [62]*

based on the publications and textbooks by Henrike Heise [67, 10] and Melinda J. Duer [61].

Chemical shift anisotropy The observed Larmor frequency of a nucleus depends on its local chemical environment. The difference to the theoretically calculated Larmor frequency (Table 1.1) is named the chemical shift δ. The chemical shift arises because every nucleus feels a slightly different magnetic field $\vec{B}_{eff}$ at its site. The resulting field at the site of a nucleus is a superposition of the external field $\vec{B_0}$ and an internal opposing field $\vec{B}_s$, caused by the surrounding electron cloud.

The field $\vec{B}_s$ depends on the chemical environment, but also on the orientation of the molecule in the external field. The chemical shift anisotropy tensor $\hat{\delta}$, a $3x3$ matrix, describes the orientation-dependent shielding.

$$\begin{aligned} \vec{B}_s &= \hat{\delta} \cdot \vec{B}_0 \\ &= \begin{bmatrix} \delta_{xx} & \delta_{xy} & \delta_{xz} \\ \delta_{yx} & \delta_{yy} & \delta_{yz} \\ \delta_{zx} & \delta_{zy} & \delta_{zz} \end{bmatrix} \times \begin{bmatrix} 0 \\ 0 \\ B_0 \end{bmatrix} = \begin{bmatrix} \delta_{xz} \cdot B_0 \\ \delta_{yz} \cdot B_0 \\ \delta_{zz} \cdot B_0 \end{bmatrix} \end{aligned} \tag{1.10}$$

The CSA tensor $\hat{\delta}$ can be visualized as an ellipsoid. The three main axes of the ellipsoid define a coordinate system, the principle axis system (PAS). If the principle axis system is collinear with the laboratory frame (z-axis parallel to $\vec{B}_0$), the CSA tensor is in its diagonal form. If the CSA tensor is in its diagonal form, the shielding field is parallel to the external field $\vec{B}_0$.

In the diagonal form, all elements except of the diagonal elements (main values) equal 0. The main values of $\hat{\delta}$ are denoted δ_{11}, δ_{22}, and δ_{33}. These three main values correspond to the chemical shift, when one of the tensor main axes is aligned parallel to $\vec{B_0}$.

The observed chemical shift in an oriented sample is calculated from the main values as

$$\delta_{obs} = \delta_{iso} + \sum_{k=1}^{3} (3 \cdot cos^2\theta_k - 1) \cdot \delta_{kk} \tag{1.11}$$

θ_k describes the angle between the k^{th} main axis of the tensor and the external magnetic field $\vec{B}_0$.

In a sample consisting of an ensemble of equal molecules with all possible orientations, a broad powder pattern is observed due to the chemical shift anisotropy.

Dipolar coupling The nuclear magnetic moment of each spin causes an additional small magnetic field $\vec{B}_{nuc}$ around the nucleus. Adjacent spins which are not more than 10 Å apart, mutually experience these dipolar fields and are thus dipolarly coupled. Dipolar couplings are either homonuclear (^{1}H-^{1}H, ^{13}C-^{13}C, ^{15}N-^{15}N) or heteronuclear (^{13}C-^{15}N, ^{13}C-^{1}H,^{15}N-^{1}H). The dipolar coupling constant D is defined as

$$D = (\frac{\mu_0}{4\pi})(\frac{\gamma_1\gamma_2}{r^3{}_{1,2}}) \tag{1.12}$$

μ_0 is the magnetic permeability of free space ($4\pi \cdot 10^{-7} V \cdot s/A \cdot m$), $\gamma_{1,2}$ are the gyromagnetic ratios of the nuclei involved and r is the distance between the nuclei. The dipolar coupling of two spins leads to a splitting of the observed peaks.
In the heteronuclear case, the dipolar coupling Hamiltonian is described by

$$\hat{H}_D het = D \cdot \hat{I}_{1z} \cdot \hat{I}_{2z}(3cos^2\theta - 1) \tag{1.13}$$

In the homonuclear case, the dipolar coupling Hamiltonian is described by

$$\hat{H}_D homo = D \cdot (\hat{I}_{1z} \cdot \hat{I}_{2z} - \frac{1}{4}(\hat{I}_{1-}\hat{I}_{2+} + \hat{I}_{1+}\hat{I}_{2-}))(3cos^2\theta - 1) \tag{1.14}$$

In both Hamiltonians, θ describes the angle between the internuclear distance vector $\vec{r}_{1,2}$ and $\vec{B}_0$. Equation 1.14 includes the energy neutral flip-flop term $(\hat{I}_{1-}\hat{I}_{2+} + \hat{I}_{1+}\hat{I}_{2-})$. This term describes the spontaneous exchange of spin angular momentum between two coupled homonuclear spins. This exchange is energy neutral and occurs frequently for the highly abundant ^{1}H nuclei, which build a strongly coupled network in proteins. The flip-flop transition is also exploited for magnetization transfer in between ^{13}C nuclei in the proton-driven spin-diffusion technique and thus very useful for solid-state NMR experiments [68]. On the other hand, the spontaneous exchange of magnetization in between strongly coupled spins causes homogeneous line-broadening, which cannot be refocused. This imposes high requirements on decoupling techniques during acquisition and evolution times.
The homonuclear dipolar coupling constants for low γ nuclei reside in the range below 10 kHz. The heteronuclear coupling to protons is stronger, i.e. around 30 kHz for a directly bonded ^{1}H-^{13}C pair. The strongest couplings appear in between ^{1}H nuclei with strengths up to 100 kHz [69].

1.4.3 Magic Angle Spinning

The anisotropic interactions described contain the angular term $(3 \cdot cos^2\theta - 1)$. If the angle θ, i.e. the angle between $\vec{B}_0$ and the tensor main axis, is set to the magic angle of 54.7°, this term equals 0. This is applied in magic angle spinning by rotating the sample in a stator around an axis that is tilted away from the z-axis ($\vec{B}_0$) by the magic angle.
The net effect of CSA and dipolar coupling experienced by the spins over one rotor period are zero, if a fast enough spinning is applied. In this case, the broad powder pattern caused by CSA is reduced to a line at the isotropic chemical shift δ_{iso} and the dipolar splitting and dephasing do not occur. However, if the frequency of rotation does not exceed the line-width caused by CSA,

spinning sidebands are observed. These sideband signals appear at a distance ν_{rot} from the main signal in spectra. MAS is applied in our spectrometers at frequencies between 11 kHz and 35 kHz. The spinning frequency can be increased, when the rotor diameter is decreased. For example, a rotor with an outer diameter of 3.2 mm can be rotated up to 22 kHz and a rotor with 1.6 mm diameter up to 40 kHz. New developments report spinning speeds up 100 kHz for protein samples [70]. As even this frequency is not yet enough to completely decouple the strong proton network, additionally the method of deuteration and partial back-exchange is developed in order to become able to detect the proton dimension directly [65, 71].
As mentioned above, the strong homonuclear proton-proton dipolar couplings can reach up to 100 kHz. Therefore, proton couplings are not completely averaged out by moderate spinning frequencies below 20 kHz. Additional proton decoupling has to be provided by radio-frequency pulse sequences. The most frequently applied decoupling sequence in our group is SPINAL-64 [72].

1.4.4 Structural studies by NMR

In an NMR study on protein structure, a site-specific resonance assignment is the first step toward structural characterization. Site-specific resonance assignment means that every nucleus in the system under investigation is assigned to its corresponding chemical shift. In the case of ssNMR, the ^{1}H chemical shifts are not detected and therefore not assigned. In the course of assignment, firstly the spin systems of all amino acids are determined by ^{13}C-^{13}C correlation spectra and ^{15}N-^{13}Cα^{13}CX correlation spectra. In the following step, site-specific information is extracted. This is done either by ^{13}C-^{13}C correlation experiments with mixing times around 200 ms, in which the magnetization diffuses in between neighbouring spin systems, or by ^{15}N-^{13}CO experiments, which link the carbonyl ^{13}C of a spin system to the nitrogen chemical shift of the subsequent residue [73].
The homogeneity of the sample, i.e. the homogeneous morphology of the fibrils, has a strong influence on the resolution of the peaks. A more homogeneous sample yields better defined peaks than a less homogeneous sample and therefore probably less spectral overlap. The homogeneity of a sample is related to the dispersion of the backbone ^{15}N chemical shifts [15].
For small proteins as IAPP or Aβ, the resonance assignment can be achieved on uniformly ^{13}C, ^{15}N labelled samples. For proteins with a higher number of amino acid residues, specific labelling may reduce spectral overlap.

Secondary structure correlates with chemical shifts Once a site-specific resonance assignment is achieved, conclusions on secondary structure can be drawn from the chemical shifts of the backbone nuclei Cα and Cβ [74]. In secondary structure elements as α-helix or β-sheet, their chemical shifts deviate systematically from random-coil values.
The deviation from random-coil chemical shifts is analyzed by calculation of secondary chemical shifts. The secondary chemical shift is defined as $\delta_{sec} = \delta_{exp} - \delta_{rc}$. It is calculated sepa-

rately for Cα and Cβ values. The difference of the secondary chemical shifts is calculated as $\Delta\delta = \delta_{sec}\alpha - \delta_{sec}\beta$. In α-helices, the Cα chemical shifts are shifted to higher frequencies and Cβ chemical shifts are shifted to lower frequencies; in β-strands it is vice versa [74]. Therefore, α-helices are indicated by positive difference of Cα and Cβ secondary chemical shifts, and β-strands by negative difference of secondary chemical shifts.

There are three possible sources of random-coil chemical shifts. Firstly, random-coil values have been determined experimentally in 1995 by Wishart et al. in model peptides [75]. Secondly, chemical shifts of NMR studies are deposited in the BMRB database [76]. The average values of the deposited chemical shifts can be used as random-coil values. Thirdly, the group of Wishart has generated a revised chemical shifts databank, based on BMRB entries. This databank, RefDB, currently comprises 2162 re-referenced protein chemical shifts [77].

A computer program for the analysis of secondary structure based on secondary chemical shifts and primary structure is TALOS-N [78, 79]. It compares the sequence and the experimentally derived secondary chemical shifts with a structure database, searches for homologies of both input parameters, and predicts the dihedral angles ϕ and ψ for the segment under investigation. The dihedral angles subsequently serve as constraints for structure calculations.

In addition to the chemical shift based analysis of secondary structure, the peak intensities in cross-polarization based solid-state NMR spectra contain information on the rigidity of a segment [80, 81]. If the peaks are rather weak and broad, and even a scattering occurs, a less constrained region is assumed. Well defined and intense peaks represent a structurally more constrained region. A J-coupling based experiment, INEPT, is used to initially observe, if any mobile residues are found in the sample [82]. Signals observed in this experiment belong to mobile regions.

Through-space contacts The knowledge of the location of secondary structure elements is one important step toward structure elucidation. The next step is the detection of structure-relevant through-space contacts, i.e. dipolar couplings of spins that are close in space due to the fold of the protein. These appear as cross-peaks between nuclei which are more than two amino acid residues apart in the sequence, when long-mixing time experiments are applied. Alternatively, the distance in between specifically labelled nuclei can be detected using dipolar recoupling pulse sequences as REDOR or RFDR [83].

Long-distance dipolar couplings are weaker than couplings of neighboring spins and harder to detect. The effect of dipolar truncation describes the attenuation of weak dipolar couplings in the vicinity of strong dipolar couplings [16]. However, recent publications have reported the extraction of through-space contacts also from experiments on uniformly labelled systems [15, 14]. The experiments that are applied for the extraction of through-space contacts on fully labelled samples are mainly ^{13}C-^{13}C correlation experiments, as PDSD, DARR, and PAR [68, 84, 85]. Magnetization can be transferred over distances up to 9 or 10 Å, depending on the mixing time [11].

If the dipolar truncation impedes the detection of long-range contacts, the attenuation can be overcome by diluting the spins in the sample by sparse labelling approaches [17].

1.5 Objective

Protein misfolding diseases are devastating diseases and place a high burden on our modern society. One of the highly investigated topics related to protein misfolding diseases is the elucidation of the structure of amyloid fibrils on the molecular level.
Fibrillar aggregates have the ability to transform soluble molecules by propagating their pathogenic conformation and the infectivity appears to be contained in the fibrillar structure itself. On the way to a thorough comprehension of misfolding diseases, the knowledge of fibrillar structures is an important step.
Structural models are proposed from time to time by reputable scientists, but a real connecting link in between the different models is still missing. It is intriguing to find out, if fibrils are closely related on the level of molecular conformation, for example by characteristic side-chain contacts. If there is a structural relationship in between all fibril cores, the knowledge gained on one system could be transferred to the whole range of related diseases.
The efficient implementation of biophysical techniques for structure elucidation is essential for this research field.

The aim of this dissertation was to gain insights into the structural characteristics of fibrillar IAPP. The method which was applied for this aim was solid-state nuclear magnetic resonance spectroscopy. In order to efficiently characterize fibrillar IAPP, different labelling strategies and pulse-sequences were applied.
Fibrils formed from IAPP are a versatile model system for structural studies of fibrils. Fibrillar samples impose common requirements, both on sample conditions, as well as on NMR experimental conditions and assignment strategies. Insights from studies on fibrillar IAPP are therefore transferable to other systems, as for example fibrillar Aβ.

2. Material and Methods

Pages 23 to 26 are taken from *Weirich et al., PLoS ONE 11(9): e0161243*.

2.1 Recombinant expression and fibrillation

Human IAPP was expressed recombinantly in *E.coli* cells. It was expressed fused to an engineered protein tag to prevent aggregation as described in detail by Mirecka et al. [59]. The β-wrapin was cleaved off by Protease Factor Xa digestion after expression. With this expression protocol, the free acid form of IAPP, IAPP$_{COOH}$ was obtained without any additional aa residues. Uniformly ^{13}C, ^{15}N-labelled IAPP$_{COOH}$ was expressed and purified with a yield of about 3mg pure peptide per liter of culture. It had an intact disulfide bridge between cysteine residues at positions C2 and C7. The oxidation state was proven by reversed-phase high-performance liquid chromatography (RP-HPLC) with different retention times for oxidized and reduced peptide forms [59]. The corresponding RP-HPLC chromatograms are shown in Figure 2.1. Purified IAPP was lyophilized and stored at -80℃ in glass tubes. Prior to fibrillation, IAPP$_{COOH}$ was monomerized by dissolution in hexafluoroisopropanol (HFIP) to a concentration of 0.3 mM for 48 hours, lyophilized and stored at -80℃. Fibrillation was achieved in a stepwise procedure during seven consecutive days. At day one, a fraction of IAPP$_{COOH}$ was dissolved to a concentration of 110 μM in fibrillation buffer at pH 7.4. The solution was exposed to intermittent sonication without shaking at room temperature overnight, as described previously in the literature [33]. The following six fractions were dissolved accordingly and added to the existing fibrillation solution in the sonication bath on a daily base. Turbidity of the solution was detected by unaided eye after few minutes. After fibrillation, the solution was centrifuged at 16,100 g and 4℃ for 1 hour, followed by centrifugation at 100,000 g and at 4℃ for 90 minutes. RP-HPLC analysis of the supernatant after fibrillation and pelletization revealed that monomeric IAPP$_{COOH}$ was completely absent, i.e. the sample was completely fibrillated. After discarding the supernatant, the highly viscous sample was filled into a rotor from Agilent Technologies, with 3.2 mm diameter and 22 μl sample volume. A second fibril sample was prepared accordingly by co-fibrillating ^{13}C, ^{15}N-labelled IAPP$_{COOH}$ with unlabelled IAPP$_{COOH}$ in the ratio 1:4.

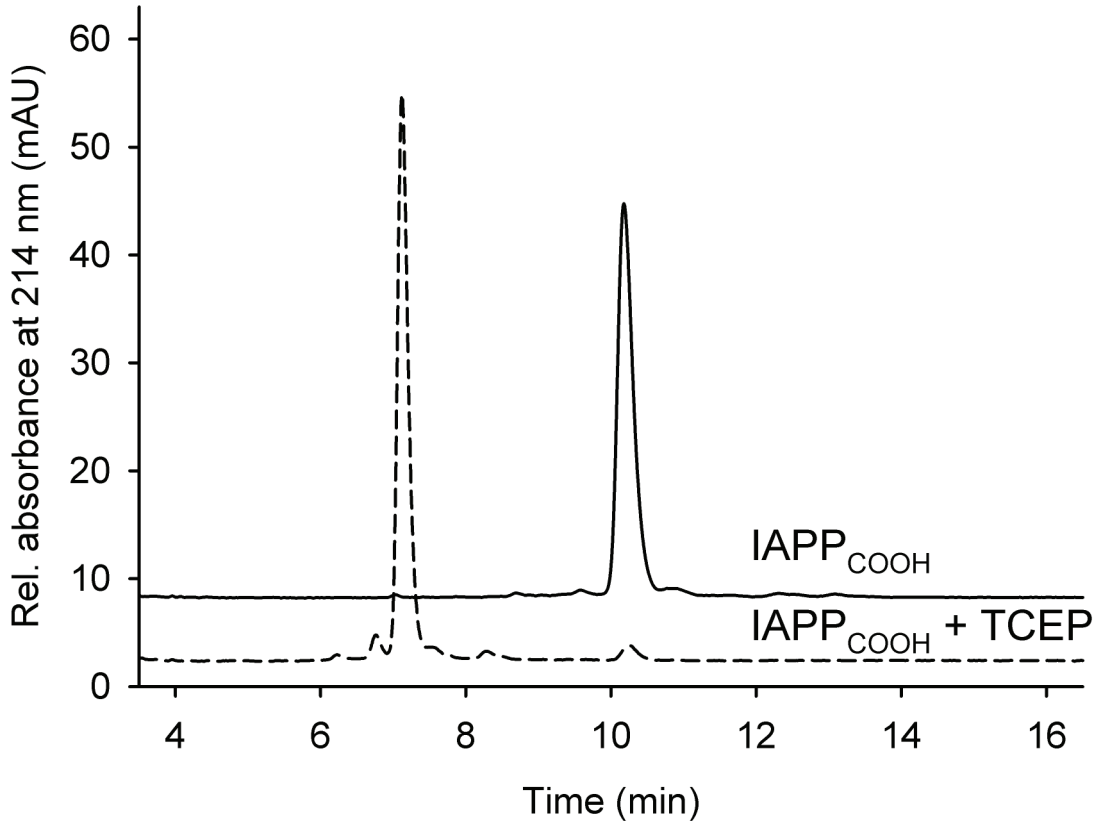

Figure 2.1: *Analytical RP-HPLC before fibrillation. Performed under reducing (dashed line) and oxidizing (solid line) conditions to verify the presence of the disulfide bridge between residues C2 and C7. (PLoS ONE 11(9): e0161243)*

2.2 Solid-state NMR experiments and processing of spectra

MAS-NMR experiments were performed at Varian spectrometers at fields of 14.1 T and 18.8 T (Experimental details in Table 6.1 on page 93). All but one pulse sequences used started with a ^{1}H to ^{13}C cross-polarization step [80]. Exception was the J-coupling based INEPT (Insensitive nuclei enhanced by polarization transfer) experiment [82]. External calibration of the sample temperature, using the ^{1}H chemical shift of nickelocene as temperature standard [35], showed that at a spinning frequency of 11 kHz the actual sample temperature was 10 °C $\pm$ 3 °C above the temperature of the variable temperature (VT) gas which in the following is given as the nominal sample temperature. Proton-driven spin-diffusion (PDSD) experiments were conducted with longitudinal mixing times ranging from 20 ms to 200 ms [36]. Mixing times of up to 50 ms mainly led to intra-residual cross-peaks in spectra, while inter-residual peaks showed up with longer mixing times. A 200 ms mixing time PDSD was performed with MAS spinning of 12500 Hz at an 800 MHz proton frequency spectrometer. This spinning frequency was close to a Cα-CO rotational resonance condition and enabled detection of weak inter-residue couplings CO(i-1)-Cα(i) in vicinity of strong intra-residue couplings [82]. The observed inter-residual cross-peaks were strong indicators for sequential linking of residues and used for sequential resonance assignment. For discrimination of one-bond correlations from relayed and sequential ones, SPC5$_3$, a double quantum coherence sequence, was used at an MAS spinning frequency of 11 kHz [86]. A further ^{13}C, ^{13}C correlation experiment was based on a homonuclear double-quantum transfer step called DREAM (Dipolar recoupling enhanced by amplitude modulation) [87]. DREAM mixing was done with a tangentially shaped soft pulse during 1500 μs, followed by a 90° pulse on ^{13}C nuclei. In the 2D and 3D ^{15}N, ^{13}C correlation experiments, the second transfer relied on spectrally induced filtering in combination with CP (SPECIFIC-CP) and enabled a frequency selective polarization transfer from amide to Cα or CO nuclei [88]. NCACX/NCACB spectra served the assignment of ^{15}N backbone shifts and NCOCX the linking of residues, as magnetization was transferred from N(i) to CO(i-1) and further to CX(i-1) nuclei by spin diffusion. The NHHC experiment [89] was recorded at a spinning rate of 11 kHz, with CP contact times of 200 μs, 200 μs and 70 μs for HN, NH and HC transfers respectively, and a longitudinal proton mixing time of 50 μs. High-power broadband decoupling on protons with SPINAL phase modulation [72] was applied for all spectra during acquisition and t1, t2 evolution times. All processing of raw data was done with NMRPipe [90]. Spectra were multiplied with sine-bell window functions shifted from 0.25 π in ^{13}C to 0.4 π in ^{15}N dimensions and analyzed using CcpNmr Analysis [91]. The low temperature spectrum of fibrillated IAPP$_{COOH}$ was acquired with dynamic nuclear polarization (DNP) enhancement [92] on a 600 MHz Bruker Avance III HD spectrometer at a sample temperature of circa 100 Kelvin. The gyrotron provides microwaves at 395 GHz frequency. For better freezing properties and optimization of the DNP enhancement, the final sample contained 10% H20, 30% D2O and 60% d8-Glycerol. The biradical added to the sample was AMUPOL [93] to a final concentration of 20 mM. The double-quantum DNP spectrum was recorded at 8 kHz MAS with SPC5$_2$ recoupling [94].

2.3 Thioflavin-T fluorescence

The time course of fibrillation of IAPP was studied in different buffers and with different concentrations of the β-wrapin HI18 by detection of Thioflavin-T fluorescence.
IAPP was dissolved in buffer to a final concentration of 10 μM and ThT was added to a final concentration of 40 μM. The total sample volume per well was 150 μl. The samples were pipetted into a 96-well plate (Greiner flat-bottom) and a protective foil was set on top. The temperature of the plate reader (FLUOstar OPTIMA, BMG Labtech) was set to 33°C. 250 cycles of 4 min duration each were applied. In the first run (A), 30 seconds shaking were applied before each scan, while in the second run (B), no shaking was applied. At the end of each cycle, one scan was done.
Every condition was measured once and each sample was prepared with and without addition of ThT (white vs. grey boxes). The samples without addition of ThT did not show fluorescence, but were used for AFM measurements later on. The set-up of the assay with buffer conditions and HI18 concentrations is shown in Figure 2.2.

A)
96 Well Greiner Flat Bottom
Temperature 33 °C
with shaking

	$C_{initial}$	V per well	C_{final}
IAPP	150 uM	10 ul	10 uM
HI18	150 uM	0-20 ul	0-20 uM
ThT	1,47 mM	4,1 ul	40 uM
total		150 ul	

		NaPi, pH 6, 50 mM		MES , pH 6, 50 mM		NaPi, pH 7.4, 50 mM		Tris, pH 7.4, 50 mM		HEPES, pH 7.4, 50 mM	
		rIAPP		rIAPP		rIAPP		rIAPP		rIAPP	
		1	2	3	4	5	6	7	8	9	10
IAPP, 0 uM HI18	A										
IAPP, 2 uM HI18	B										
IAPP, 5 uM HI18	C										
IAPP, 10 uM HI18	D										
IAPP, 20 uM HI18	E										
		- ThT	+ ThT		+ ThT		+ ThT		+ ThT		+ ThT

B)
96 Well Greiner Flat Bottom
Temperature 33 °C
without shaking

		NaPi, pH 6, 10 mM		NaPi, pH 6, 10 mM		Napi, pH 6, 10 mM		Napi, pH 6, 10 mM	
		sIAPP		rIAPP		rIAPP		sIAPP	
		5	6	7	8	9	10	11	12
IAPP, 0 uM HI18	A								
IAPP, 2 uM HI18	B								
IAPP, 5 uM HI18	C								
IAPP, 10 uM HI18	D								
IAPP, 20 uM HI18	E								
			+ ThT		+ ThT		+ ThT		+ ThT

Figure 2.2: *Assay to study IAPP fibrillation by the fluorescence dye Thioflavin-T. ThT fluorescence studies on IAPP were conducted with different buffers and with different concentrations of the β-wrapin HI18. In A), shaking of the plate was applied before each scan, and in B), no shaking was applied. Recombinant or synthetic IAPP were used, as denoted below each buffer.*

2.4 Microscopic studies

2.4.1 Atomic force microscopy

The samples of the above mentioned fluorescence study were also studied by atomic force microscopy (AFM). If not indicated otherwise, the samples without addition of ThT were studied by AFM.

Sample holders were prepared by first washing a microscope slide with ethanol, drying it, and fixing the mica with glue on top. The upper slices of the mica surface were removed with adhesive film to get a smooth surface.

Best results were yielded, when 10 μl of fibril pellet were washed 3 times with 50 μl MilliQ by centrifugation. After washing, the pellet was again resuspended in 50 μl MilliQ, and 25 μl of the suspension were put on the Mica surface. It was incubated for 20 minutes and washed 3 times with 100 μl MilliQ. Then it was dried in an N_2 gas stream. The cantilever used was OMCL-AC160TS in intermittent contact mode (AC mode) on a JPK NanoWizard II. First, image areas of (50 μm)^2 were scanned with 256x256 pixels. Closer scans were performed with image areas of (5 μm)^2 and (1 μm)^2 with up to 1024x1024 pixels.

2.4.2 Electron microscopy

The sample preparation for electron-microscopy on uranylacetate-stained IAPP fibrils was done with 20μl of fibril pellet. It was washed once with 50 μl of fibrillation buffer and twice with 50 μl MilliQ. After washing, the pellet was dissolved in 50 μl MilliQ.

The staining was prepared by first centrifuging the uranylacetate at 18 000 g for 10 minutes. Only the supernatant was used. Grids were cleaned in a plasma chamber and afterward 10 μl of sample placed on the grid. It was incubated for 2 minutes and the liquid removed from the grid using filter paper. It was washed with 20 μl MilliQ for 3 times. Then it was washed with 5 μl uranylacetate, and the uranylacetate was removed immediately with filter paper. The last step was to incubate with 5 μl uranylacetate for 1 minute and remove it by filter paper. The EM study was done by Prof. Dr. Gunnar Schröder.

2.5 Selectively and extensively labelled IAPP$_{COOH}$

Two selectively and extensively labelled samples were prepared applying the *Ten amino acid selective and extensive* labelling scheme (TEASE) [95]. In this approach, 1-^{13}C glucose or 2-^{13}C glucose (Figure 2.3) were used as sole carbon sources in the M9 medium. Furthermore, ten amino acids were added in a concentration of 150 μg per ml in natural abundance form to the medium. Those are Asn, Asp, Arg, Gln, Glu, Ile, Lys, Met, Pro, and Thr. As a result, these spin-systems are unlabelled and the others are sparsely labelled at distinct positions as seen in Figure 2.4 [96].

In the two IAPP samples prepared with this technique, the six amino acids Asn, Thr, Lys, Ile, Gln, and Arg were added in natural abundance to the growth medium and $^{15}NH_4Cl$ was used as sole nitrogen source. As the four amino acids Asp, Glu, Met, and Pro do not occur in the sequence of IAPP, they were not added in natural abundance.

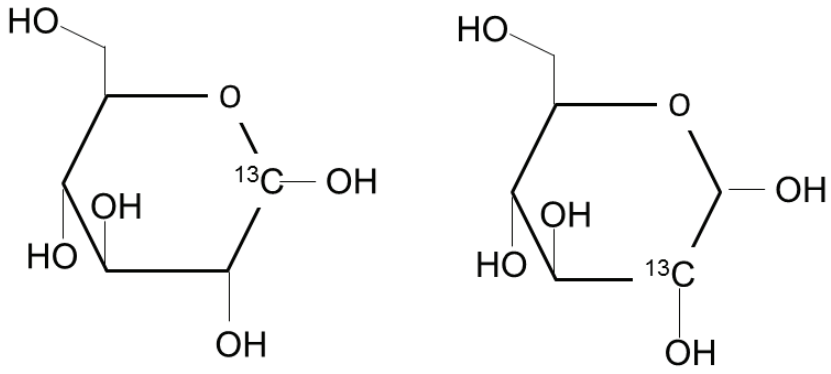

Figure 2.3: *1-^{13}C glucose and 2-^{13}C glucose.*

2.5.1 Recombinant expression and purification

Expression and purification of recombinant IAPP fused to the β-wrapin HI18 were done following the methods described before [59]. Some adaptions were made regarding buffer recipes and workflow of purification. All buffer recipes are found in section 2.8 on page 37.

Recombinant expression One preculture was grown overnight in unlabelled M9 medium (3 g/l glucose, 2 g/l NH_4Cl, unlabelled amino acid mix) at 37°C, 160 rpm. Cells were pelleted and, for each of the two main cultures, resuspended in 800 ml labelled M9 medium (Table 2.1). The two main cultures were incubated at 37°C and 180 rpm. Expression was induced at an OD of 0.6-0.8 with a final concentration of 1 mM IPTG, and cells were incubated in a shaker cooled to 27°C at 180 rpm overnight. Cells were harvested, resuspended in lysis buffer and centrifuged at 4000 g for 20 minutes. The 1-^{13}C labelled sample yielded 4.8 g cell pellet and the 2-^{13}C labelled sample 5.1 g. Each cell pellet was resuspended in 50 ml lysis buffer and frozen at -20°C. The recipe for the lysis buffer is found in table 2.3.

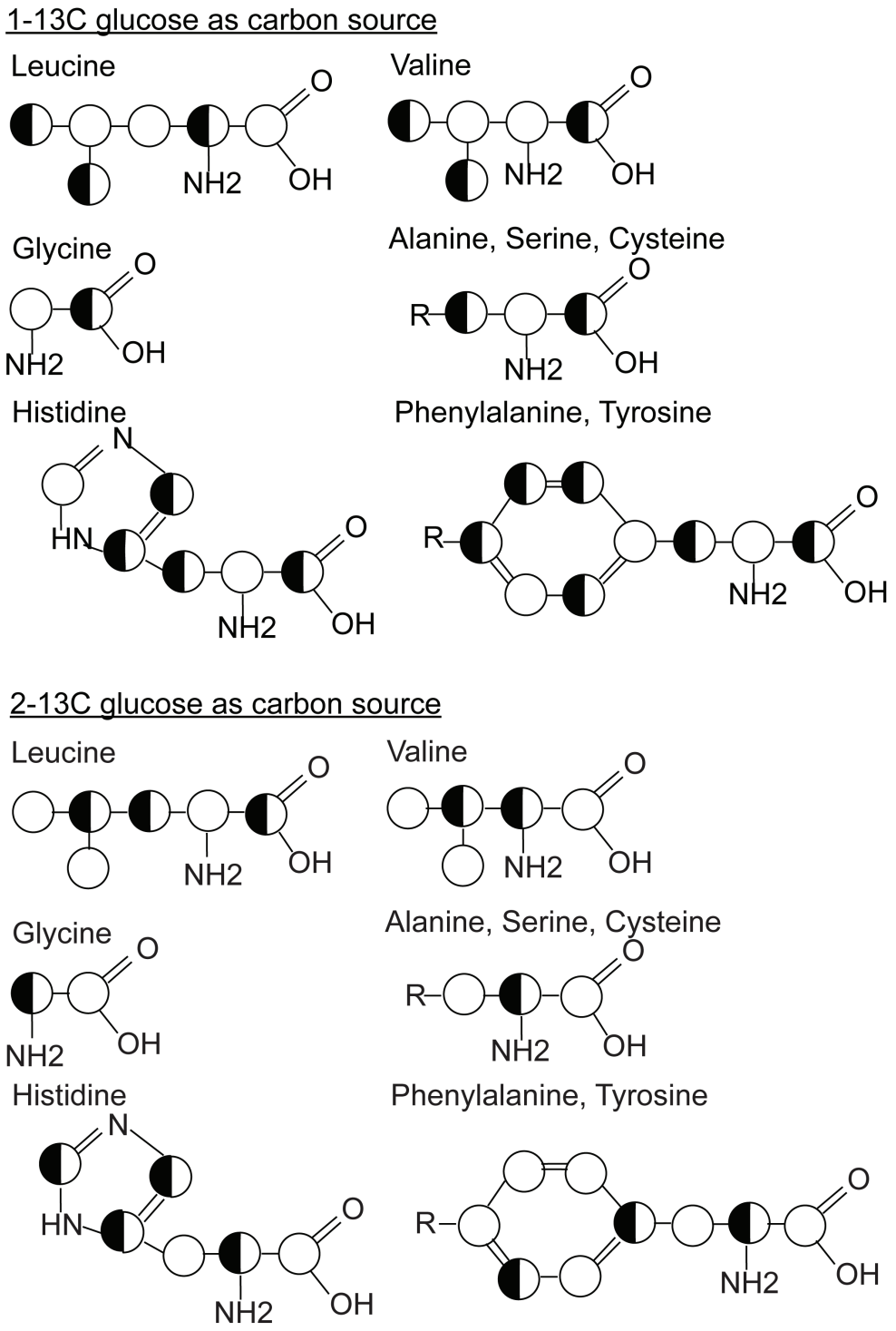

Figure 2.4: *Distribution of spin labels expected from the TEASE labelling approach. Amino acids from the citric acid cycle are added in unlabelled form to the expression medium and do not appear. Black spheres show the labelled position when 1-^{13}C glucose is used as carbon source (A) and when 2-^{13}C glucose is used (B). Due to the glycolytic pathway, positions are labelled with a probability of 50 %.*

Purification and proteolytic cleavage Cells were thawed, and 50 ml Tris buffer were added to each suspension. Cell lysis was done with ultrasonication. During sonication (probe VS70T) at 70% amplitude, the beaker containing the cells was was placed in an ice container to avoid sample heating. 20 cycles were applied with one cycle comprising 10 on-off cycles (1 sec: 3 sec). The lysed cells were centrifuged at 2000 g for 10 minutes, and the supernatant was centrifuged in an ultracentrifuge at 40 000 rpm for 1 hour at 4° C. The supernatant was used for purification.
In the publication of 2014 [59], immobilized metal affinity chromatography (IMAC), followed by size exclusion tomography (SEC) were applied. These two steps were reduced to only the IMAC step on a nickel column in the current protocol. Two columns (Protino Ni-NTA Columns, 5 ml, Macherey-Nagel) were connected in series in an ÄKTA chromatography system. Nickel columns were equilibrated in 10 mM Imidazole buffer. The supernatant was loaded with a flow rate of 1.5 ml/min. After loading, columns were washed with 10 mM Imidazole buffer, until the baseline was reached (3 ml/min). Elution was done with 12 column volumes (i.e. 120 ml) at a flow rate of 2 ml/min on a gradient to 100 % of 500 mM Imidazole buffer. Absorption at 280 nm was monitored, and 5 ml per fraction were collected. Fractions were stored at 4℃ until further processing. The buffer recipes for IMAC are found in Table 2.4 and 2.5.
Subsequent proteolytic cleavage of IAPP from the binding protein HI18 was done by Protease Factor Xa digestion (Merck Millipore). For the digestion of 5 mg fusion protein, 100 μl Factor Xa and 20 μl $CaCl_2$ (0.5 M stock) were added and incubated at 4℃ for 12 to 16 hours. The suspension can be stored even longer at 4℃. Before RP-HPLC, the suspension was centrifuged in 15 ml falcon tubes at 2000 g for 10 minutes at 4℃. The supernatant was loaded on a preparative Zorbax C8 column, 9.4 mm x 250 mm, equilibrated in 27 % Acetonitrile (ACN), 0.1 % Triflouroacetic acid (TFA). A 1000 μl sample loop was used and maximum 600 μl sample per run. The flow rate was set to 4 ml/min. The RP-HPLC purification protocol was: Isocratic elution at 28.5 % ACN, 0.1 % TFA for 20 min (95% D), a 3 min gradient to 80 % ACN, stay at 80 % for 5 minutes. Reequilibrate for 7 min to 28.5 % ACN, 0.1 % TFA. A chromatogram of a preparative run is shown in Figure 2.5 A). The buffer recipes for HPLC are found in tables 2.6, 2.7, and 2.8.
The eluted volumes were 377 ml for the 1st and 268 ml for the 2nd sample. Of each eluate 20 μl were put aside for an analytical HPLC run.
Eluates were filled in 1 liter flasks and frozen in liquid N_2. The frozen samples were lyophilized. Lyophilized IAPP samples were dissolved in 10 ml HFIP each and aliquots of 2 ml were frozen at -80℃. For liquid state NMR, 300 μl of each aliquot were put aside.

Calibration of RP-HPLC chromatogram To determine the concentration of an IAPP sample by RP-HPLC, one run with a defined sample concentration was performed, as shown in section B) in Figure 2.5. For this aim, 45 μg of synthetic IAPP (Bachem) was dissolved in 150 μl of fibrillation buffer (300 μg/ml) and 20 μl of sample were injected for the analytical run on an analytical C8 column. The peak area detected was 3763.24 mAU·s.

$$3763.24mAU \cdot s \equiv 300\mu g/ml \Leftrightarrow 12.54mAU \cdot s \equiv 1\mu g/ml \tag{2.1}$$

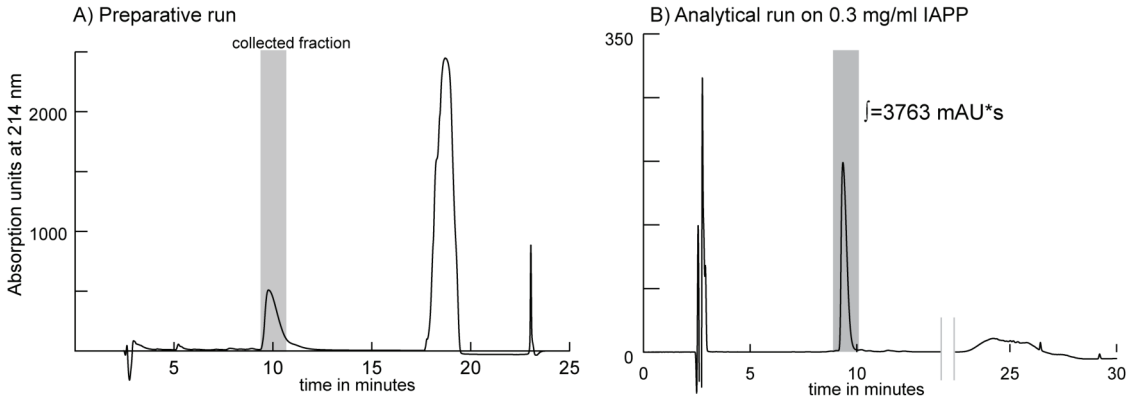

Figure 2.5: *A) Chromatogram of preparative RP-HPLC on IAPP and indication of the collected fraction. B) Analytical run with a defined sample concentration of 0.3 mg/ml IAPP. The peak area is determined and used as calibration point.*

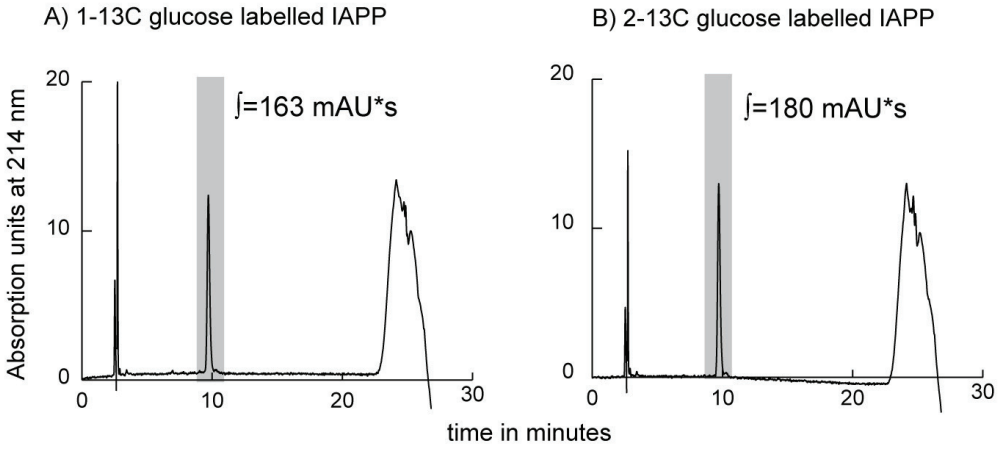

Figure 2.6: *Determination of the concentration of the TEASE labelled samples via analytical RP-HPLC.*

The peak area of 12.5 AU·s in the chromatogram equals an IAPP concentration of 1 $\frac{\mu g}{ml}$. Concentrations of further IAPP samples can therefore be calculated from the peak areas of equally performed HPLC runs.

Concentration of selectively and extensively labelled samples After purification, 20 μl of each sample were used for an analytical RP-HPLC run. The chromatograms are shown in Figure 2.6. With the calibration point determined before, the concentrations were calculated as 120 μM and 95 μM for the first and the second sample, respectively.

Fibrillation for ssNMR samples The aliquots of IAPP in HFIP were thawed, distributed into 4 glass tubes and lyophilized. Fibrillation was done in a stepwise procedure. On the first day, the first aliquot was dissolved in 2.5 ml fibrillation buffer (Table 2.9). It was put into a sonication bath for 30 seconds. Every hour, 30 seconds of sonication were applied. After 24 hours, the next

aliquot was dissolved in fibrillation buffer, sonicated for 30 seconds, and added to the first aliquot. Intermittent sonication was applied during all four days of seeded fibrillation. After fibrillation, the solution was transferred into a 15 ml falcon tube and centrifuged in a swing-out rotor for 1 hour at circa 2000 g (3700 rpm max.). The fibril pellet was stored at 4°C.

2.6 NMR studies on selectively and extensively labelled IAPP

2.6.1 Liquid-state NMR

IAPP dissolved in HFIP was lyophilized and dissolved in 50 mM MES buffer at pH 6 (Table 2.10). Under these buffer conditions, IAPP stays soluble for several hours, allowing to perform a set of liquid-state NMR experiments. Solution-state NMR experiments were conducted to compare the ^{15}N-HSQC fingerprint with existing literature and prove the labelling scheme of the TEASE labelled samples [97, 59, 98].
All experiments were done on a 600 MHz Bruker spectrometer with the help of Dr. Rudolf Hartmann.

Uniformly labelled IAPP 150 μg IAPP were dissolved in 300 μl MES buffer (50 mM, pH=6). 15 μl D_2O were added. Experiments were conducted at 5°C. A ^{15}N-HSQC was acquired with 8x128 scans in 20 minutes and a ^{13}C-HSQC was acquired with 16x256 scans in 1.5 hours. The HNCaCB 3D experiment and the HNCoCaCb 3D experiment were both acquired with 32x40x64 scans in 24 hours.

Selectively and extensively labelled IAPP After expression and purification, 300 μl of each sample, dissolved in HFIP, were put aside. The aliquots had concentrations of 120 μM and 95 μM, respectively. The samples were lyophilized and dissolved in 300 μl MES buffer and 15 μl D_2O. One ^{15}N-HSQC and one ^{13}C-HSQC were acquired for each sample. The ^{15}N-HSQC experiments were acquired with 32x200 scans in 2 hours. The ^{13}C-HSQC experiments were acquired with 128x256 scans in 14 hours.

2.6.2 Solid-state NMR experiments

Fibril pellets were filled into 3.2 mm thin-wall Varian rotors with a sample volume of 36 μl and a sample spacer for liquid samples. It has to be noted here, that ultracentrifugation, which was used for former samples, is much more efficient for pelletization than centrifugation of the sample in falcon tubes in the swing-out rotor in the Eppendorf 5804 R centrifuge.
The experiments performed on the samples are listed in Table 3.1. A number of 2D ^{13}C-^{13}C experiments was performed at a VT gas temperature of 0°C. External referencing to an adamantane sample was done. Each experiment started with an initial ^{1}H-^{13}C Hartmann-Hahn cross-polarization step, and SPINAL decoupling was applied as decoupling sequence. The pulses were

calibrated first with an adamantane sample, and again on the protein samples. The calibration of the ^{1}H pulse was done at fixed proton power level in a CP-experiment. The proton pulse length was optimized to yield an 180° pulse, i.e. to observe no signal in the CP-spectrum. Half of the pulse length was used as a 90° pulse. Subsequently, the 90° ^{13}C pulse was calibrated in an CP-experiment followed by a 90° pulse on carbons. The 90° pulse length was reached, when a zero crossing of the spectrum in the aliphatic region was observed.
Experimental data were processed with NMRPipe and analyzed with CcpNMR analysis.

DNP experiments on 1,^{13}C labelled IAPP On the first TEASE-labelled sample, ssNMR experiments with dynamic nuclear polarization (DNP) were performed. The DNP sample was prepared from 20 μl fibril pellet. It was resuspended with 60 μl D_2O and centrifuged at 14 000 rpm for 20 minutes. Two more washing steps with D_2O were done. The resulting pellet was dissolved in 5 μl of 100 mM AMUPol/D_2O stock solution (Table 2.14). 30 μl of d_8-glycerol were added and a total sample volume of 25 μl filled into a 3.2 mm zirconia rotor from Bruker. The sample was cooled to 120 K during DNP experiments. Several PDSD experiments with MAS of 8 kHz or 9 kHz were performed. Homonuclear ^{13}C-^{13}C mixing was applied for 5 seconds. 256 scans per increment and 140 2D increments were used. The initial cross-polarization time from ^{1}H to ^{13}C was set to 100 μs (p15).

2.7 Structure calculation

2.7.1 Tertiary contacts in PDSD spectra

On the diluted labelled (1:4) and the uniformly labelled sample, PDSD experiments with 800 ms mixing times were performed. The diluted sample was measured in an 800 MHz Varian spectrometer at 11 kHz MAS and with 448x230 scans. The fully labelled sample was measured in a 600 MHz Varian spectrometer at 11 kHz MAS with 736x200 scans. All experiments were performed at 0℃ VT gas temperature. Four ambiguous cross-peaks from the diluted sample were chosen as valuable restraints for the structure calculation. They were verified by also finding them in a 500 ms mixing time PDSD, acquired at an 600 MHz spectrometer. The cross-peaks are indicated in Figure 3.23.
Additionally, one cross-peak was observed only in the uniformly labelled sample. This was interpreted as an inter-molecular cross-peak. It is also indicated in Figure 3.23.

2.7.2 Cyana structure calculation of a monomer

The simulated annealing program Cyana was used for an initial structure calculation. The calculation was performed on given distance restraints and TALOS-N dihedral angles. An automated peak assignment was not performed.
Two fibril layers were simulated, with one monomer per fibril layer. The stacked β-strands of the molecules from the two fibril layers form β-sheets. The two monomers were stacked in a parallel-in-register alignment on top of each other.
The characteristic requirements for the Cyana input file are not described here in detail. There is a comprehensive documentation available in the internet (`www.cyana.org`), that also contains several tutorials. In the following, the parameters chosen for the current simulation are explained. If a structure calculation from given distance restraints is done, seven input files are required, as described in the following.

.seq file In the sequence file, the primary sequence is defined. There is only one sequence per run, but individual molecules can be separated by invisible linkers. In this model, monomer one runs from residue 1 to 37 and monomer two from 201 to 237. The linker molecule spanning residues 98 to 130 was chosen to be 31x2 Å in length. The oxidized state of the cysteine residues is denoted by writing `CYSS`.

Calc.cya In the Calc.cya file, the input files for the run are listed. Furthermore, the user can influence the performance of the simulation by choosing the number of structures created and the number of steps. 100 initial structures were generated and 10000 MD steps chosen.

init.cya The β-strand building segments were defined by a parameter called *welldefined*. As two molecules are defined and they are expected to have an identical conformation, identity con-

straints were generated for the *welldefined* regions. This leads to the automatic generation of 87 identity constraints, when the program is started. The weight of the identity constraints was chosen as 0.15.
The two monomers were defined and attributed to their corresponding residue range in the sequence. The invisible linker molecules are not included in the definition of the molecules.

.prot file A numbered list in XEASY file format containing all chemical shifts found experimentally. Equal chemical shifts were defined for residues 1-37 and 201-237. In the current calculation, chemical shifts were defined for carbon and nitrogen nuclei. No hydrogen chemical shifts were defined, as they were not detected in the solid-state NMR experiments.

.aco file The torsion angle restraint file contains the dihedral angles ϕ and ψ and their respective standard deviation, as yielded from TALOS-N. Only predictions were used, that TALOS-N denoted as *strong*. Again, equal dihedral angles were used for region 1-37 and 201-237.

.upl file This file contains the upper distance limits. In this model, two different kinds of upper distance limits were defined.
The first type are distance limits characteristic of a parallel-in-register β-sheet. The distances in between NH and CO groups of adjacent β-strands are known to be 1.8-2 Å for $O_{i,n}$-$H_{j,n+1}$ and 2.7-3 Å for $O_{i,n}$-$N_{j,n+1}$. These distance restraints were implemented for all regions, which were declared to belong to the *welldefined* segments in the `init.cya` file. The defined spacing of the adjacent β-strands in a β-sheet is seen in a simplified way in Figure 2.7.
The second type of distance restraints are ambiguous intra-molecular restraints, that define the tertiary fold of the monomers. The intra-molecular disulfide bridge in the N-terminus was defined for both molecules, and four ambiguous distance constraints were included. The four peaks from which these constraints were deduced are shown in Figure 3.23 and listed in Table 3.2.

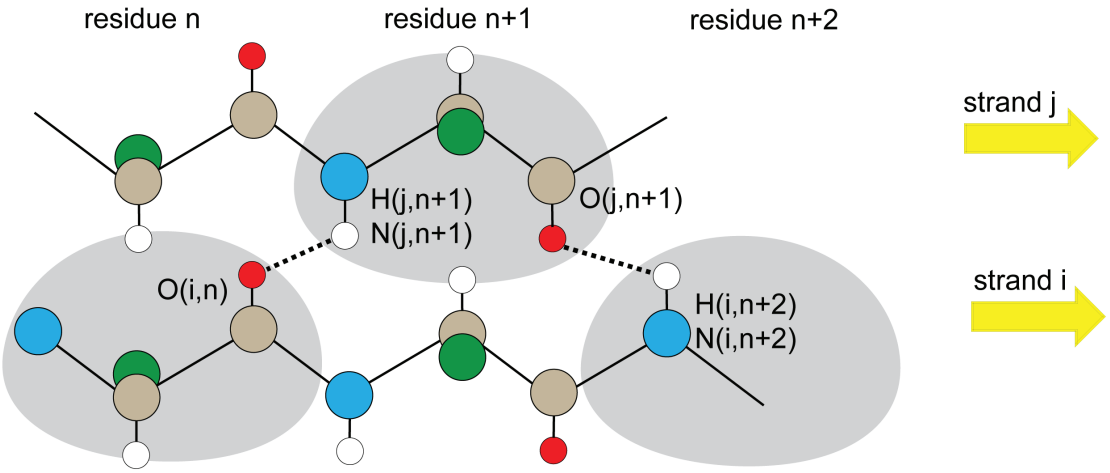

Figure 2.7: *Simplified illustration of two β-strands in an in-register-parallel β-sheet. Characteristic inter-molecular hydrogen bonds in between strands i and j are shown.*

.lol file In this file, the lower distance limits were defined, i.e. all entries from the *.upl file appear in this file with their corresponding lower distance limit. The lower distance limit of $O_{i,n}$-$H_{j,n+1}$ was set to 1.8 Å and to 2.7 Å for $O_{i,n}$-$N_{j,n+1}$. The lower distance limits of the ambiguous distance restraints were set to 1.8 Å.

The corresponding input files for the simulation of two identical monomers stacked on top of each other are shown in the Supporting information on page 88.

2.8 Buffer recipes

M9 medium	per liter
M9 salts (5x)	200 ml
$CaCl_2$	200 μl (0.5 M stock)
$MgSO_4$	2 ml (1 M stock)
Ampicillin	1 ml (100 mg/ml stock)
(1)-^{13}C **or** (2)-^{13}C Glucose	3 g
$^{15}NH_4Cl$	2 g
Biotin	2 ml (0.5 mg/ml stock)
Thiamin	1 ml (1 mg/ml stock)
Ammonium Ferric citrate	1 ml (20 mg/ml stock)
Trace elements	10 ml (100x)
Unlabelled amino acids (N,T,K,I,Q,R)	150 μg/ml M9 each
MilliQ	fill to 1 liter
autoklave	

Table 2.1: *M9 medium used for selective and extensive labelling*

50 mM Tris stock	per 2 liters	final conc.
Tris	12.2 g	50 mM
NaCl	23.36 g	200 mM
adjust pH	8	
MilliQ	fill to 2 liters	

Table 2.2: *Tris stock for purification*

Lysis buffer	per 50 ml	final conc.
Tris stock	50 ml	50 mM
Lysozym	10 mg	
DNAse I	spade point	
PMSF		0.1 mM

Table 2.3: *Lysis buffer*

500 mM Imidazole buffer	per liter
50 mM Tris stock	1 liter
Imidazole	34 g
adjust pH	to 8

Table 2.4: *500 mM Imidazole buffer*

10 mM Imidazole buffer	per liter
50 mM Tris stock	980 ml
500 mM Imidazole buffer	20 ml
pH	8

Table 2.5: *10 mM Imidazole buffer*

HPLC buffer A	per liter
MilliQ	1 liter
Trifluoroacetic acid	1 ml

Table 2.6: *HPLC buffer A*

HPLC buffer B	per liter
MilliQ	800 ml
Acetonitrile	200 ml
Trifluoroacetic acid	1 ml

Table 2.7: *HPLC buffer B*

HPLC buffer D	per liter
MilliQ	700 ml
Acetonitrile	300 ml
Trifluoroacetic acid	1 ml

Table 2.8: *HPLC buffer D*

Fibrillation buffer	per liter	final conc.
NaH_2PO_4-H_2O	1.38 g	10 mM
NaCl	0.88 g	15 mM
adjust pH to 7.4	using NaOH	
NaN3		3 mM

Table 2.9: *Fibrillation buffer for ssNMR samples*

MES stock	per liter
MES (free acid)	97.6 g
adjust pH to 6	using 10N NaOH

Table 2.10: *0.5 M MES stock*

NaPi	per liter
NaH_2PO_4-H_2O	10 mM or 50 mM
adjust pH to 6 or 7.4	using NaOH or H_3PO_4

Table 2.11: *NaPi for ThT kinetics*

50 mM Tris	per liter
Tris	6.05 g
adjust pH to 7.4	using HCl

Table 2.12: *Tris for ThT kinetics*

HEPES 50 mM	per liter
HEPES	11.9 g
adjust pH to 7.4	using NaOH

Table 2.13: *HEPES for ThT kinetics*

AMUPol D_2O stock	
AMUPol	1.5 mg
D_2O	20.66 μl

Table 2.14: *AMUPol 100 mM stock*

2.9 Random-coil chemical shifts

Random-coil chemical shifts are used for the calculation of secondary chemical shifts $\delta_{sec} = \delta_{exp} - \delta_{rc}$. There are different ways to obtain random-coil chemical shift values. Firstly, random-coil values have been determined experimentally in 1995 by Wishart et al. by NMR examination of model peptides [75]. Secondly, chemical shifts of NMR studies are deposited in the BMRB database [76]. The average values of the deposited chemical shifts can be used as random-coil values. Thirdly, the group of Wishart has generated a revised chemical shifts databank, based on BMRB entries. This databank, RefDB, currently comprises 2162 re-referenced protein chemical shifts [77]. The revised databank is found in `www.refdb.wishartlab.com`. It provides random-coil chemical shifts.

The chemical shift values for Cα, Cβ, CO and backbone amide of all three resources are shown in Figures 2.8 and 2.9. The differences of the Cα and Cβ chemical shift values are shown in Figure 2.10.

For the calculation of secondary chemical shifts, all three resources were used and the results were compared. For cysteine, the chemical shifts for the oxidized form were applied. These are available from Wishart et al. but not from the BMRB database.

Random-coil values, 19.04.2017, RefDB,
http://refdb.wishartlab.com/stat.html

	Ca	Cb	C	N
Ala	52,84	19,06	177,67	123,61
Cys(ox)	55,6	40,97	174,93	117,96
Asp	54,18	40,85	176,31	119,95
Glu	56,87	30,2	176,43	120,43
Phe	57,98	39,45	175,59	119,67
Gly	45,51	0	173,89	109,13
His	55,86	29,97	174,83	118,72
Ile	61,03	38,65	175,57	120,87
Lys	56,59	32,79	176,34	120,45
Leu	54,92	42,38	176,89	121,48
Met	55,67	33,36	175,35	119,66
Asn	53,23	38,55	175,08	118,22
Pro	63,47	31,94	176,89	0
Gln	56,12	29,14	175,9	119,49
Arg	56,42	30,66	176,02	120,42
Ser	58,38	64,03	174,49	115,55
Thr	61,64	70,12	174,7	113,36
Val	62,06	32,71	175,66	119,77
Tyr	57,97	38,95	175,39	119,52
Trp	57,78	29,67	176,15	120,16

Figure 2.8: *Random-coil chemical shifts exported from revised database RefDB, maintained by Wishart et al. [77]*

BMRB, 19.04.2017, filtered list

	Ca	Cb	C	N
Ala	53,181	18,97	176,472	123,27
Cys	58,163	0	174,955	120,082
Asp	54,701	40,87	176,445	120,643
Glu	57,335	29,975	176,92	120,702
Phe	58,148	39,947	175,5	120,37
Gly	45,357	0	173,892	109,595
His	56,523	30,226	175,262	119,686
Ile	61,675	38,577	175,936	121,399
Lys	56,973	32,784	176,722	121,044
Leu	55,694	42,272	177,083	121,816
Met	56,139	32,938	176,234	120,09
Asn	53,562	38,69	175,302	118,902
Pro	63,357	31,853	176,765	0
Gln	56,615	29,172	176,371	119,89
Arg	56,8	30,656	176,472	120,789
Ser	58,753	63,794	174,654	116,269
Thr	62,261	69,708	174,584	115,373
Val	62,572	32,713	175,71	121,081
Tyr	58,181	39,271	175,467	120,458
Trp	57,753	29,958	176,239	121,574

Wishart 1995, random coil values of residues followed by alanine

	Ca	Cb	C	N
Ala	52,5	19,1	177,8	123,8
Cys(ox)	55,4	41,1	174,6	118,6
Asp	54,2	41,1	176,3	120,4
Glu	56,6	29,9	176,6	120,2
Phe	57,7	39,6	175,8	120,3
Gly	45,1	0	174,9	108,8
His	55	29	174,1	118,2
Ile	61,1	38,8	176,4	119,9
Lys	56,2	33,1	176,6	120,4
Leu	55,1	42,4	177,6	121,8
Met	55,4	32,9	176,3	119,6
Asn	53,1	38,9	175,2	118,7
Pro	63,3	32,1	177,3	0
Gln	55,7	29,4	176	119,8
Arg	56	30,9	176,3	120,5
Ser	58,3	63,8	174,6	115,7
Thr	61,8	69,8	174,7	113,6
Val	62,2	32,9	176,3	119,2
Tyr	57,9	38,8	175,9	120,3
Trp	57,5	29,6	176,1	121,3

Figure 2.9: *Average chemical shifts exported from BMRB database and experimentally obtained random-coil values by Wishart et al. in 1995. [76, 75]*

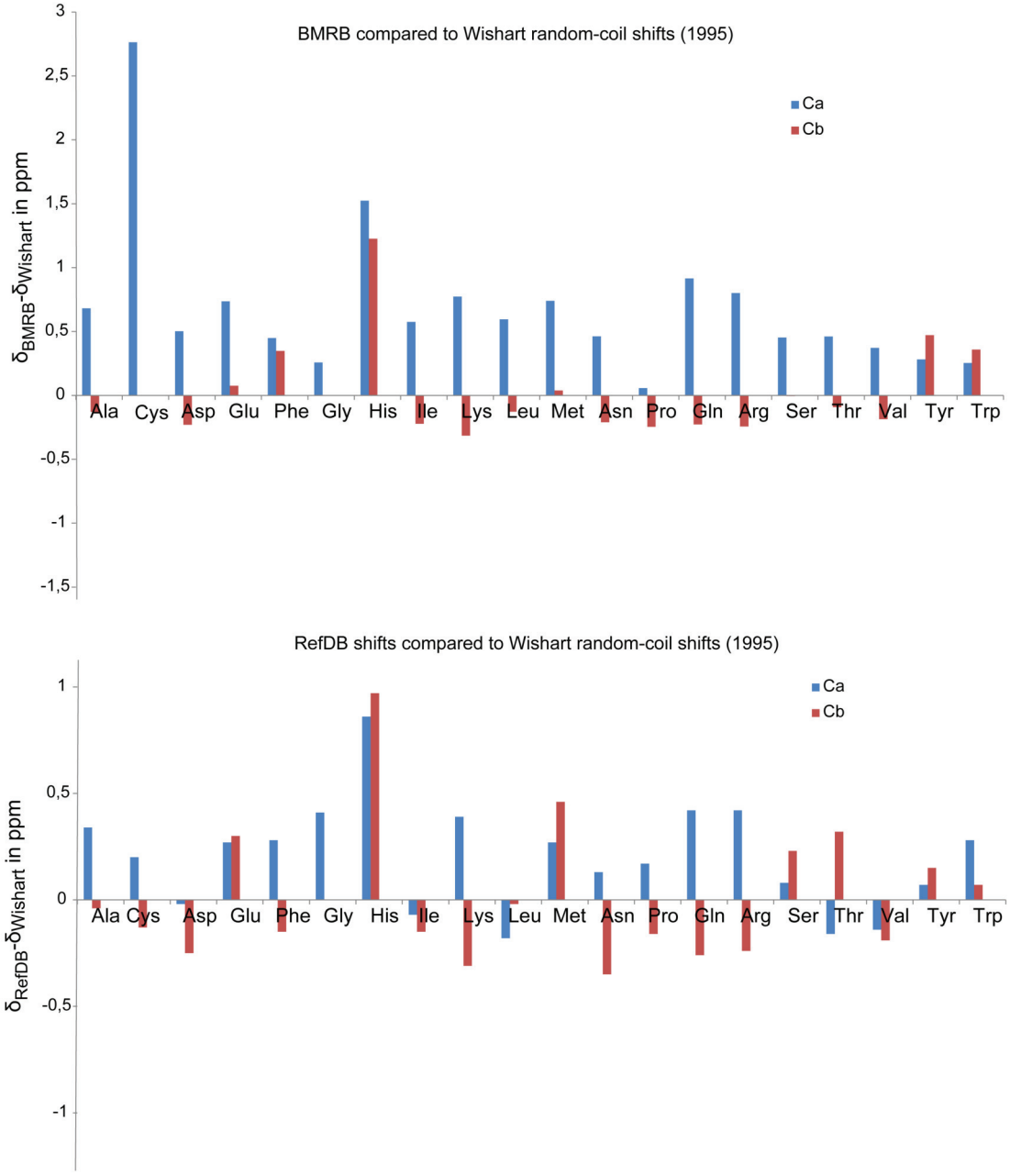

Figure 2.10: *BMRB average chemical shifts and RefDB random-coil chemical shifts compared to random-coil shifts from Wishart et al. 1995.*

3. Results and Discussion

This thesis covers structural studies on fibrillar Islet Amyloid Polypeptide (IAPP, Amylin) by solid-state Nuclear Magnetic Resonance (ssNMR). The 37 amino acid residue peptide was expressed recombinantly in *E.coli* cells, and different ^{13}C, ^{15}N labelling strategies were applied. Due to its high aggregation propensity, Islet Amyloid Polypeptide was expressed as a fusion construct with the stabilizing β-wrapin protein HI18 [59]. After expression, the fusion construct was cleaved proteolytically and removed by reversed-phase high-performance liquid chromatography (RP-HPLC). IAPP in its free-acid form, i.e. IAPP$_{COOH}$, with an intact N-terminal disulfide bridge was obtained from this expression system. Prior to fibrillation, the lyophilized peptide was dissolved in hexafluoroisopropanol (HFIP) to dissolve any preformed aggregates and start fibrillation from monomeric IAPP. Seeded fibrillation under intermittent sonication was conducted at pH 7.4, with spontaneously generated aggregates serving as initial seeds. This fibrillation protocol was expected to yield a homogeneous fibril morphology [33].

The first part of the ssNMR study was performed on three samples with two different ^{13}C and ^{15}N labelling schemes. Two samples were used for *conventional* ssNMR and the third sample for dynamic nuclear polarization (DNP) ssNMR experiments at 100 K. The first labelling scheme is a uniform ^{13}C, ^{15}N labelling, and the second one a diluted labelling, with a ratio of uniformly labelled to unlabelled peptide of 1:4. The diluted sample was prepared by mixing labelled and unlabelled fractions before fibrillation started. The DNP sample was prepared by dissolving uniformly labelled fibrils in DNP juice (Table 2.14) to a final volume ratio of 10:30:60 (sample:D_2O:d_8-Glycerol), and a final concentration of 20 mM AMUPol [93].

The analysis of the solid-state NMR experiments led to a complete sequential resonance assignment. The chemical shifts were used for a secondary structure analysis by TALOS-N [79]. The predicted dihedral angles ϕ and ψ reflect a predominant β-structure of the fibrils. Three β-strands are found, located at positions (8-20), (23-32), and (35,36). Residue Ser-29 is less constrained, as it shows a second, less pronounced, C_β chemical shift. This may indicate a disruption of the second β-strand for a fraction of fibrils, or an alternative way of forming hydrogen bonds. The N-terminus ^{1}KCNTATCA^8 of IAPP is clearly observed in spectra. It shows an intermediate flexibility, i.e. a higher flexibility than residues in extended β-conformation, but is more constrained than a random-coil loop. Up to this point, results have been published in 2016 [19]. The text of the publication and the figures are included in this thesis on pages 23 to 26 and 44 to 61 with minor adaptions in wording and formatting.

After the site-specific resonance assignment and the analysis of secondary structure, the subsequent experiments focused on the detection of long-range through-space contacts, which contain indispensable information for a structure calculation. Through-space contacts contain information on the tertiary fold of a protein. Cross-peaks arising from amino acids that are more than two residues apart in the sequence, are not caused by magnetization transfer along the protein backbone. Indeed they are observable, because the spatial conformation of the molecule causes through-space dipolar couplings in between the spins. In a structure calculation, through-space cross-peaks can be correlated with an upper distance limit between the observed nuclei. The applied upper distance limit depends on the pulse sequence and the mixing time applied and ranges from 6 to 10 Å [11].

There are several obstacles regarding the detection of such structurally important cross-peaks. First, the effect of dipolar truncation, that is the attenuation of a weak dipolar coupling in the presence of a strong dipolar coupling. It is caused mainly by labelled neighboring spins and impedes the detection of weak dipolar couplings [16].
The second hindrance is the ambiguity of the detected cross-peaks. Due to overlap of resonances, the δ_1 and δ_2 values of a cross-peak are in the majority of cases not unambiguously assignable.
Labelling approaches, which result in a reduction of labelled spin systems, or in the dilution of labelled spins, are efficient methods to reduce the impact of these effects.

In this thesis, the first approach to obtain tertiary structural information was to reduce the effect of dipolar truncation by application of a selective and extensive labelling scheme, called TEASE labelling [95]. This labelling strategy yields a diluted distribution of spins in the sample, with no neighboring labelled spins, and additionally erases several spin systems completely from the spectra. As a result, long-range contacts should be observable in ^{13}C-^{13}C correlation spectra, and the spectral overlap and ambiguity should be reduced.
Complementary to the selectively and extensively labelled samples, the uniformly labelled and the diluted sample were further examined by ^{13}C-^{13}C correlation experiments with mixing times above 500 ms. In the corresponding spectra, new peaks were observed, that were not visible in previously recorded spectra of 200 ms mixing time. Four cross-peaks were selected and ambiguous intra-molecular distance restraints created. These were used as constraints in a first structure calculation with the simulated annealing program Cyana [20].

Complementary to the preliminary structural model from the Cyana simulation, two theoretical structural models were built. They are based on the results of secondary structure analysis and on an evaluation of the reduced cross-peak intensity of several spin systems in PDSD spectra.

3.1 Site-specific resonance assignment

Pages 44 to 61 are taken from *Weirich et al., PLoS ONE 11(9): e0161243*.

Solid-state MAS NMR experiments were performed at magnetic fields of 14.1 Tesla and 18.8 Tesla on a uniformly ^{13}C, ^{15}N-labelled sample. In cross-polarization based spectra [99], exhibiting only the rigid parts of the sample, line-widths ranging from 0.8 ppm to 1.3 ppm in the ^{13}C dimension and below 3 ppm in the ^{15}N dimension were observed for well-resolved signals in 2D spectra. These line-widths are comparable to those observed for spectra of other fibril preparations of non-functional amyloids [100, 33, 101, 13, 102]. In an initial INEPT experiment [82], performed at a sample temperature of circa 10 °C, no signal was observed. The lack of signal in this J-coupling based transfer scheme indicates that all 37 amino acid residues of the peptide, including the N-terminal disulfide-bridged loop, lack high flexibility [100, 103].

Full sequential resonance assignments were obtained from a set of 2D and 3D ^{13}C, ^{13}C and ^{15}N, ^{13}C correlation experiments. The experimental details are listed in Table 6.1 and the experimentally obtained chemical shifts in table 6.2 on pages 93 and 94 [104, 87, 88]. In Figure 3.1, the aliphatic region of a PDSD spectrum with 20 ms longitudinal mixing time is shown, and resonance assignments are indicated. Most of the 37 amino acid residues gave rise to one single set of resonances, and site-specific resonance assignments could be obtained from inter-residual cross correlations. These were observed in PDSD spectra recorded close to the rotational resonance condition between the CO and the Cα region and are shown in Figure 3.2 [104].

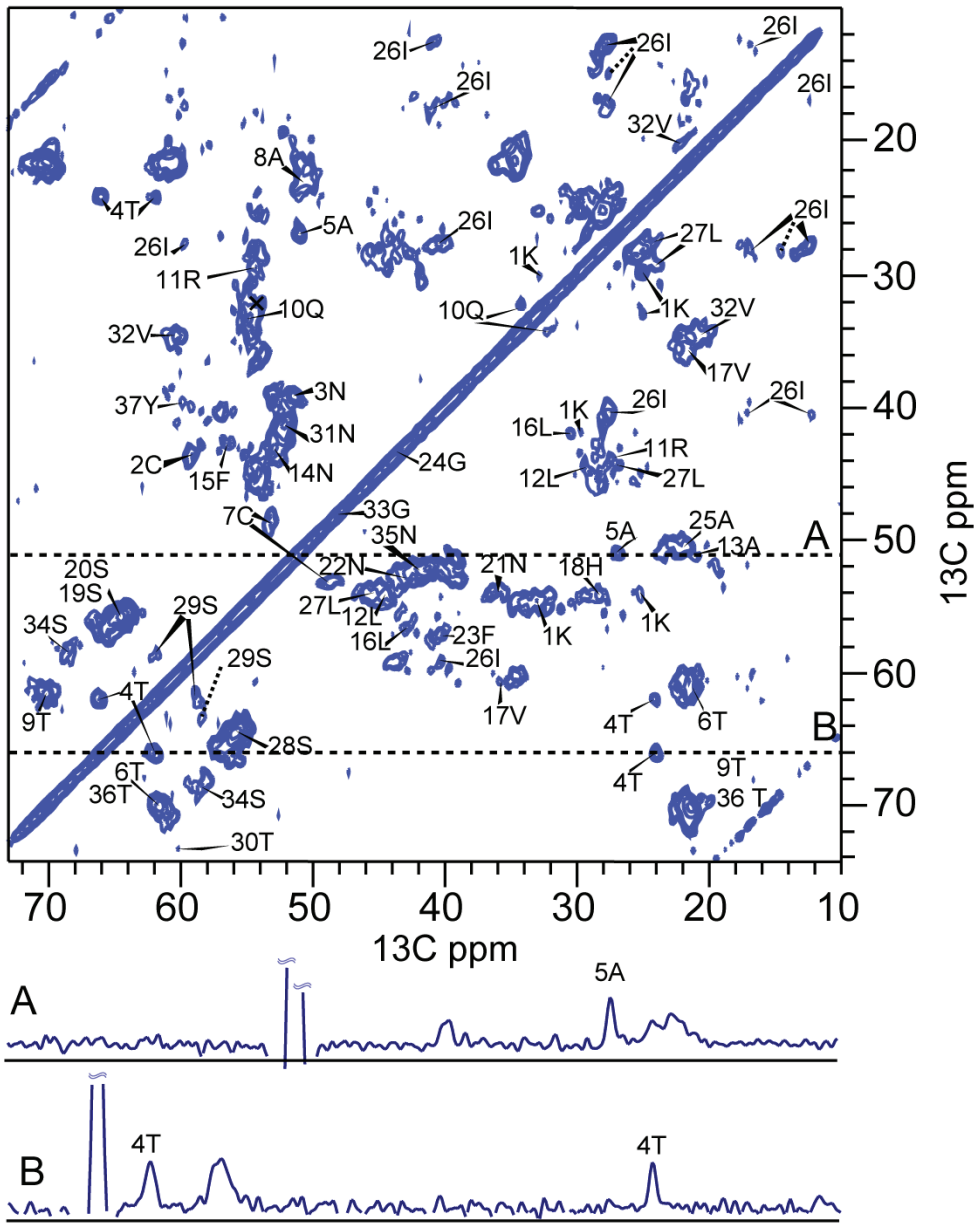

Figure 3.1: *Proton-Driven Spin-Diffusion spectrum. The spectrum was recorded at a field of 18.8 Tesla with longitudinal mixing time of 20 ms and spinning speed of 11 kHz. Sequential assignments shown are based on a number of experiments and brought together in this figure. There are two cross-sections drawn underneath, taken at the positions indicated by dotted lines. The dashed pointers mark the additional peaks found for Ile-26 (Cδ1) and Ser-29 (Cβ). (PLoS ONE 11(9): e0161243)*

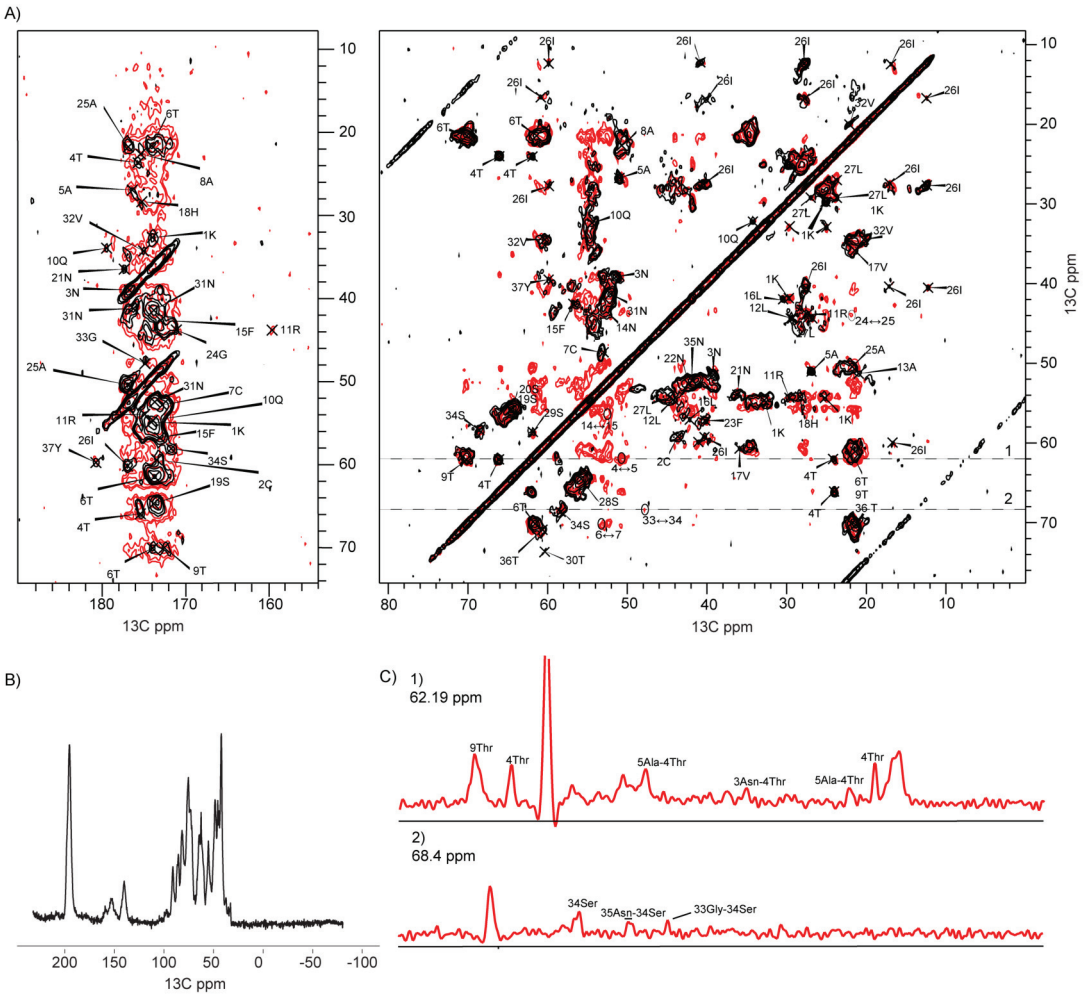

Figure 3.2: *PDSD spectra with short and long mixing times. A) Proton-Driven-Spin-Diffusion (PDSD) spectra recorded at a field of 18.8 Tesla with longitudinal mixing times of 20 ms (black) and 200 ms (red) and spinning speeds of 11 kHz and 12.5 kHz respectively. The VT gas temperature was set to 0 ℃ in both experiments. Short mixing time (20 ms) provides mainly intra-residual peaks, while long mixing time (200 ms) at spinning close to rotational resonance condition shows many inter-residual peaks. Assignments shown are based on a number of experiments and brought together in this figure. Inter-residual cross-peaks connecting Thr-4 and Ala-5 as well as Ser-34 with its neighboring residues are indicated. B) Spectrum of the first FID of the 20 ms PDSD spectrum. C) Two cross-sections of the 200 ms mixing time spectrum as indicated by dashed lines in section A). ((PLoS ONE 11(9): e0161243))*

Furthermore, inter-residual cross correlations were obtained from a combination of 3D NCOCX, NCACX, and NCACB spectra. The ^{15}N, ^{13}C correlation spectra were used for a sequential walk along the backbone amide for sequential assignment, as seen in Figure 3.3. The majority of residues gave rise to intense cross-peaks in PDSD spectra, which points to strongly dipolar coupled spins and thus a rigid conformation. Less intense Cα-Cβ cross-peaks appeared for amino acid residues Leu-16, Val-17, Ile-26, Thr-30, Ser-34, and Tyr-37. At these sites, the conformation might be less constrained than at sites which showed more intense peaks, thus either resulting in higher flexibility or increased conformational heterogeneity. At position Ile-26, the Cα-Cβ cross-peak was scattered over a range of 1.5 ppm. Likewise, for Ser-29, a slight degree of peak doubling, resulting from some scatter of the Cβ chemical shift was observed. The main peak was observed at Cβ of 61.7 ppm, but a minor conformation also showed a Cβ shift of 63.7 ppm. This suggests some residual disorder in the region 26-29. Furthermore, for Ile-26, two distinct Cδ1 signals, an intense (12.4 ppm) and a weak one (14.4 ppm), were observed. The weak signal is marked by a dashed line (Fig 3.1). While a shift of circa 14.8 ppm or higher is found to be typical of a 100$\%$ population of the all-trans conformation of the χ2 dihedral angle [105], a shift of 12.4 ppm is close to the average chemical shift value determined by solution NMR [75], which is indicative of a free rotation around the bond connecting Cβ and Cδ1. Thus, for a small fraction of monomers, the Ile-26 sidechain appears to be rotationally constrained to one conformation, while free sampling of the χ2 space seems possible for the larger fraction. Residue Ser-34 is the only residue that was completely absent from the 3D NCOCX spectrum which was recorded using a weak spin-lock on ^{13}C (circa 5 kHz). This also points towards a different degree of flexibility at this site as apparent from accelerated T1ρ relaxation (see below). Its neighboring residues Gly-33 and Asn-35 were however well observed in this experiment.

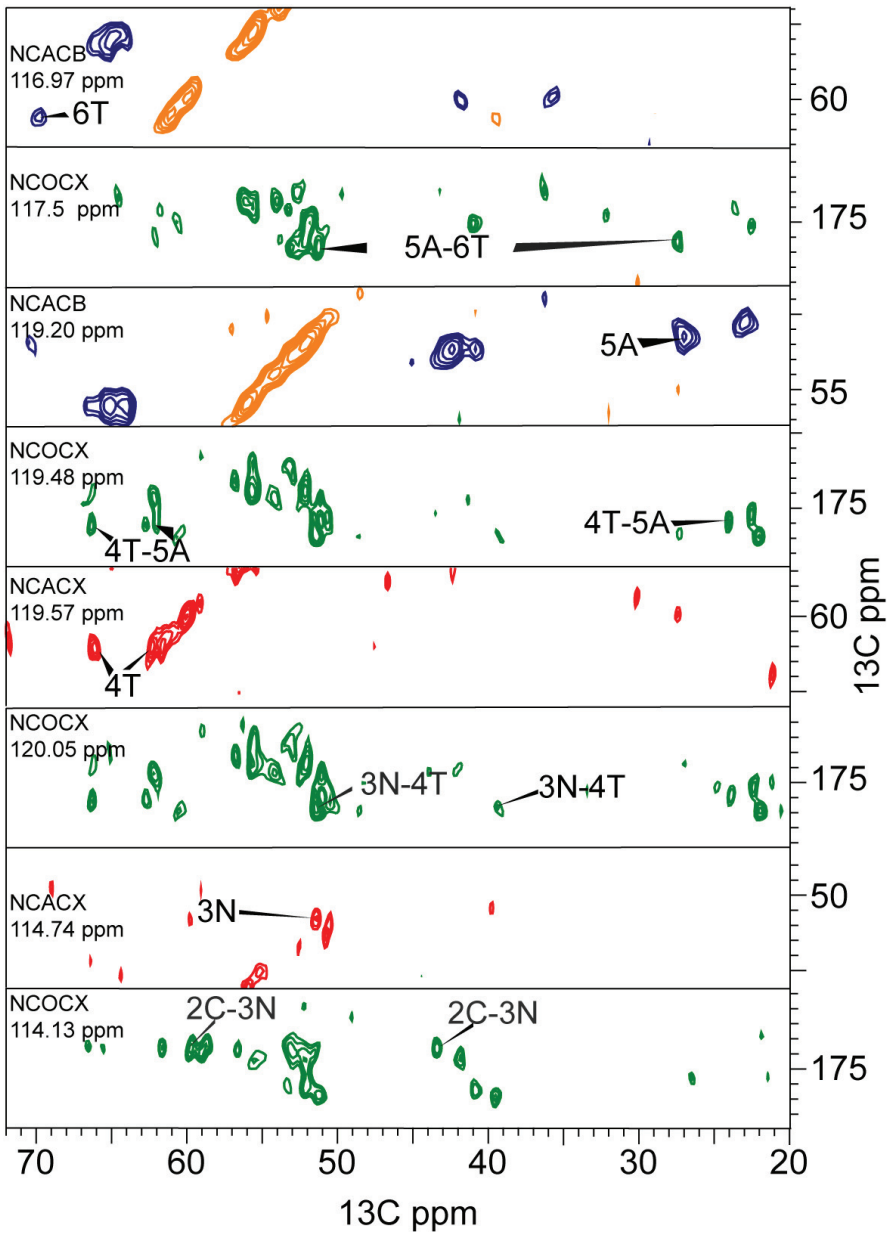

Figure 3.3: *Sequential walk in the N-terminus via backbone nitrogen chemical shifts. The orange and blue peaks belong to a 3D NCACB spectrum (positive, negative) acquired at 14 kHz MAS at 14.1 Tesla. Red peaks belong to a NCACX 3D spectrum recorded at 14.1 Tesla and 11 kHz MAS spinning. Green peaks come from a 3D NCOCX experiment acquired at the same spectrometer at 14 kHz MAS spinning. All experiments were performed at a nominal sample temperature of 10 ℃. Reading from up to down, a spin system i is assigned to its backbone nitrogen shift in the upper strip. In the strip underneath, the preceding residue (green peaks) $i-1$ appears at the same nitrogen shift as found above. Deviations of up to 0.7 ppm appear due to the line-widths of the nitrogen chemical shifts. (PLoS ONE 11(9): e0161243)*

3.1.1 N-terminal residues

Surprisingly narrow ^{13}C line-widths of 0.8 ppm and intense peaks were observed for the N-terminal amino acid residues Asn-3 to Thr-6, which, together with Cys-2 and Cys-7, form a disulfide bridged N-terminal loop. The presence of the intra-molecular disulfide bridge was confirmed by RP-HPLC, based on different retention times for oxidized and reduced IAPP, before fibrillation. The corresponding RP-HPLC chromatograms are shown in Figure 2.1 in the materials and methods section. As a result of the loop structure, the chemical shifts of Asn-3, Thr-4, and Ala-5 differed decidedly from those of the same residue types in the remainder of the sequence. In particular, the Cβ resonance of Ala-5 exhibited a strong positive shift to a value of 26.8 ppm. The oxidation state of the disulfide bridge also strongly influenced the Cβ chemical shifts of the two cysteine residues [106]. Their Cβ shifts were highly shifted to values of 43 ppm and 49 ppm. The signal intensities for residues Asn-3, Thr-4 and Ala-5 varied in ^{15}N, ^{13}C correlation experiments, depending on the ^{13}C spin lock field applied during the second cross polarization step. For radiofrequency-fields on ^{13}C with a nutation frequency below 7 kHz, ^{15}N, ^{13}C cross correlation signals appeared weak, whereas for spin-lock fields with a frequency higher than 15 kHz, the intensity was as good as for other residues. This enhanced T1ρ relaxation at low spin-lock fields may be an indication of additional slow dynamics of the N-terminal loop in contrast to the other residues in the sequence [107]. At extremely low temperatures around 100 K, when all residual motions are frozen out, signals of NMR spectra are inhomogeneously broadened by the resulting conformational disorder. In Figure 3.4, an overlay two ^{13}C, ^{13}C double quantum correlation spectra of fibrillar IAPP at circa 10 °C and at 100 K is shown. While the signals of all residues are affected by line broadening, this effect is most pronounced for residues of this loop. In particular, the line-broadening for the cross correlations of the Cα-Cβ correlation of amino acid residue Ala-5 is broadened beyond detectability. A similar effect has been observed in a previous study by Luca et al., where lyophilization of the sample had the same effect [33].

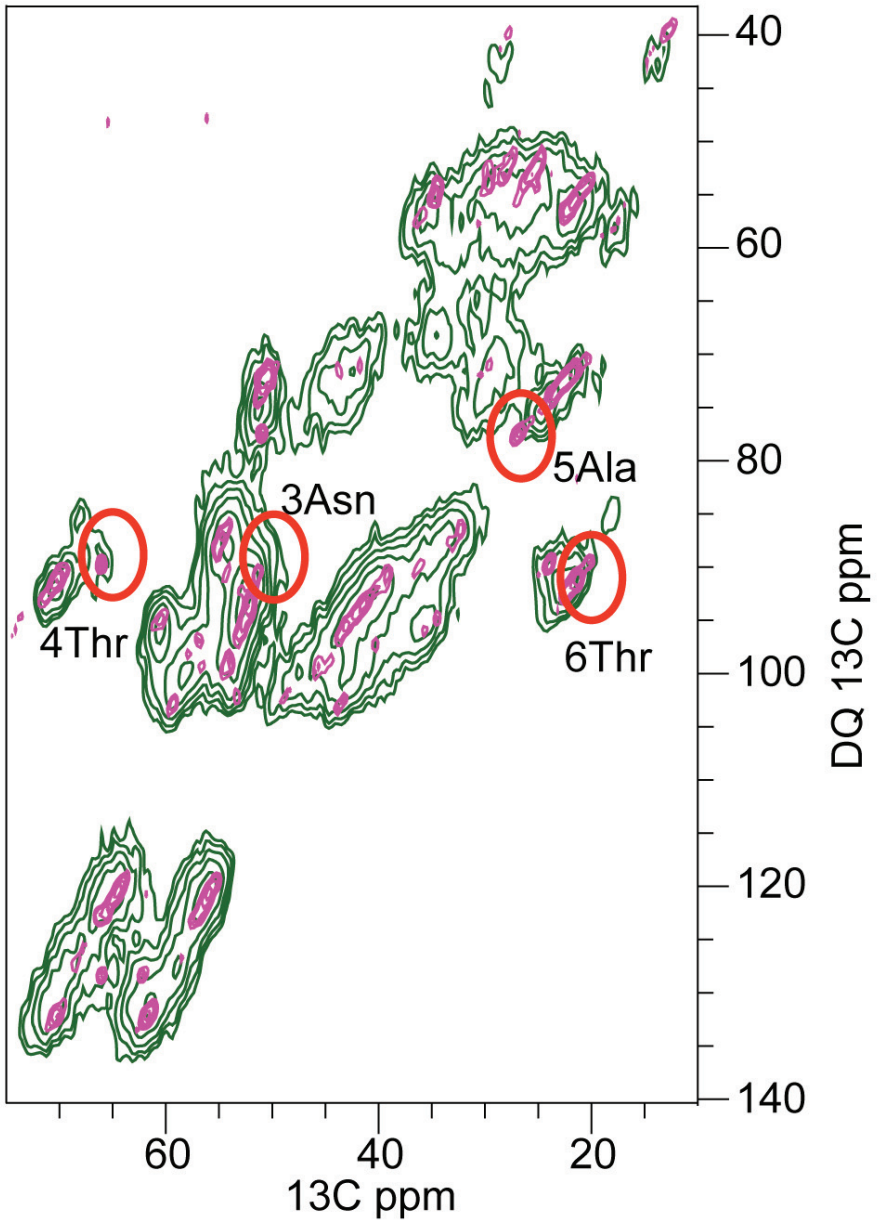

Figure 3.4: *The effect of low temperature and hyperpolarization on the sample. Overlay of 2D Single-quantum double-quantum spectra recorded at magnetic fields of 14.1 T. The green spectrum was acquired with Dynamic-Nuclear Polarization (DNP) at 100 Kelvin nominal sample temperature and $SPC5_2$ recoupling at 8 kHz MAS. The purple spectrum was acquired with conventional solid-state NMR technique at 0 ℃ nominal sample temperature with $SPC5_3$ recoupling at 11 kHz MAS. In the DNP experiment, the sample was frozen out and it is obvious, that the N-terminal $C\alpha$-$C\beta$ cross-peak are broadened due to impeded molecular motion. (PLoS ONE 11(9): e0161243)*

3.1.2 Sample reproducibility

A second fibril sample was prepared under identical conditions for expression, purification and fibrillation. Again spontaneously generated aggregates served as initial seeds. In contrast to the first sample, one part of uniformly ^{13}C, ^{15}N-labelled IAPP$_{COOH}$ was mixed with four parts of unlabelled IAPP$_{COOH}$ prior to fibrillation. The first and the second sample were analyzed in 2D ^{13}C, ^{13}C correlation spectra to compare their chemical shifts. The spectra are shown in Figure 3.5. The cross peaks of most residues coincided, which indicates that two independent fibrillations under equal conditions resulted in fibrils of the same molecular structures, as a different conformation of monomers would result in shifted peaks. Very prominent were again the narrow peaks from the N-terminal residues Asn-3 to Thr-6. They coincided in both samples and again showed intense signals. Thus, also the N-terminus appears to be in the same conformation or cover the same conformational ensemble in both samples. Like in the first sample - the non-diluted uniformly ^{13}C, ^{15}N-labelled IAPP$_{COOH}$- peak doubling for Ser-29 (Cβ) and Ile-26 (Cδ1) was also observed in the second sample. However, the ratios of the signals differed between the two samples, thus ruling out the existence of complex fibrils consisting of monomers with different conformations as observed in [108, 109]. In contrast to the first sample, for Ser-29, the signal with the Cβ shift of 63.7 ppm dominated in the spectrum of the second sample. Likewise, for Ile-26, a Cδ1 chemical shift of 14.8 ppm, indicative of the rigid trans-conformation, was more pronounced than the shift of 12.4 ppm resulting from rotational averaging. Peaks from two additional alanine and threonine spin systems, which could not be integrated into the sequence by means of a sequential walk, were observed mainly in a DREAM spectrum. The DREAM spectrum is shown in Figure 3.6 [87]. We interpret these peaks as a certain amount of impurity in the sample which was not eliminated through the process of purification.

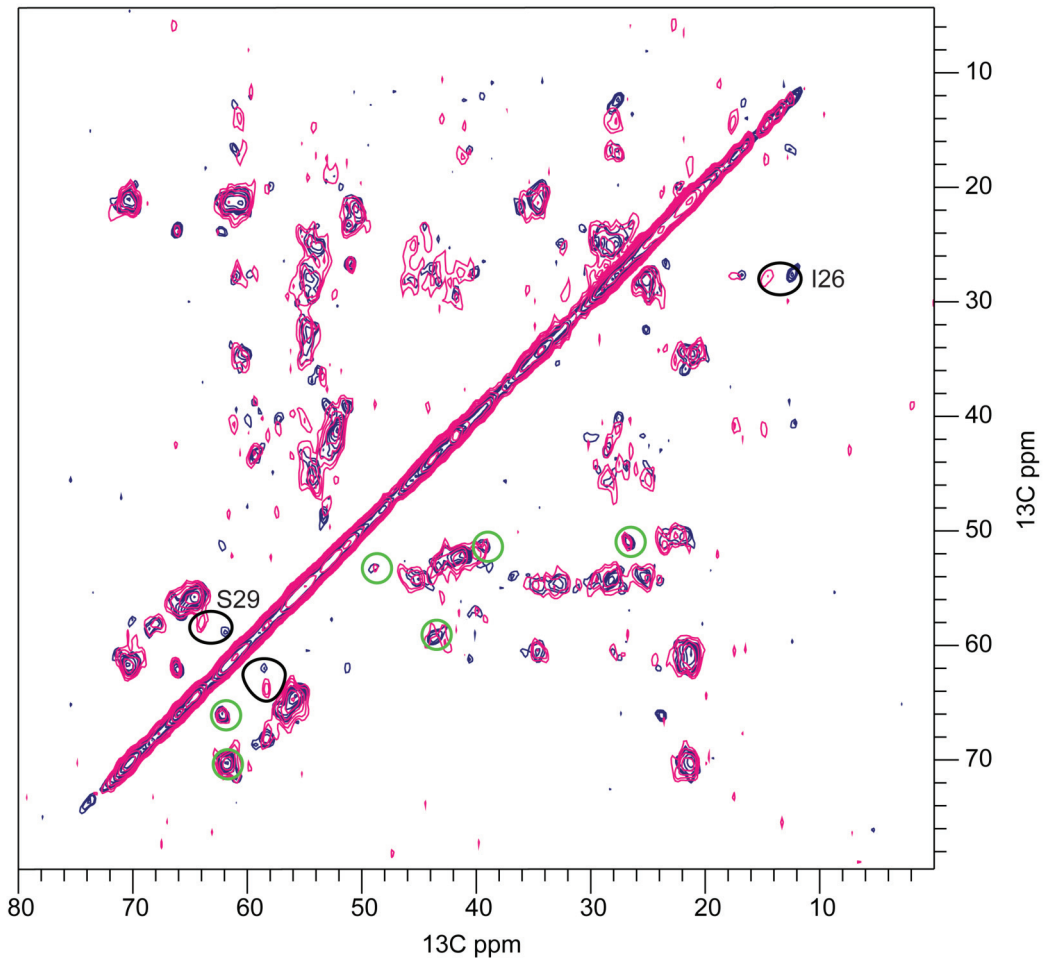

Figure 3.5: *Reproducibility of fibril spectra. Overlay of two PDSD spectra acquired at a field strength of 14.1 T with an MAS spinning frequency of 11 kHz. Longitudinal mixing time was set to 50 ms in both experiments. The spectra were recorded on sample 1 (undiluted, uniformly ^{13}C, ^{15}N-labelled) and sample 2 (1 part uniformly ^{13}C, ^{15}N-labelled IAPP per 4 parts of unlabelled peptide). Blue peaks are from sample 1 (VT = 0 ℃) and pink peaks from sample 2 (VT = -10 ℃). Peaks are coincident for all residues but Ser-29 and the side-chain Cδ of Ile-26. Differences are indicated by black circles. N-terminal residues Cys-2 to Cys-7 show the same chemical shifts in both samples. These residues are marked by green circles. (PLoS ONE 11(9): e0161243)*

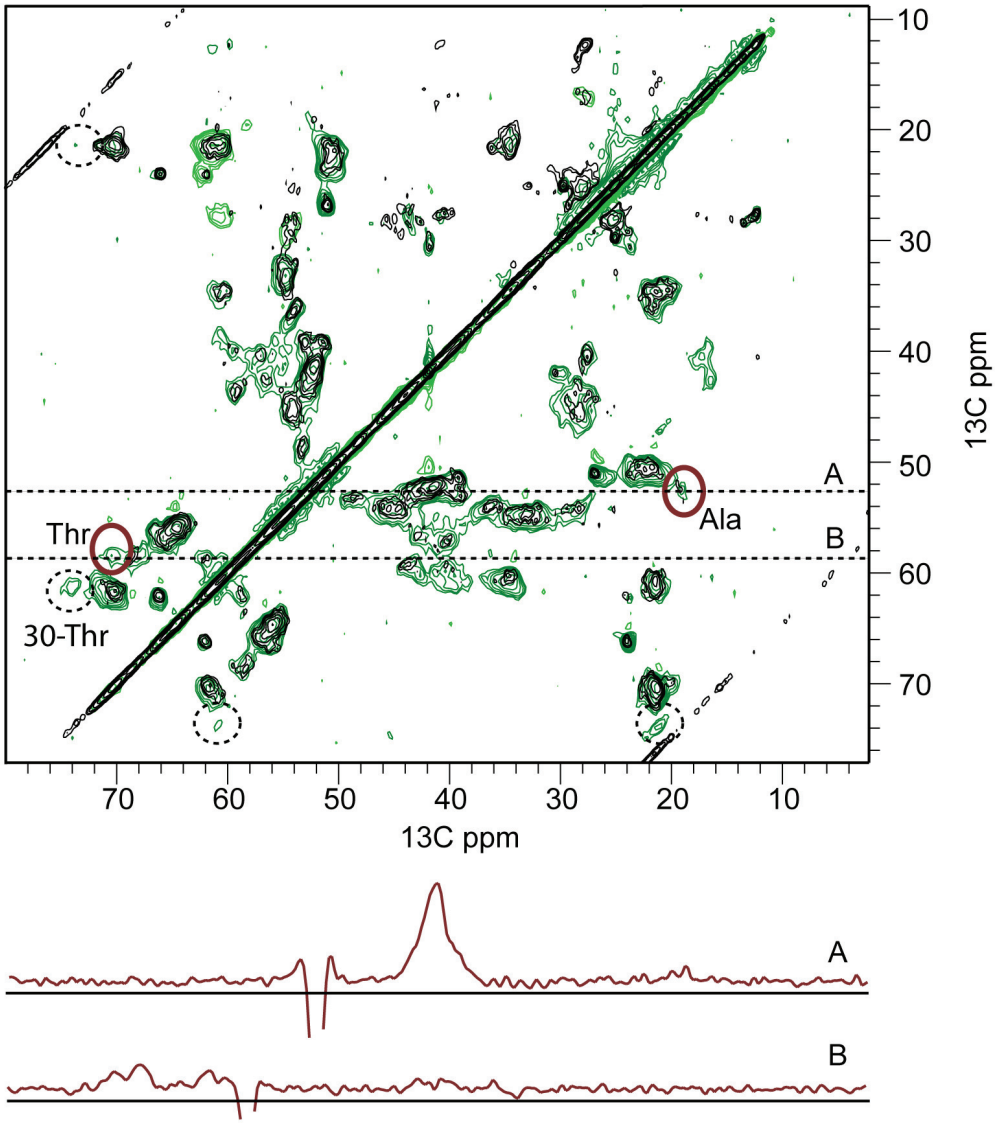

Figure 3.6: *2D DREAM spectrum. Overlay of a 2D DREAM spectrum (green) and a PDSD spectrum with 20 ms longitudinal mixing (black). The DREAM spectrum was acquired at a field strength of 14.1 T with an MAS frequency of 22 kHz. The PDSD was acquired at a field strength of 18.8 T with an MAS frequency 11 kHz. In both experiments, the VT gas temperature was set to 0 ℃. Shown in red are two cross-sections of the DREAM spectrum. They show the impurities which were found in all spectra, but strongest appeared in the DREAM spectrum. The dashed lines indicate the spin system Thr-30, which is better observed in the DREAM spectrum than in PDSD spectra. (PLoS ONE 11(9): e0161243)*

3.2 Analysis of secondary structure

NMR chemical shifts strongly correlate with molecular conformation [110, 78]. The differences of secondary chemical shifts were calculated as

$$\Delta\delta C_{sec} = \Delta\delta C_\alpha - \Delta\delta C_\beta \tag{3.1}$$

with $\Delta\delta C_x = \delta C_x(exp) - \delta C_x(BMRB)$ [74]. The BMRB chemical shift values are listed on page 40. For the amino acid residues Cys-2 and Cys-7, Cβ random coil values of 40.7 ppm were used in the calculation to take into account the oxidized disulfide bridge [111]. Three or more adjacent negative values indicate an extended conformation typical of a β- strand. In Figure 3.7, the secondary chemical shift values are displayed as blue bars. As expected for an amyloid fibril, the whole peptide shows a high degree of β-sheet secondary structure, with only six residues showing a positive value. For a more detailed analysis of secondary structure, all experimentally derived ^{13}C and ^{15}N chemical shifts were used for a TALOS-N prediction of backbone torsion angles [79]. Based on secondary chemical shifts and sequence information, TALOS-N empirically predicts protein backbone torsion angles and a measure of rigidity expressed as RCI S^2 value. No dihedral angles are predicted for residues at first and last position in the sequence. Resulting from the analysis were 35 pairs of dihedral angles ϕ and ψ, of which 30 pairs were classified as strong predictions and 5 as ambiguous. Ambiguous predictions resulted for residues Asn-3, Thr-4, Asn-21, Ser-29, and Gly-33. These were all not part of a β-strand. The dihedral angles are found in Table 6.3 on page 95. Residues were designated as part of a β-strand if TALOS-N predicted the secondary structure with a probability higher than 75%.

Sites for which TALOS-N predicted torsion angles typical for β-strands with a prediction classification as strong, were interpreted as being part of a β-strand. An exception was made for amino acid residues Ala-5, Thr-6 and Cys-7, for which extended conformation was predicted by TALOS, but which cannot be part of an extended β-strand due to their location in the disulfide-bridged loop. They were thus omitted from the first β-strand. According to this analysis, the fibrillar peptide comprises three to four β-strands, i.e. depending on the Cβ shift used for Ser-29, the second and third β-strands are merged to one single strand or not. The strands are located at positions 8 to 20, 23 to 28, 30 to 32, and 35 to 36, as displayed in Figure 3.7. They are interrupted by one or two residues with random coil like conformation. Figure 3.7 also includes a comparison of the findings of our TALOS-N secondary structure analysis with results from former studies [54, 33, 56, 55, 53]. Secondary chemical shifts and TALOS-N results are in agreement, meaning that at positions with positive values, also the β-strands predicted by TALOS-N are interrupted. The only exception is Leu-16, for which TALOS-N predicts torsion angles typical of a β-strand, although this residue has a small positive secondary chemical shift of 0.7 ppm. For this amino acid residue, as well as for the neighboring residue Val-17, Cα-Cβ cross-peaks were less intense than for most other residues assigned to β-strands. This is either because of increased flexibility or increased conformational disorder, an observation which may point to a short perturbation of the β-strand around positions 16/17. However, TALOS-N predicts for both residues torsion angles

which are characteristic of β-sheet conformation.

TALOS-N predictions of backbone angles were classified as ambiguous at the kink positions Asn-21, Ser-29, and Gly-33, as well as for residues Asn-3 and Thr-4 in the N-terminus. The kink residues, connecting the C-terminal two or three β-strands, exhibited specific features. At position Ser-29, depending on the Cβ chemical shift used, the prediction was either random coil (61.7 ppm) or β-strand (63.7 ppm). The second and third β-strand might thus be merged to one single β-strand spanning residues Phe-23 to Val-32. A further reason for the shifted Cβ chemical shift could be that the side-chain hydroxyl group forms a hydrogen bond, either to the protein backbone [112], or to an adjacent serine residue in an intermolecular polar zipper motif [22].

For residue Gly-33, the predicted dihedral angles were widely scattered in the Ramachandran plot. No structural prediction was made based on these angles. As described above, Ser-34 appeared more dynamic due to its divergent behavior compared to its neighbor Asn-35 in NCOCX with weak spin-lock on ^{13}C. We thus interpret Gly-33 and Ser-34 as having a more dynamic behavior than the adjacent β-strands and do not ascribe them as part of such. To further corroborate the extended conformation of the core region predicted by secondary shifts, we performed NHHC experiments [89] with longitudinal mixing times of 50 μs. In extended β-structures, Hα(i) nuclei and HN(i+1) are close in space [113] and should thus yield the strongest cross peaks in a 2D NHHC spectrum for short longitudinal proton mixing times < 100μs [114]. In Figure 3.8 on page 57, sequential N(i+1)-Cα(i) cross-peaks from assigned chemical shifts are plotted for all aa residues of the predicted core regions 8–20, 23–28 and 30–36 and overlaid with an NHHC spectrum obtained with a longitudinal mixing time of 50 μs. Signal overlap due to limited resolution in the indirect dimension prevents an unambiguous resonance assignment of resonances. However, all interresidual N(i+1)-Cα(i) cross-peaks predicted for residues in the β-strands agree well with the spectrum, as well as most of the N(i+1)-Cβ(i) cross-peaks.

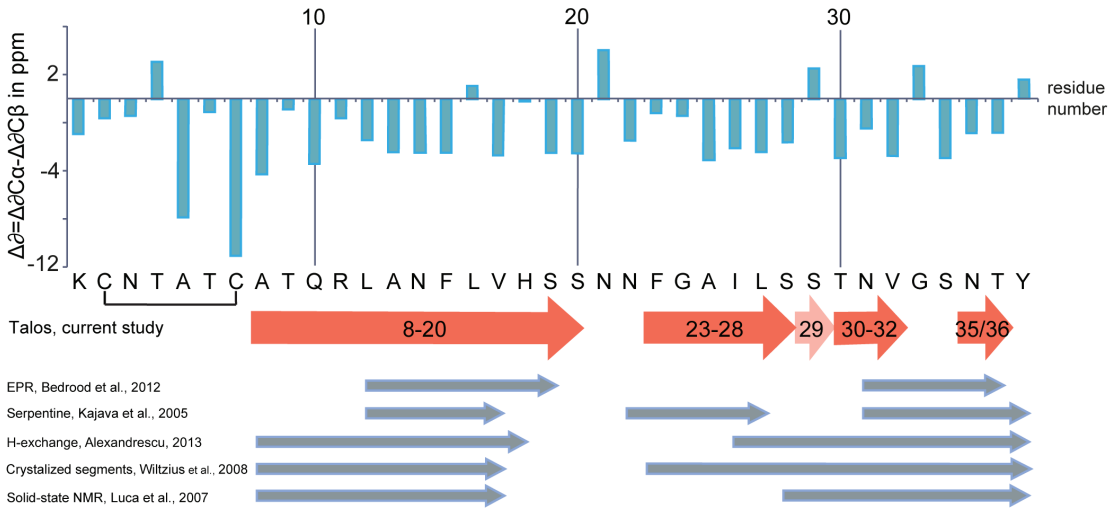

Figure 3.7: *The location of β-strands in fibrillar IAPP. Top: calculated differences of secondary chemical shifts. Two or more adjacent negative values usually are indicative of a β-strand. Bottom: red arrows represent the β-strands predicted by TALOS-N based on NMR chemical shifts from the current study (except for residues Ala-5, Thr-6 and Cys-7, which are part of the disulfide bridged N-terminal loop). Position Ser-29 is found to be structurally less constrained and able to form part of a β-strand in a fraction of fibrils. Grey bars indicate the location of β-strands as determined in previous studies. (PLoS ONE 11(9): e0161243)*

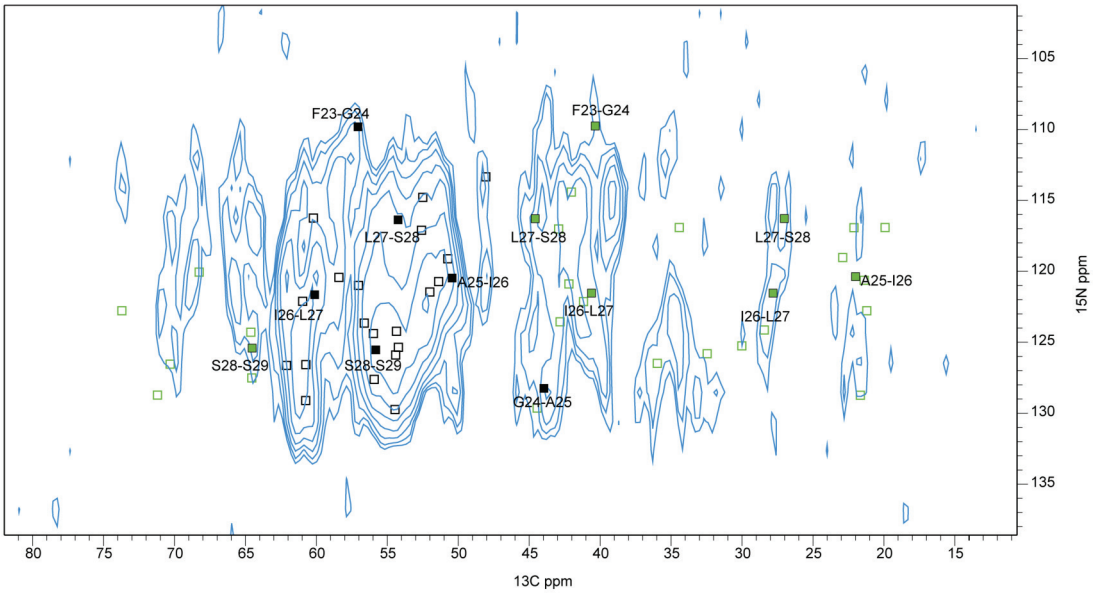

Figure 3.8: *NHHC spectrum with 50 μs proton mixing overlaid with C(i)-N(i+1) cross-peaks. The overlap with sequential ^{13}C(i)-^{15}N(i+1) peaks supports the assumption of a β-conformation in the peptide regions shown. Symbols indicate positions of sequential peaks using chemical shifts from current study. The black peaks are Cα(i) shifts correlated with N(i+1). In green are shown the Cβ(i) or Cγ(i) correlated with N(i+1). The filled symbols represent the FGAILS region IAPP(23–28), open symbols represent cross peaks for residues of regions 8–20 and 29–36. (PLoS ONE 11(9): e0161243)*

3.2.1 Polymorphism in IAPP fibrils

Polymorphism is a feature frequently observed for disease-related amyloid fibrils [115, 100, 34, 116, 9]. Polymorphism often becomes evident when different fibril preparations are compared, but can also occur within a single fibril preparation. AFM images of all samples of fibrillated IAPP$_{COOH}$ revealed short fibrils which were laterally assembled into bundles, consisting of multiple filaments. Thus, no conclusions about sample homogeneity could be drawn from AFM images alone. AFM micrographs of fibrillar IAPP are shown in Figure 3.11 on page 64.

Solid-state NMR experiments on fully ^{13}C, ^{15}N-labelled fibrillar IAPP$_{COOH}$ yielded spectra showing a single set of resonances for the majority of amino acid residues, indicative of high sample homogeneity with a common, rather well-defined conformation of IAPP molecules incorporated into the fibril. Inter-sample polymorphism can be caused by differences in the chemical identity of the amyloidogenic protein (e.g., aa sequence or post-translational modifications) or differences in the fibrillation conditions. To evaluate polymorphism between different IAPP fibril preparations, we compared our data with solid-state NMR data reported by Luca et al. on solid-phase synthesized IAPP$_{CONH2}$ with a residue-specific ^{13}C labeling scheme for unambiguous resonance assignments [33]. An overlay of the chemical shifts obtained from this study and our PDSD spectrum is shown in Figure 3.9. Major differences in chemical shifts were observed for the region spanning residues Leu-27 to Ser-34. For residue Ala-5 and the region Ala-8 to Ile-26, chemical shifts were in reasonable agreement. The unusual chemical shifts of Ala-5 were identical in both studies. Moreover, residue Asn-21, whose Cα chemical shift is 4 ppm less than those of the other asparagine residues, appeared in both studies at the same position in the spectra. The overlay shows that chemical shift differences between both studies did not arise from disagreements in sequential assignments. Indeed, for residues Leu-27 to Ser-34, cross-peaks appeared at different positions in the two spectra. This difference was very pronounced for serine residues, where three out of a total of five cross-peaks appeared at different positions (Ser-28, Ser-29 and Ser-34). From the partial mismatch of spectra, we conclude that we have studied a different polymorph of IAPP fibrils that showed significant chemical shift differences in the segment Leu-27 to Ser-34. These differences in chemical shifts might be a consequence of the difference in the C-terminus, which was amidated in the study of Luca et al. and occurred as a free acid in our study. They could, however, also reflect IAPP polymorphism independent of C-terminal (de)amidation and stem from alterations of the fibrillation pathway caused by subtle differences in the fibrillation conditions.

3.2.2 FGAILS-region forms a β-strand in IAPP$_{COOH}$

Structural characterization of the monomers in fibrils by chemical shift analysis led to the result that amino acid regions 8 to 20, 23 to 28, 30 to 32, and 35 to 36 form β-strands. Our data agree with previous models on the presence of a single β-strand in the N-terminal half of the peptide sequence (Figure 3.7), however with variations regarding its exact length and position [54, 33, 56, 55, 53]. More profound differences appear in the C-terminal half of the peptide. This

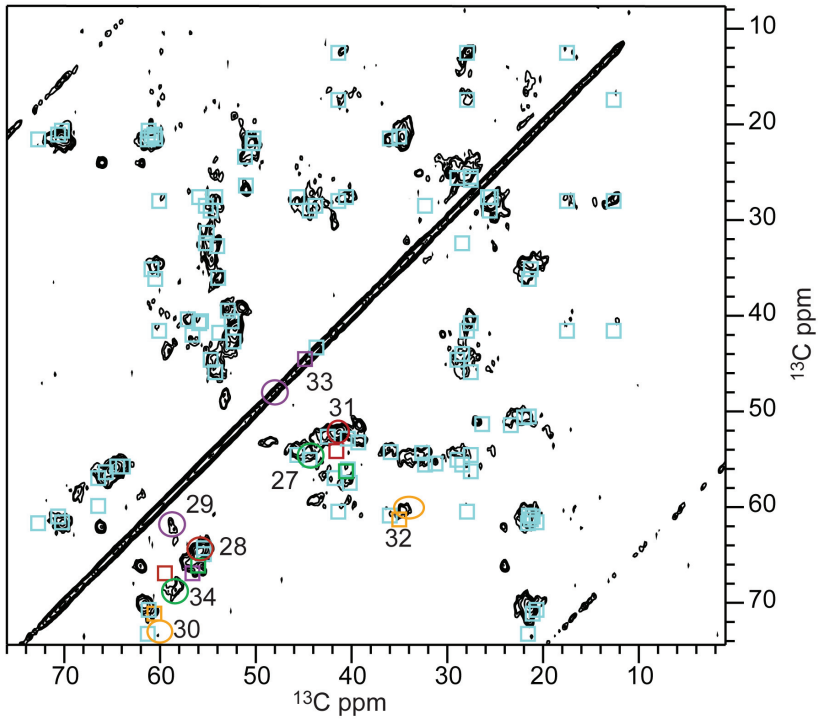

Figure 3.9: *Comparison with chemical shifts from former ssNMR study. Overlay of PDSD spectrum (black) with peaks generated from chemical shifts as published in 2007 by Luca et al. [33] (blue squares). A 2 ppm correction to the shifts reported by Luca et al. was made before comparison as different referencing compounds were used in both studies. Our spectrum was acquired at a field of 18.8 Tesla at 11 kHz MAS and a VT gas temperature of 0 ℃. The longitudinal mixing time was set to 20 ms. In the experiments from Luca et al., the N-term, except of A5, was not labelled. No systemic deviation in between the chemical shift values of the two studies is found, rather a partial agreement and partial disagreement between the peaks. Major differences in chemical shifts are observed for residues spanning region L27-S34. These are displayed in colors and marked with the respective residue number. Circles belong to our peaks and the colored boxes indicate the corresponding peaks from the study of Luca et al. (PLoS ONE 11(9): e0161243)*

half contains the region 23-FGAILS-28, which has been recognized early on to be of critical importance for IAPP amyloidogenicity [47, 117]. Our results from chemical shift analysis clearly indicate that the FGAILS region is part of a β-strand in our fibrils from hIAPP$_{COOH}$. This finding is in line with the crystal structure based model, which proposes a β-strand starting from Gly-24 [54], and with the serpentine model [53]. In contrast, other models suggest that this region may as well be part of a random coil loop [33, 56, 55].

In the hIAPP$_{COOH}$ fibrils, the conformation at position Ser-29 is less constrained than at other sites, and a continuous β-strand may be adopted spanning the region from Phe-23 to Val-32. A conformation in which these residues form a continuous β-strand is in reasonable agreement with the crystal structure based model [54] which predicts a β-strand for the GAILS segment. Taken together, the chemical shift analysis of our NMR data as well as our NHHC transfers strongly

support the hypothesis that the central segment FGAILS is able to adopt β-sheet conformation in mature IAPP$_{COOH}$ fibrils. The comparison with literature data indicates that this region, which is highly amyloidogenic, and critical for IAPP fibrillation, is the site of significant conformational variability in IAPP amyloid fibrils.

3.2.3 Structural aspects of the N-terminus in hIAPP

Considering their high peak intensities, their particular chemical shifts, and their enhanced T1ρ relaxation at weak spin-lock fields (ν_{rf}<10 kHz), the N-terminal amino acid residues Asn-3 to Thr-6 appear to have a more dynamic behavior than the β-strand regions, presumably due to a less dense packing. We assume free side chain rotations about the Cα-Cβ bonds and potential restricted puckering motions of the loop which lead to partial averaging of the backbone torsion angles. Inhomogeneous line-broadening due to different conformations might be reduced because of partial conformational averaging.

We underline the observation that the N-terminal residues showed the same conformation in two independently prepared samples. A further argument in favor of partial chemical shift averaging due to restricted conformational sampling is the finding that the Cα-Cβ cross peak of Ala-5 was broadened beyond detectability upon lyophilization [33], or upon freezing the sample to temperatures around 100 K (Figure 3.4).

3.3 Thioflavin-T fluorescence

To improve the fibrillation conditions for IAPP and gain knowledge on the production of more homogeneous fibril samples, its aggregation kinetics were studied in the presence of the fluorescence dye Thioflavin-T. Upon binding to β-structure, the fluorescence properties, i.e. frequency maximum and intensity, of ThT undergo an observable shift [118].
The effect of five different buffer conditions and increasing concentration of the β-wrapin HI18 on IAPP fibrillation were studied. The β-wrapin HI18 is expected to have an inhibitory effect on fibril formation [59] and the decreased aggregation rate is expected to cause more homogeneous fibrils. In all samples, the concentration of IAPP was 10 μM and the concentration of ThT was 40 μM. The concentration of the binding protein HI18 was increased from 0 μM to 20 μM. The fluorescence kinetics are shown in Figure 3.10. The fibrillation was studied first under intermittent agitation of the sample plate (A), and second without any agitation (B).
The orange graphs in A) show fibrillation in absence of the β-wrapin HI18. A sigmoidal curve with a lag time of circa 60 minutes is observed in all buffer conditions, except of MES buffer. In MES buffer, the lag-phase is increased from around 60 minutes to 150 minutes.
The green curves show the time course of IAPP fibrillation, when HI18 is added in a molar ratio of one. There is an inhibitory effect observed in NaPi 6, MES 6, and Tris 7.4. In these buffers, the lag-phase is prolonged in the presence of HI18. The inhibitory effect is not observed in NaPi 7.4 and HEPES 7.4 buffer.
The violet curves show the fibrillation kinetics of a molar ratio of 2:1 of HI18 to IAPP in the solution. This concentration of HI18 causes the strongest inhibitory effect, however not in NaPi 7.4. For NaPi 6, the lag-phase is increased by a factor of 4. For MES 6, again no typical sigmoidal curve is observed, but rather a very small linear rise in signal intensity. For Tris 7.4 and HEPES 7.4, an inhibitory effect is observed. The graphs show two plateaus, which could point to a secondary nucleation pathway.

As each point of the study was only acquired once, the standard deviation of the sampled values is high. The main conclusion of this fibrillation study is that the strongest inhibitory effect of HI18 is present in MES buffer at pH 6 and that IAPP is most stable in MES buffer. Therefore, this buffer was used for liquid-state NMR studies on soluble IAPP in the course of the project.

The agitation of the sample during the fibrillation might have had an effect on the kinetics. Shaking inhibits the sedimentation of fibrils and therefore exposes the fibrils to soluble monomers in the solution. Additionally, shaking increases the motion of the molecules in solution and increases the probability of molecules to collide. Therefore, the inhibitory effect of HI18 may be hampered by the sample agitation. The fibrillation kinetics without sample agitation and with lower buffer concentrations are shown in section B) of Figure 3.10. The blue curves show fibrillation in the absence of HI18 and the other curves show fibrillation in the presence of increasing amounts of HI18. Without agitation, the inhibitory effect of HI18 on fibrillation is strongly observed.
In section C) of Figure 3.10, the fibrillation kinetics of synthetic IAPP$_{NH_2}$ are shown. In synthetic

IAPP, the lag-phase prolongs upon addition of HI18, but the effect is less pronounced than in recombinant IAPP. The inhibitory effect is more pronounced for recombinant IAPP, than for synthetic IAPP.

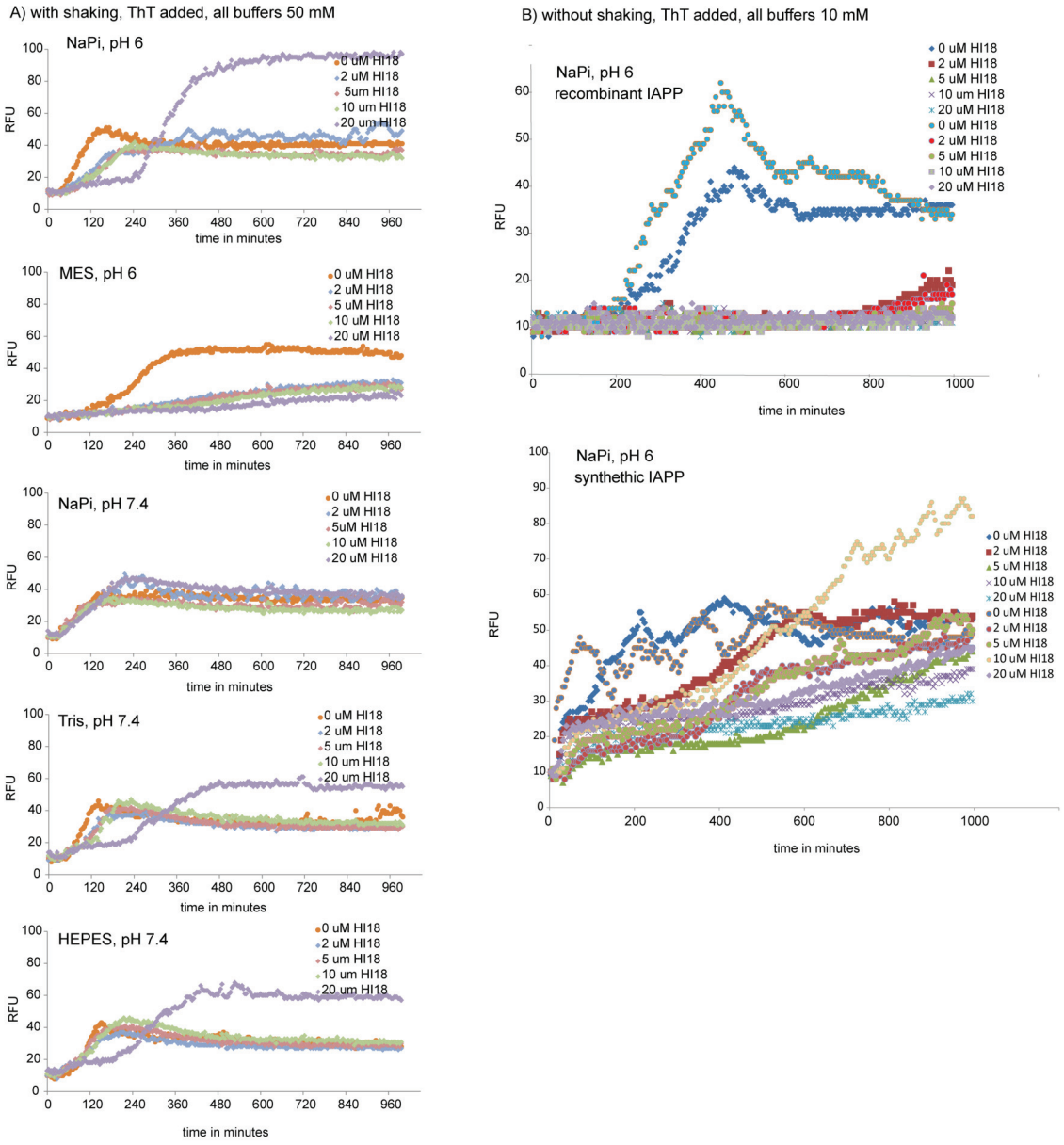

Figure 3.10: *Thioflavin-T fluorescence studies of IAPP in different buffers and with increasing concentration of the β-wrapin HI18. In A), shaking of the samples was applied, while in B), fibrils were grown under quiescent conditions. The buffer concentrations in A) were 50 mM and in B) 10 mM.*

3.4 Microscopic studies

3.4.1 Atomic force microscopy

The samples of the above mentioned ThT fluorescence study were also studied by atomic force microscopy.

In Figure 3.11, fibrils grown under quiescent conditions and without the addition of HI18 are shown. There are big differences visible in between fibrils formed from recombinant or synthetic IAPP. For recombinant IAPP, short, thick fibrils are observed, which build bigger assemblies. For synthetic IAPP, very thin fibrils are observed in combination with huge aggregates. These aggregates might be of proteinaceous origin or stem from phosphate crystals in the buffer. In sample 8 A), ThT was added to the fibrillation solution. In this sample, drop-like species are observed. These drops are observed in many AFM micrographs and seem to appear prior to fibril formation. The droplets measure around 10 to 100 nm in height. They appear like droplets of high peptide concentration, phase separated from the environment, i.e. like the 2D projection of a colloidal suspension. Droplet-like species are often described as precursors to fibril formation. These localized high concentrations of aggregation prone peptide might still contain soluble molecules, while some environmental impact might cause the stable suspension to fibrillize [119].

In Figure 3.12, fibrils are shown that were grown in the presence of HI18 in a molar ratio of 1:1. Additionally, ThT was present in this samples in a molar ratio of 4:1 (ThT:IAPP). The fibrils grown in the presence of HI18 do not show notable morphological differences.

From the AFM pictures alone, it is not possible to completely judge the homogeneity of the fibrils. Conclusions that can be drawn are that fibrils in the AFM micrographs show no observable twist around their long axis and that thinner fibrils (protofilaments) appear to assemble into higher order filaments (mature fibrils). The thin filaments observed have a height around 4 nm, and the bigger filaments up to 50 nm.

3.4.2 Electron microscopy

Electron microscopy on uranylacetate-stained IAPP fibrils was done with the aim to judge if the sample is eligible for a cryo-EM study. The EM measurements were done by Prof. Dr. Gunnar Schröder. Two micrographs are shown in Figure 3.13. Fibrils appear very similar to the AFM pictures, but they do assemble stronger into bundles. This might be due to different surface conditions of the grid as compared to the Mica. The assembly of the fibrils is mainly laterally. Again, thicker fibrils appear to be made up of thinner rods. It is not distinguishable, if the thinner rods twist around each other or simply attach laterally. Drop-like species were not observed in the EM experiments.

As the fibrils form large assemblies, it was not possible to pick single fibrils for a more intense EM examination and the fibrillar sample was found to be not amenable for a further cryo-EM study.

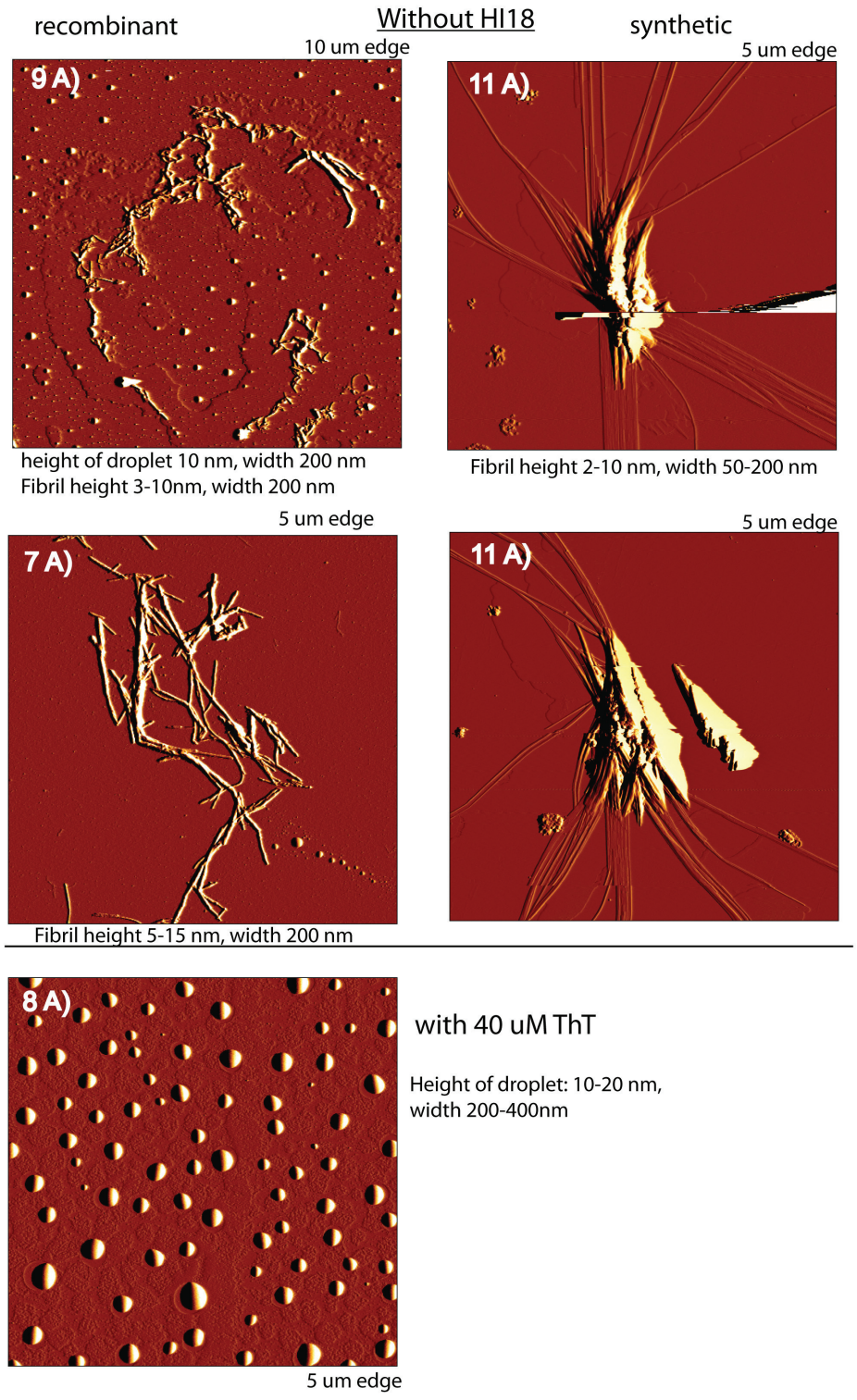

Figure 3.11: *Atomic force micrographs of IAPP fibrils, grown without addition of HI18 in 10 mM NaPi, pH 6 under quiescent conditions.*

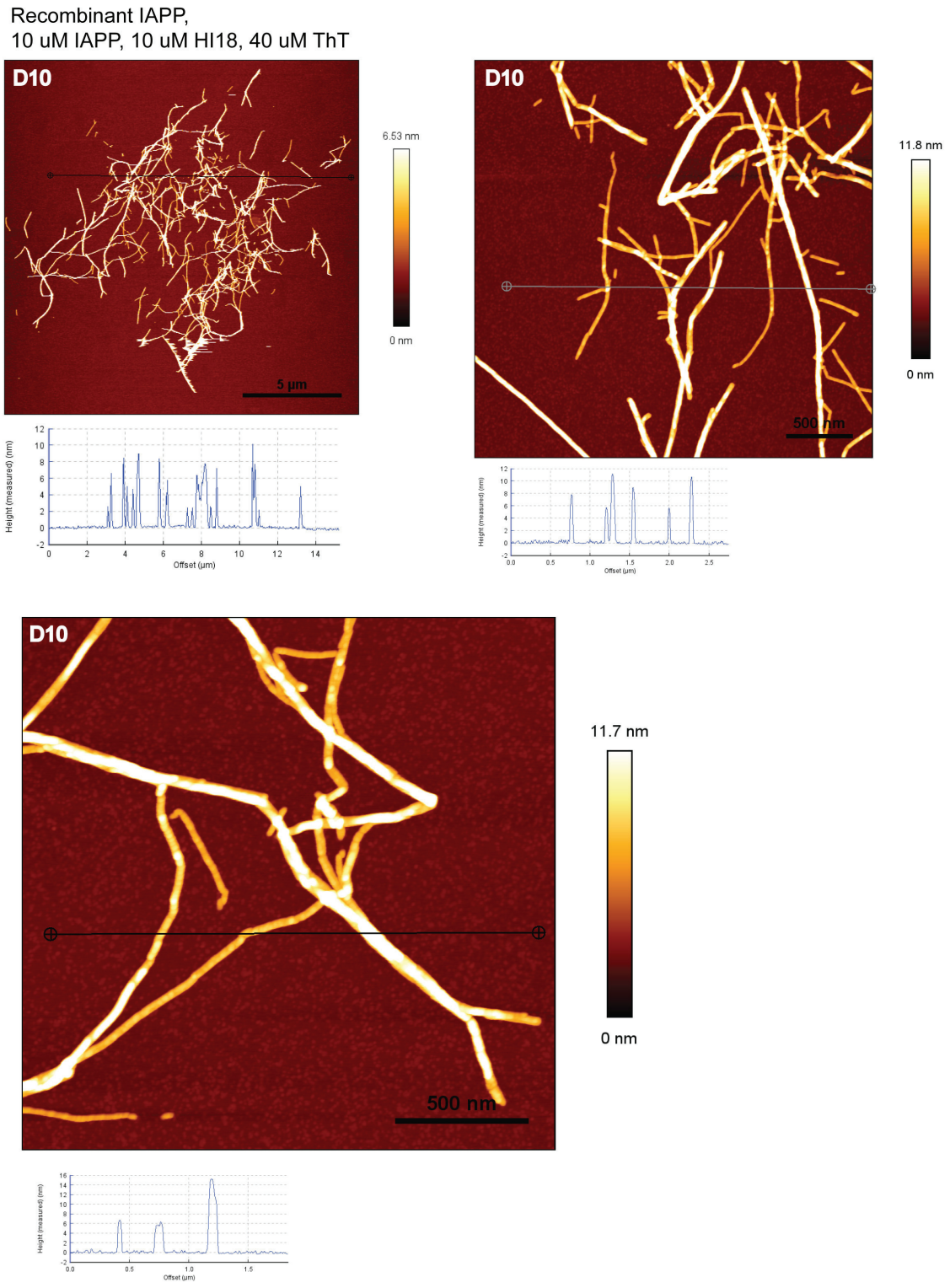

Figure 3.12: *Atomic force micrographs of IAPP fibrils, grown with addition of HI18 and ThT in 10 mM NaPi, pH 6 under quiescent conditions.*

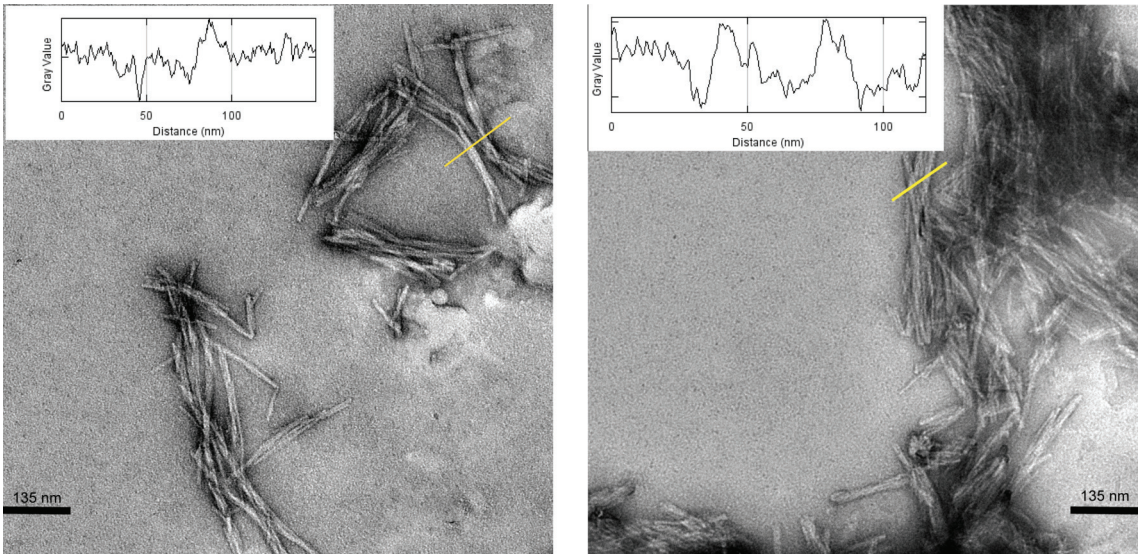

Figure 3.13: *Electron micrographs of IAPP fibrils stained with uranyl acetate. The area of one image is (1085 nm)^2. Shown are fibrils found at two different regions on the same grid. Fibrils look comparable in the two regions observed. The cross-sections correspond to the yellow lines.*

3.5 Selectively and extensively labelled IAPP$_{COOH}$

After evaluating the uniformly ^{13}C, ^{15}N labelled sample and the diluted sample (1:4) for site-specific resonance assignment, the TEASE labelling approach (Ten amino acid selective and extensive labelling) was applied to recombinantly produce two more samples [95]. The first sample was produced by using 1-^{13}C glucose as sole carbon source and the second one using 2-^{13}C glucose as sole carbon source in the M9 medium (see Figure 2.3). The usage of the specifically labelled glucose as carbon source results in a diluted distribution of ^{13}C spin labels in the samples. Furthermore, the TEASE approach includes the addition of ten unlabelled amino acids to the expression medium. These are Asn, Asp, Arg, Gln, Glu, Ile, Lys, Met, Pro, and Thr. They are added to the expression medium in unlabelled form, to suppress a labelling of their spin systems. The labelling strategy is supposed to yield a labelling pattern as shown in Figure 3.19.
In the TEASE labelling approach, the amino acids produced in the glycolytic pathway are labelled and the amino acids produced in the citric-acid cycle are unlabelled. The glycolytic pathway includes the formation of two three-carbon molecules from one glucose molecule [120]. Therefore, an amino acid from the glycolytic pathway is labelled at one position with a probability of 50 $\%$ and at two positions with a probability of 25 $\%$.

Expression yield Both samples were prepared from 800 ml M9 medium.
The eluted fractions of the final RP-HPLC purification step were 377 ml for the first and 268 ml for the second sample, with concentrations of 120 μM and 95 μM, respectively. The peptide yielded was calculated as 4.8 mg for the first, and 3.8 mg for the second sample.

3.6 NMR studies on selectively and extensively labelled IAPP

3.6.1 Liquid-state NMR experiments

Liquid-state NMR experiments were performed with the help of Dr. Rudolf Hartmann.
To verify the expected labelling scheme, liquid-state NMR experiments were performed on the selectively and extensively (TEASE) labelled samples and on an uniformly labelled sample as reference. The ^{15}N-HSQC spectrum of soluble uniformly labelled IAPP was compared to existing literature, and the chemical shifts are completely matching [97, 59, 98]. Figure 3.14 shows the assigned ^{15}N-HSQC and ^{13}C-HSQC spectra of soluble, uniformly labelled IAPP at pH=6.0 in 50 mM MES buffer. Under these buffer conditions, IAPP stays soluble for several hours, which allows to perform the mentioned liquid-state NMR experiments. The assignment was done by evaluating a 3D HNCαCβ experiment and a 3D HNcoCαCβ experiment. Not all side-chain cross-peaks could be assigned in the ^{13}C-HSQC spectrum with this approach. The sequential assignment is shown in strip-plots in Figures 3.15 and 3.16.

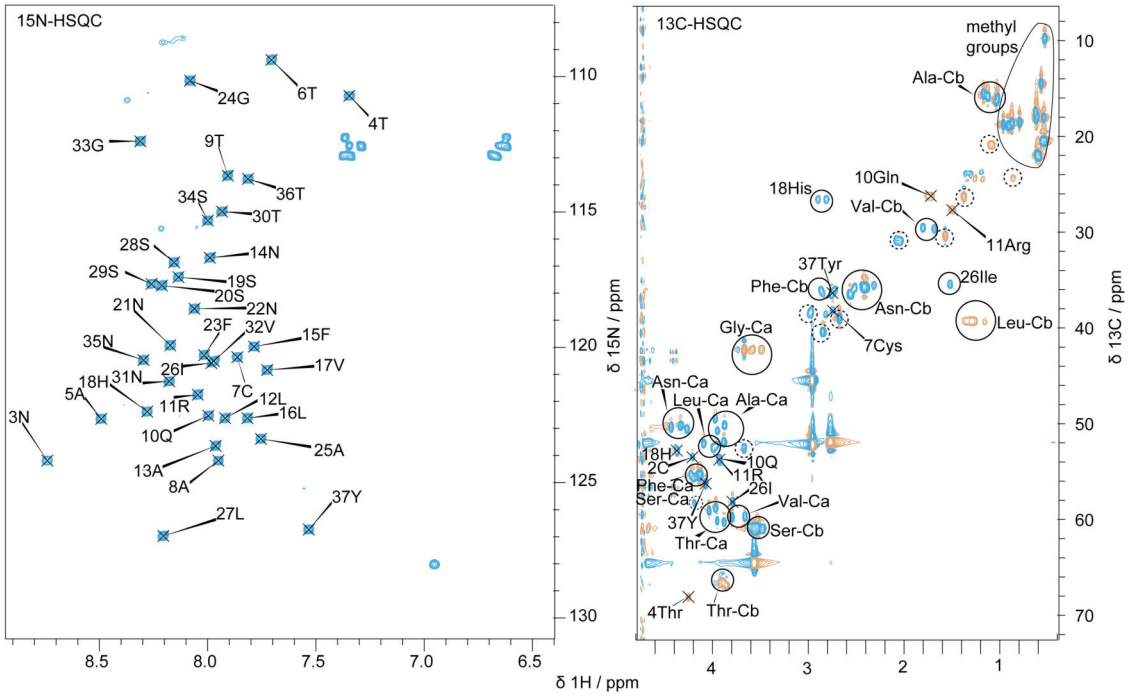

Figure 3.14: *HSQC spectra of uniformly labelled IAPP in 50 mM MES, pH=6, T=5 ℃. A) shows the ^{15}N-HSQC spectrum and B) the ^{13}C-HSQC spectrum. The assignment was obtained by evaluation of a 3D HNCαCβ and a 3D HNcoCαCβ spectrum.*

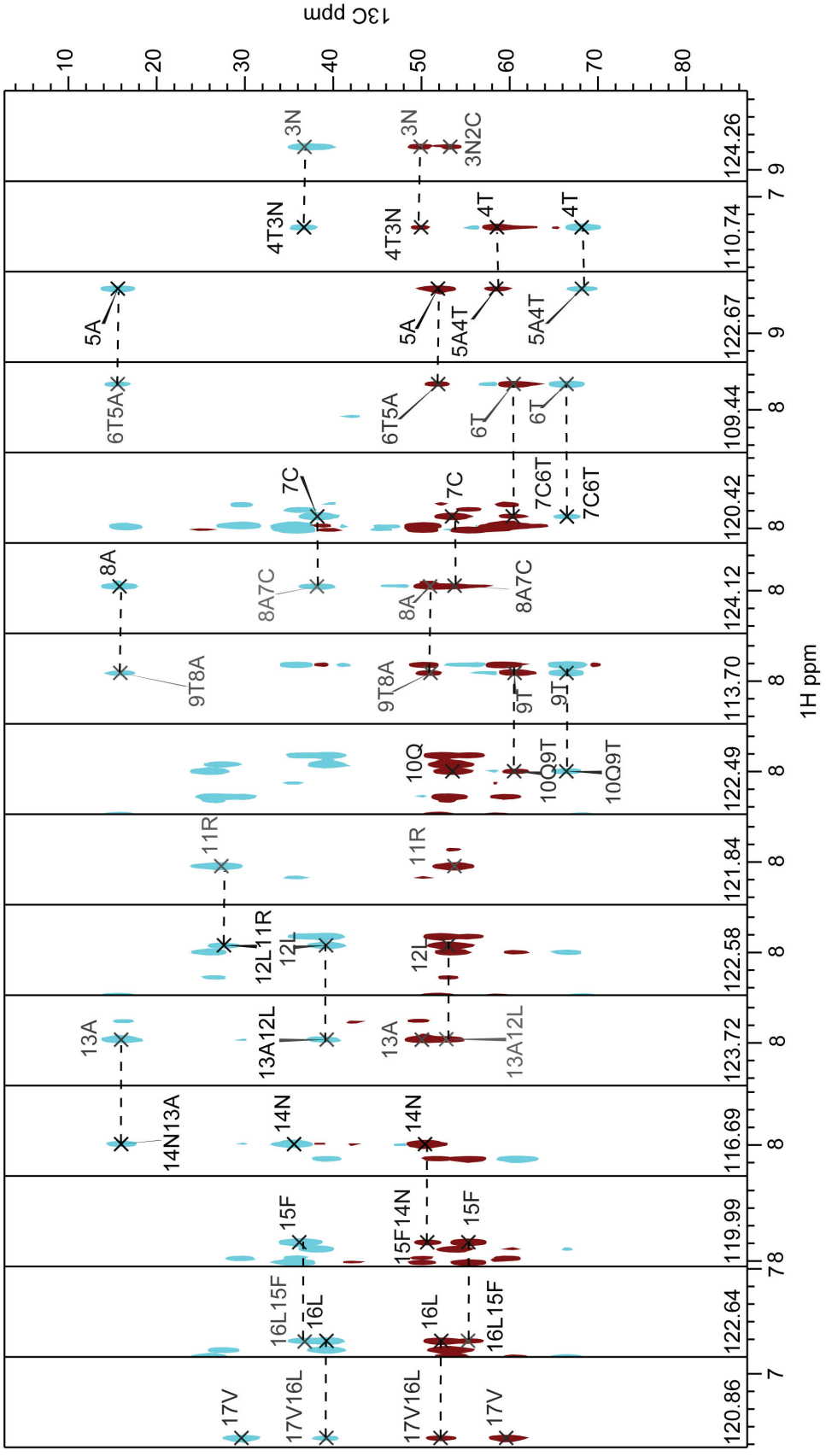

Figure 3.15: *Sequential assignment of soluble IAPP shown by strip-plots of the 3D HNCαCβ spectrum.*

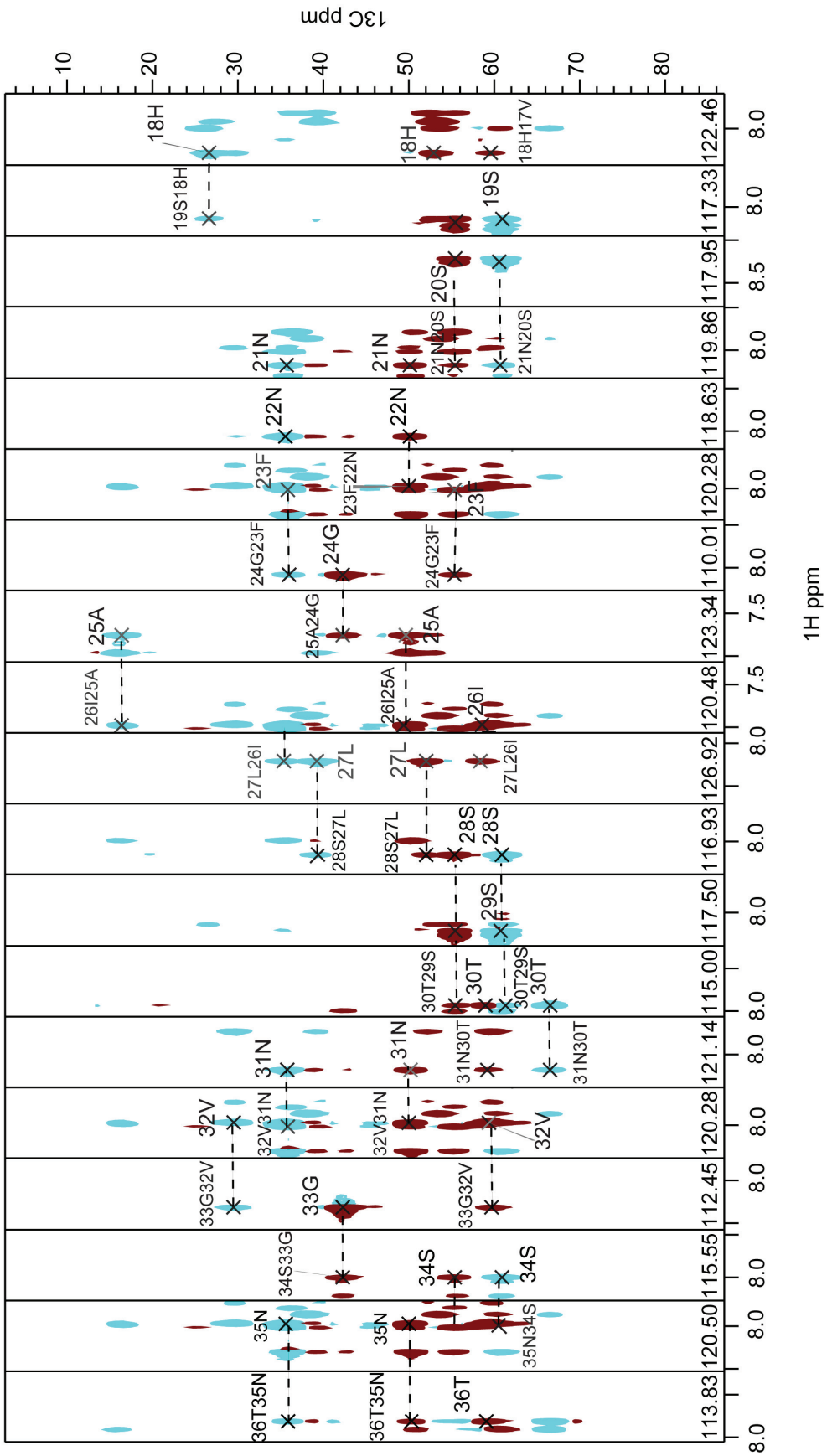

Figure 3.16: *Sequential assignment of soluble IAPP shown by strip-plots of the 3D HNCαCβ spectrum.*

1-^{13}C labelled sample Figure 3.17 shows the overlay of the 1-^{13}C glucose labelled sample with the uniformly labelled sample. It is observed, that the cross-peaks in the ^{15}N-HSQC spectrum match well the uniformly labelled reference spectrum. The first labelling scheme mainly produces labels at Cβ-sites, at methyl-groups, and at carbonyl sites. Furthermore, the Cα-nuclei of the leucine residues are expected to be labelled. Evaluating the ^{13}C-HSQC in Figure 3.17, it can be observed, that the leucine Cα sites are labelled, and a slight scrambling also caused a weak labelling at Asn, Gly, and Gln/Arg Cα positions. No further labelled Cα nuclei are observed. As expected, labels are observed at resonances typical for Ser, Tyr, Cys, Phe, and Ala Cβ positions, while Leu, Ile, Gln, Val, and Thr do not show labels at Cβ positions. From this analysis of the liquid-state NMR spectra, it is deduced, that the labeling has worked well for the first sample and that only weak scrambling effects are observed.

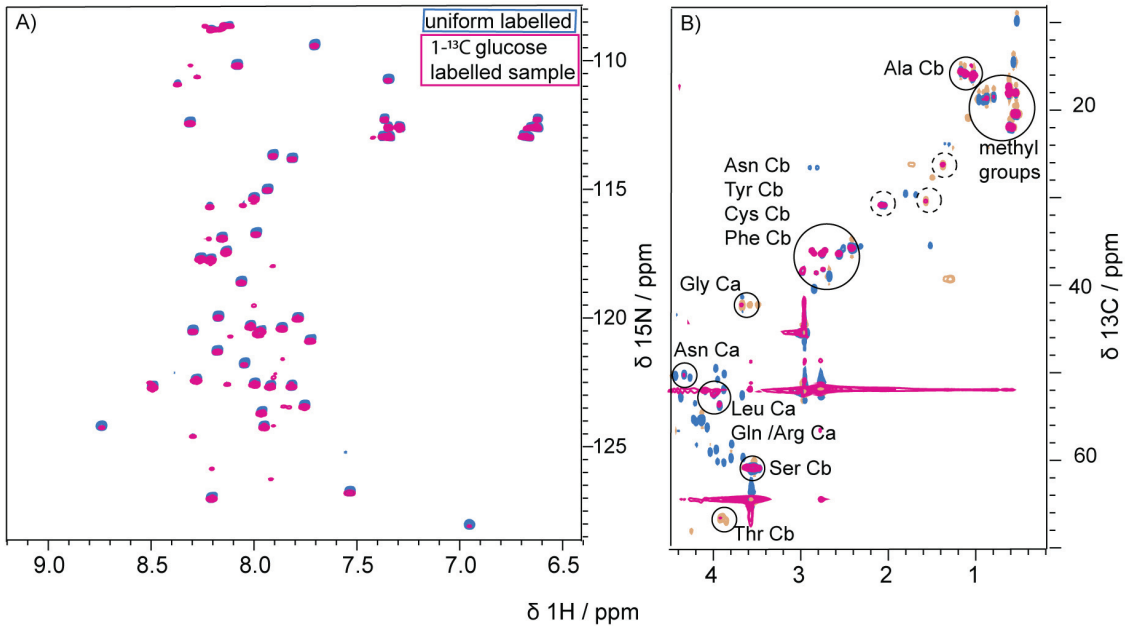

Figure 3.17: *Overlay of ^{15}N-HSQC and ^{13}C-HSQC spectra of uniformly and 1-^{13}C labelled IAPP in 50 mM MES, pH=6, T=5 ℃. The dashed circles indicate resonances which could not be assigned.*

2-^{13}C labelled sample The ^{15}N- and ^{13}C-HSQC spectra of the 2-^{13}C labelled sample are shown in Figure 3.18. The ^{15}N-HSQC spectrum shows many cross-peaks that are not matching the reference spectrum, and expected resonances are missing. The cross-peaks seem to arise from impurities, as they are also visible in the uniformly labelled sample and the 1-^{13}C labelled sample, but at much lower contour levels. In this sample, the impurities appear very pronounced. From these spectra alone, the success of the TEASE labelling strategy cannot be judged.

In the solid-state NMR spectra, as shown below, the sample showed cross-peaks at the expected sites. Therefore, the concentration of the sample for the liquid-state NMR study was too low for detection. The solid-state NMR spectra show indeed that fibrillation worked well and that the labelling strategy yielded the expected results.

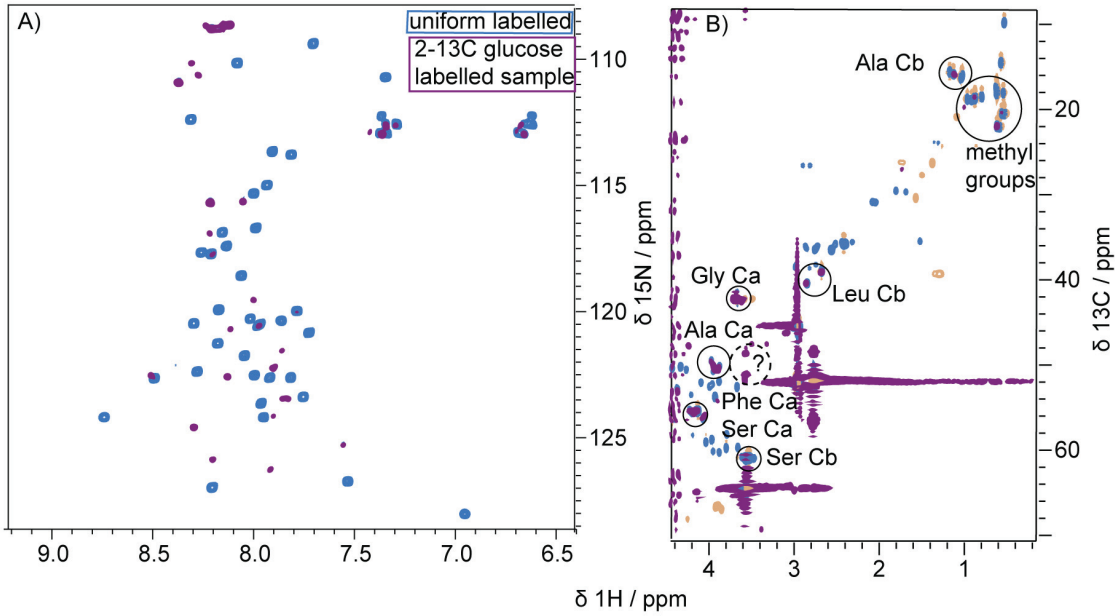

Figure 3.18: *Overlay of ^{15}N-HSQC and ^{13}C-HSQC spectra of uniformly and 2-^{13}C labelled IAPP in 50 mM MES, pH=6, T=5 °C. The dashed circles indicate resonances which could not be assigned.*

3.6.2 Solid-state NMR experiments

The selectively and extensively labelled samples were fibrillated, pelletized and centrifuged into sample rotors, as described in the Materials section. The experiments performed on the two samples and the applied processing functions are listed in Table 3.1. Initially, 1D experiments with

Spectrometer	1,^{13}C	2,^{13}C	Processing
600 MHz, Oxford	PDSD, 750 ms, 2528 scans		EM 120 Hz
	PDSD, 500 ms, 3616 scans		EM 120 Hz
		PDSD, 750 ms, 1216 scans	EM 120 Hz
600 MHz, Varian	PDSD, 50 ms, 272 scans		EM 120 Hz
800 MHz, Varian		PDSD, 80 ms, 464 scans	EM 100 Hz
		PDSD, 800 ms, 1072 scans	EM 100 Hz

Table 3.1: *Solid-state NMR experiments on selectively and extensively labelled samples. All experiments were performed at 0 ℃ VT gas temperature and 11 kHz MAS.*

detection on ^{13}C nuclei were performed and compared to spectra from the uniformly labelled sample. The number of scans acquired for the 1D spectra was 16 times more than on the uniformly labelled sample. The spectra are shown in section A) of Figures 3.19 and 3.20. The factor of 16 in acquisition time still yields a decreased signal-to-noise ratio compared to the uniformly labelled sample. The lower signal intensity can be explained by the probability of only 50 $\%$ of a labelled spin in a residue, due to the glycolytic pathway, as explained above. The probability to find two labelled ^{13}C spins in one residue is only 25 $\%$.

Subsequently, a short mixing time PDSD spectrum (50 to 80 ms) was acquired on each sample to observe, if any intra-residual peaks appear and to judge if the labelling scheme meets the expectations. Also the occurrence of scrambling, i.e. the metabolism of labelled amino acids in *E.coli*, is evaluated. Spectra are shown in section B) in Figures 3.19 and 3.20. In the 1st sample, an asparagine Cα-Cβ peak was observed, as well as some Cα-Cβ signals in the serine and threonine region. This matches the observations made in the liquid-state NMR spectra. No further unexpected intra-residual peaks were observed.

In the 2nd sample, as expected, a Cα-Cβ cross-peak for valine and a Cβ-Cγ cross-peak for leucine were observed in a short mixing time PDSD spectrum (Fig. 3.20). There are no unexpected resonances observed, as was indicated by the liquid-state NMR spectra. The 80 ms PDSD spectrum of the second sample shows that the labelling scheme has indeed worked well.

On these two samples, mainly long mixing-time PDSD experiments were performed, because the primary aim was to find medium, and long-range contacts of residues separated by more than two positions in the sequence (|k-l|>2) for a structure calculation. Long-range intra- and intermolecular contacts were expected to show up in PDSD spectra with mixing times > 500 ms. A through-space magnetization transfer of up to 7 Å was supposed to be possible with 500 to 800 ms mixing time [11, 14]. The spectra are shown in section C) of Figures 3.19 and 3.20. Due

to the low signal-to-noise ratio of the spectra, a high number of transients per experiment and a very conservative processing with up to 120 Hz line-broadening were required (see Table 3.1). In these spectra, it was hard to unequivocally judge a peak from a noise signal. Additionally, cross-peaks were not observed in several complementary spectra at the same positions. As a result, no intra-molecular cross-peaks were successfully selected for a structure calculation from these spectra.

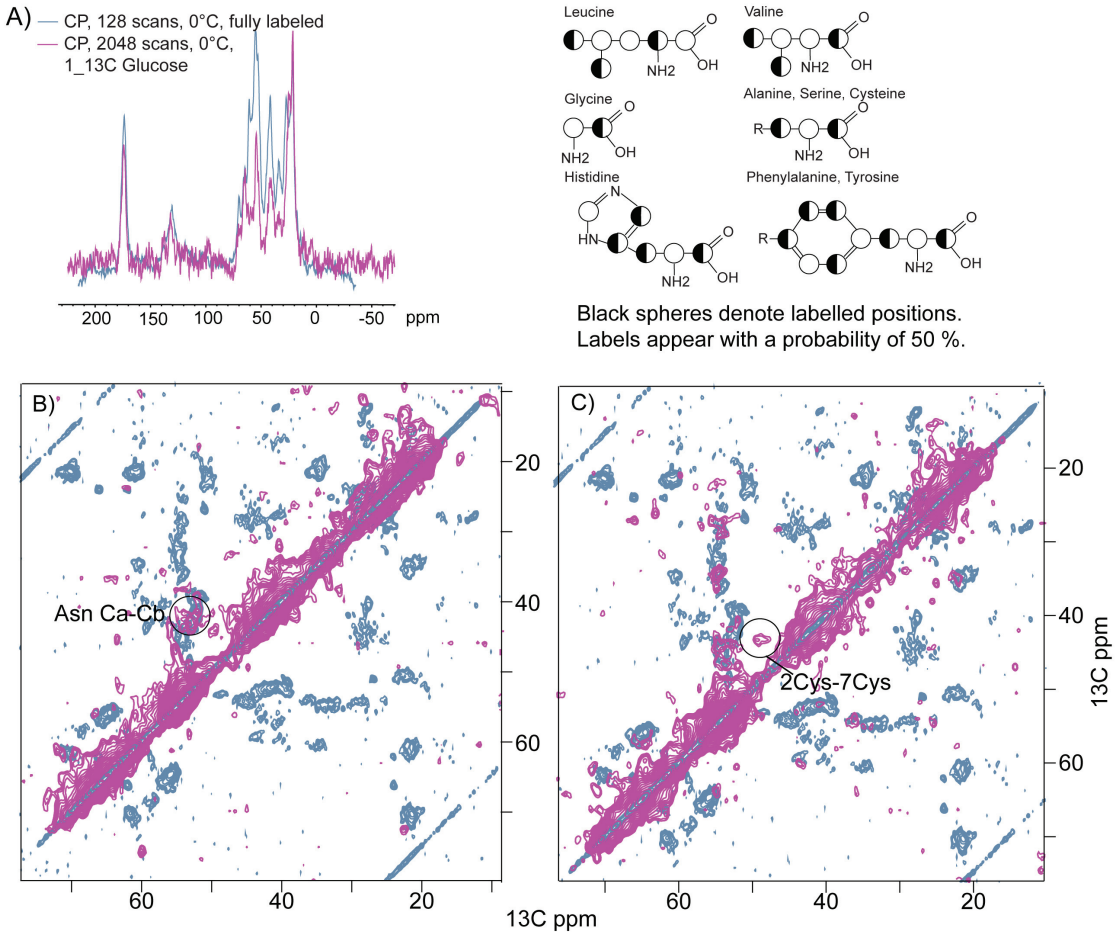

Figure 3.19: *Solid-state NMR spectra of 1-^{13}C glucose labelled IAPP, compared to a fully labelled reference spectrum. In A), 1D ^{1}H-^{13}C CP experiments are shown. In B) and C), PDSD spectra of uniformly (blue, 20ms) and 1-^{13}C (pink) labelled IAPP are shown. The mixing times of the experiments on the diluted sample were 50 ms (B) and 750 ms (C).*

DNP experiment on 1-^{13}C labelled IAPP Due to the low signal-to-noise ratio observed in the spectra, also a DNP sample was prepared from 1-^{13}C labelled IAPP fibrils. With dynamic nuclear polarization, the polarization of electrons is transferred to the ^{1}H nuclei by microwave irradiation and an enhancement of signal intensity is observed [92]. A 1D spectrum of a ^{13}C-^{13}C cross-polarization experiment at 120 K under microwave irradiation is shown in section A) of Figure 3.21. The two very intense signals arise from the d_8-glycerol, which is added as cryo-protectant

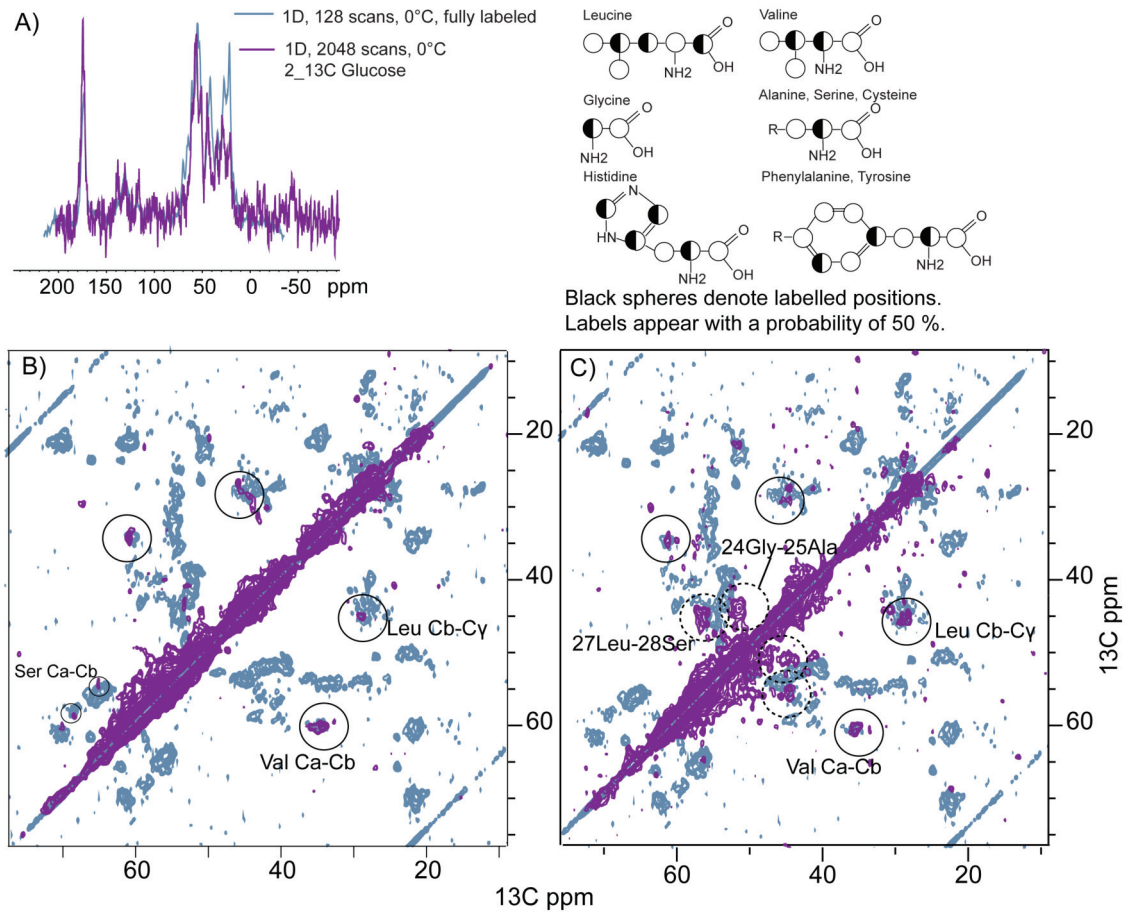

Figure 3.20: *Solid-state NMR spectra of 2-^{13}C glucose labelled IAPP, compared to a fully labelled reference spectrum. In A), 1D ^{1}H-^{13}C CP experiments are shown. In B) and C), PDSD spectra of uniformly (blue, 20ms) and 1-^{13}C (purple) labelled IAPP are shown. The mixing times of the experiments on the diluted sample were 80 ms (B) and 800 ms (C).*

to the sample. The spectrum was acquired with 64 scans, which is a high number of transients for a 1D DNP experiment. Yet, the signal intensity is very low.

In section B) of Figure 3.21, a PDSD spectrum with a longitudinal ^{13}C-^{13}C mixing time of 5 seconds is shown. The spectrum was acquired with 256x140 scans. Also in the 2D experiment, the glycerol peak was observed, overlaying with possible signals from serine and threonine residues. Cross-peaks from the fibril sample can be observed in aliphatic, aromatic and carbonyl regions. The one strong signal in the aromatic region can be assigned to an intra-residual 23-Phe Cβ-Cδ_1 cross-peak.

In this sample, the Cα nuclei of the three leucine residues are labelled. It is indicated with a line, that these nuclei show correlations to other nuclei. Due to the low temperature, the resolution of the spectrum is decreased and does not allow to unambiguously assign these cross-peaks [121].

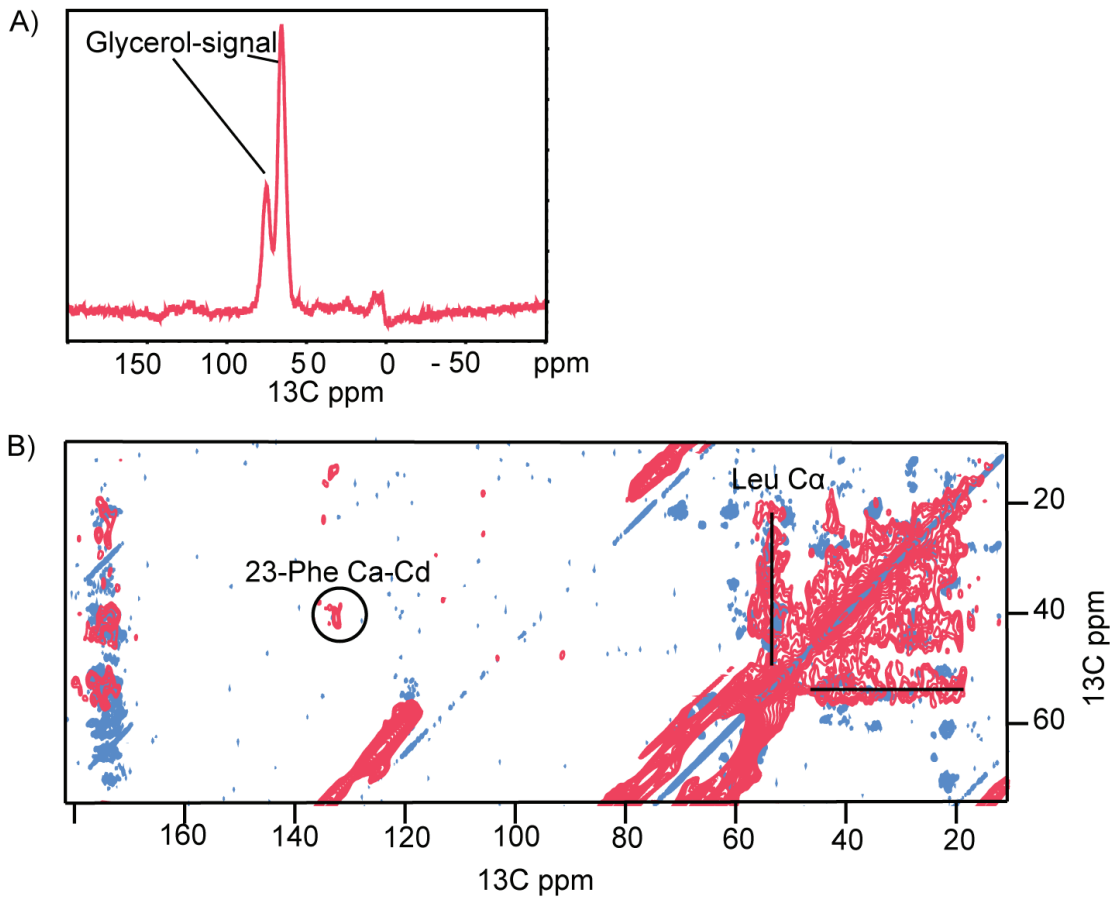

Figure 3.21: *DNP spectra of fibrillar 1-^{13}C glucose labelled IAPP. In A), a 1D ^{13}C experiment acquired with 64 scans is shown. In B), a PDSD spectrum with 5 seconds mixing time acquired at 120 K (pink), on top of a 20 ms mixing time conventional PDSD spectrum (blue) is shown. The Leucine Cα nuclei are labelled in this scheme, and their correlations to other nuclei are visible.*

Long-range contacts in selectively and extensively labelled samples In the long mixing time PDSD spectra of the two selectively and extensively labelled samples, no reproducible and evaluable inter-residual contacts were observed which could be used as unambiguous constraints for a structure calculation. The aim of a structural elucidation of fibrillar IAPP was therefore pursued by further examination of the uniformly labelled and the diluted sample.

3.7 Structural information from NMR experiments

The calculation of a structure based on NMR restraints is a complex topic and different computer programs have been developed [122]. The program CYANA is based on simulated annealing driven by molecular dynamics simulation. The simulated annealing approach first heats up the protein to induce a high kinetic energy and slowly cools it down. The danger of being trapped in a local minimum instead of a global minimum is reduced by this method. The user provides experimental constraints, as dihedral angles and distance information, or even unassigned peak lists. The software sets-up a target function that contains the experimental parameters, as well as known parameters, as bond-lengths, bond angles, and chiralities. If all constraints are fulfilled by a structure, the target function approaches a minimum. The target function represents a free energy and the aim is to find its global minimum, which corresponds to the protein structure that best fits the experimental data.

A crucial point in a structure calculation is the presence of a sufficient number of distance restraints. A recent solid-state NMR based Aβ structure applied 18 distance restraints per restrained residue [15]. The intra-molecular or inter-molecular origin of a cross-peak can be distinguished by comparing the spectra of uniformly labelled samples with spectra of diluted labelled samples. Restraints for a structure calculation can be of sequential, short- or long-distance type.

The determination of a protein structure by NMR is an iterative process. Based on secondary structure information, the observation of differing peak intensities of Cα-Cβ cross-peaks, and tertiary contacts, preliminary structural models can be generated. These provide a starting point for further refinement, for example by searching spectra for validating cross-peaks and by producing and examining samples with specifically labelled sites.

3.7.1 Secondary structure

The backbone ^{13}C chemical shifts obtained from site-specific resonance assignment provide information on positions of secondary structure elements due to their systematic deviation from random-coil values [74, 78]. The secondary structure analysis of IAPP fibrils by calculation of differences of secondary chemical shifts, and an analysis by TALOS-N has provided three β-strands at positions (8-20), (23-32), and (35,36). The difference of Cα and Cβ secondary chemical shifts was calculated with BMRB values for the publication in 2016 [19]. As there are additional resources to obtain random-coil values [75, 76, 77], the difference of secondary chemical shifts was calculated again, also applying the different random-coil values. The random-coil chemical shifts are found in the Materials section on page 40 and 39. The results are shown in Figure 3.22.
It is observed, that despite the small differences in the random-coil values, the location of β-structure elements remains the same.
Complementary to the information obtained from the chemical shift values, the cross-peak intensities in short mixing time PDSD spectra contain information on the order or disorder of regions.

Strong and intense peaks in ^{1}H-^{13}C CP-based experiments indicate a well-ordered conformation, while scattered or less intense peaks might point to a conformational disorder. In a 20 ms PDSD spectrum (Figure 3.1 on page 45), it is observed that Cα-Cβ cross-peaks at positions Leu-16, Val-17, Ile-26, Ser-29, and Thr-30 are less intense. Residue Thr-30 is not well observed in the 20 ms PDSD spectrum, and best observed in a DREAM spectrum, as shown in Figure 3.6 on page 53. Due to the weak peak intensity, a less constrained conformation at these positions is assumed, i.e. there might be conformational scattering, or these residues might build a loop that is less constrained than the β-strands. This information is considered in one of the three structural models proposed below.

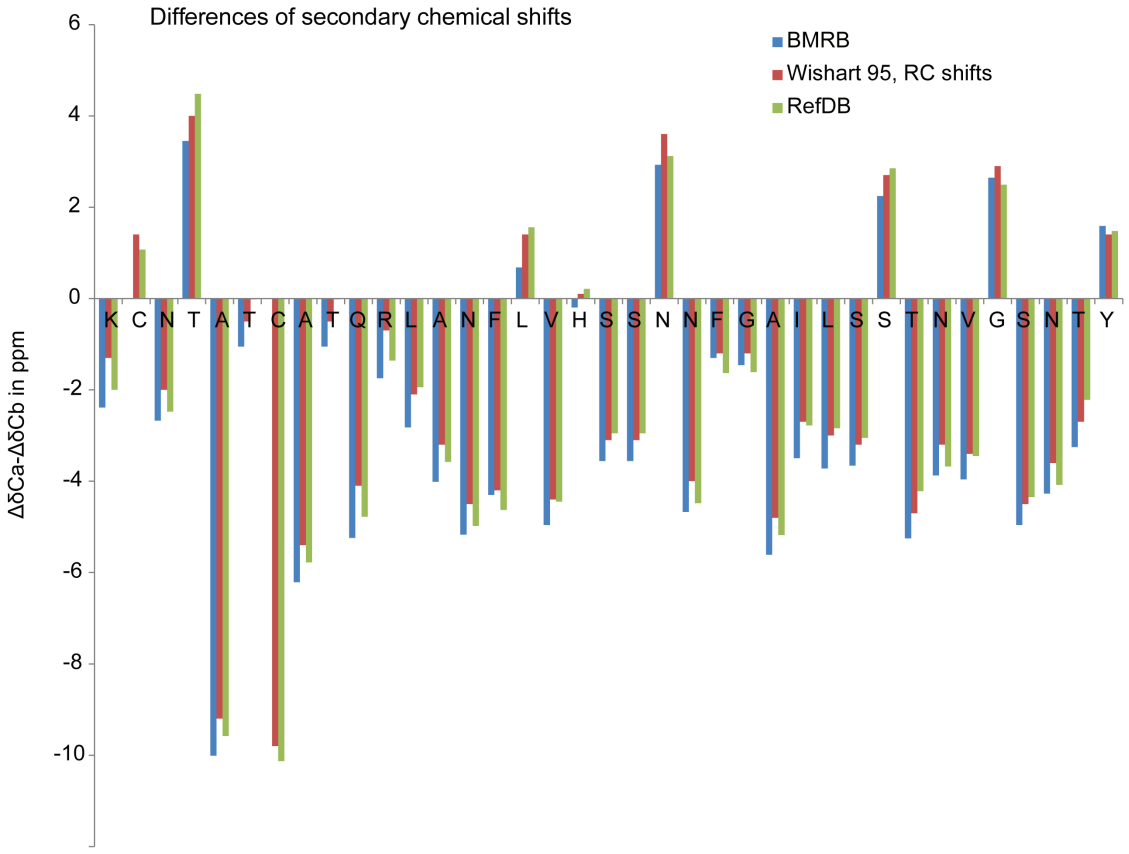

Figure 3.22: *Difference of Cα and Cβ secondary chemical shifts calculated with random-coil values from three different resources.*

3.7.2 Ambiguous through-space contacts

Due to the relative orientation of secondary structural elements, contacts between residues in adjacent β-strands can emerge, which contain information on the tertiary structure of the protein. Long mixing time PDSD spectra were searched for such through-space contacts of nuclei which are close in space. First, long mixing-time PDSD experiments were performed on the two selectively and extensively labelled samples, as described above. Due to their low signal-to-noise ratio, no reliable distance restraints were gained from these experiments within a reasonable measurement time.
Therefore, the uniformly and the diluted (1:4) sample were examined further, also applying long mixing time PDSD spectra. It has been demonstrated in earlier ssNMR studies that structural information can be extracted from the combination of experiments on uniformly labelled and diluted samples [11, 14, 15]. The difficulty with this approach is that spectra are more crowded and observed signals show a higher level of ambiguity due to spectral overlap, as compared to sparsely or specifically labelled samples.

Intra-molecular contacts Initially, the diluted sample was examined in PDSD experiments with 500 ms and 800 ms mixing time. The diluted sample was prepared by mixing one part of labelled IAPP with four parts of unlabelled IAPP prior to fibrillation. Therefore, 20 $\%$ of the molecules in the fibril are labelled. The probability of a labelled molecule to have no labelled molecule as a neighbour is $0.8^2 = 0.64$. The probability of a labelled molecule to have a labelled neighbour on either site is $2 \cdot 0.2 \cdot 0.8 = 0.32$, and the probability of a molecule to have two labelled neighbouring molecules is $0.2^2 = 0.04$. Therefore, in this sample an inter-molecular cross-peak has an intensity which is reduced to circa 36 $\%$ as compared to a fully labelled sample.
A maximum distance of 7 Å in between the observed nuclei is assumed. The spectra are shown in section A) of Figure 3.23. From the high number of peaks observed in these spectra, four cross-peaks were selected as evaluable, because of their separated position. Additionally, they do not show up in PDSD spectra of mixing times < 200 ms and are not of sequential origin. The ambiguous cross-peaks are listed in Table 3.2. From these four cross-peaks, ambiguous intra-molecular distance restraints were created and used in a first structure calculation with the simulated annealing program Cyana, as described below.

Inter-molecular contacts In section B) of Figure 3.23, an 800 ms PDSD of the uniformly labelled sample is shown. One new cross-peak shows up, which is not observed in spectra of the diluted sample. Therefore, this cross-peak might be of inter-molecular origin. Its ambiguous assignment is shown in Table 3.2. This cross-peak provides an ambiguous distance constraint for the calculation of a multimer. Fibril structures are often based on symmetric subunits, i.e. two or three symmetric molecules in one fibril layer [123]. Inter-molecular contacts serve to define the interface in between these subunits.

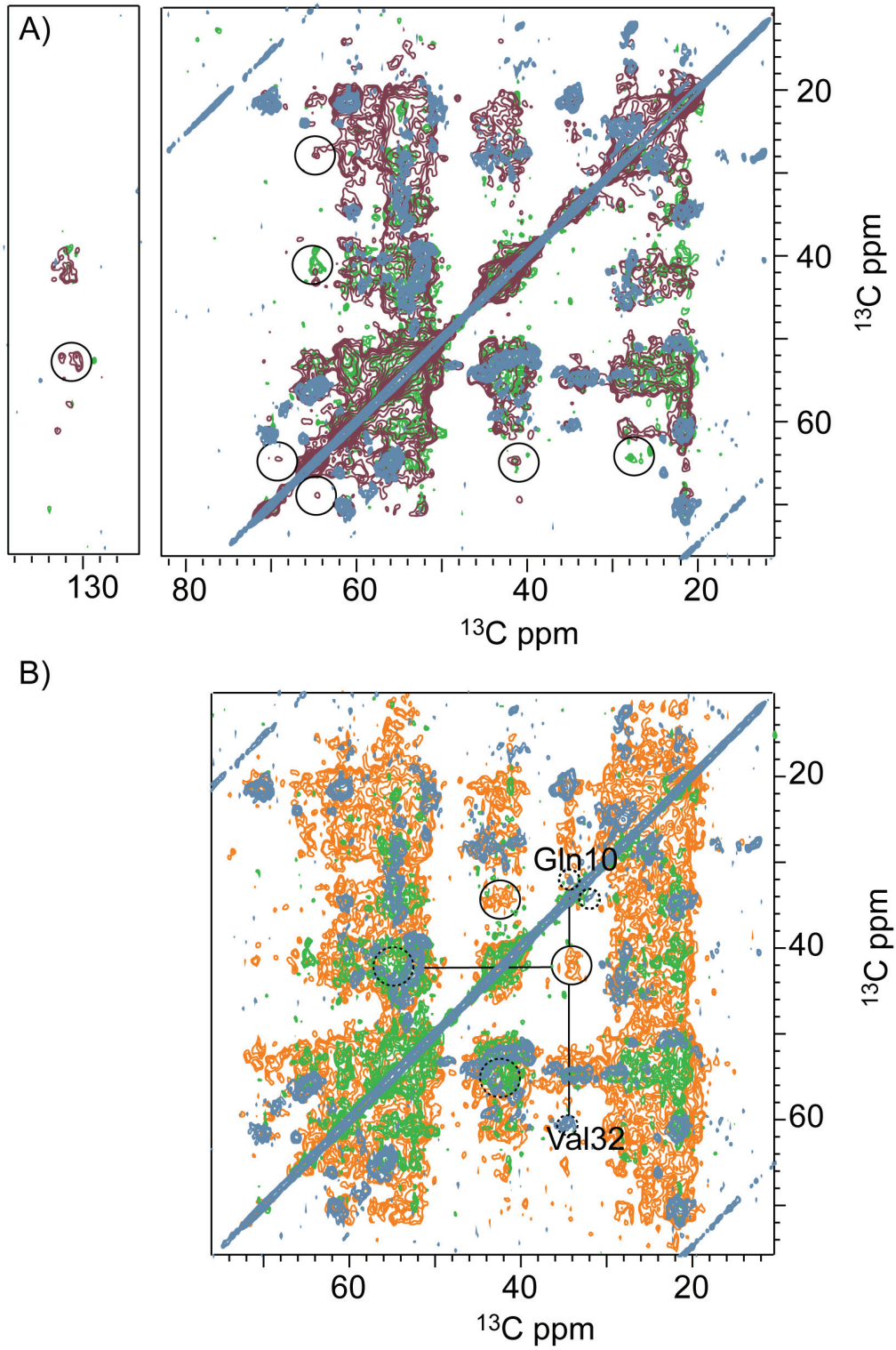

Figure 3.23: *A) Shown are long-mixing time PDSD spectra of the diluted (500 ms red, 800 ms green) sample. The blue spectrum is a 20 ms PDSD reference spectrum acquired on the uniformly labelled sample. B) Long-mixing time PDSD spectrum of the diluted (800 ms green) sample and of the uniformly labelled sample (800 ms, orange). A new cross-peak appears in B), that was not observed in the diluted sample and might contain inter-molecular information.*

Experiment	δ_1	δ_2	origin	max. distance
a)	20/28 Ser Cβ	31/35 Asn Cβ	intra-molecular	7Å
a)	20/28 Ser Cβ	34 Ser Cβ	intra-molecular	7Å
b)	20/28 Ser Cβ	26 Ile Cγ_1	intra-molecular	7Å
a),b)	14/22/31/35 Asn Cβ	15/23 Phe Cδ	intra-molecular	7Å
c)	14 Asn/15 Phe/16 Leu Cβ	10 Gln Cγ/32 Val Cβ	inter/(intra)	7Å

Table 3.2: *Ambiguous through-space contacts observed in PDSD spectra of a diluted (a,b) and an uniformly labelled sample (c). The mixing times applied were 500 ms (a), and 800 ms (b,c).*

3.8 Structural models

Based on secondary structure analysis, two theoretical structural models are proposed. The first one is based on the TALOS-N analysis and the second one on secondary chemical shifts, as well as on reduced cross-peak intensities for certain residues. Moreover, by adding the above mentioned intra-molecular, ambiguous distance restraints, one additional structural model was calculated by the simulated annealing program Cyana. The first two models are shown in Figure 3.24, and a draft of the Cyana model is shown in Figure 3.25.

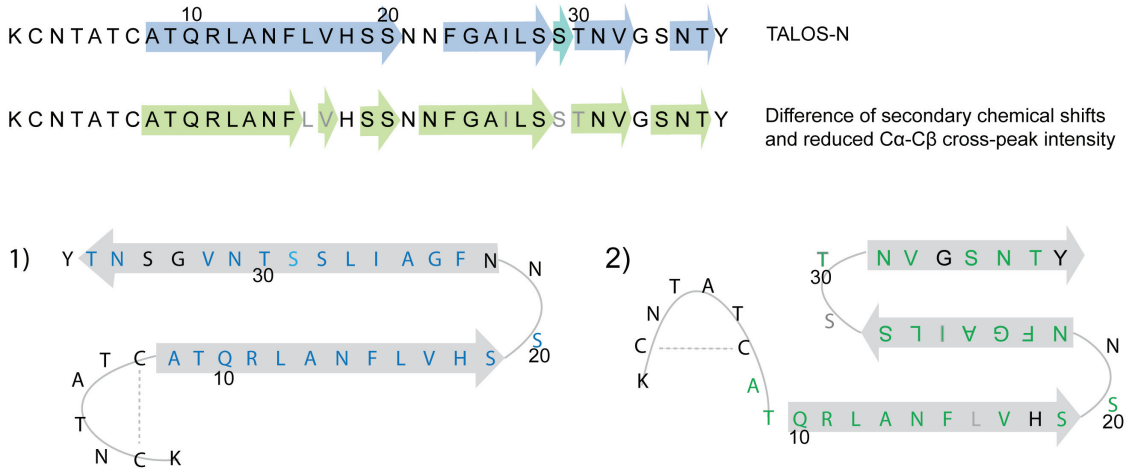

Figure 3.24: *Two possible structural models of fibrillar IAPP. Model 1) employs the widely accepted β-strand-turn- β-strand motif and is based on the TALOS-N results. Model 2) shows a β-serpentine-fold. This second model is based on differences of secondary chemical shifts. Additionally, it takes into account the reduced Cα-Cβ cross-peak intensities as observed for some residues in PDSD spectra (grey letters) and the propensity of certain residues to be part of a turn.*

β-strand-turn-β-strand motif The first theoretical model is a hairpin-type model, which is based on the TALOS-N analysis. It consists of two long β-strands, separated by a β-turn spanning positions 19-Ser to 22-Asn. This model is similar to the ssNMR model, published in 2007 by Luca et al. [33]. The main differences are the lengths of the β-strands and, as a result, the length of the loop. In the former model, an unstructured loop comprises residues 18-27. In the present model, there is no random-coil loop, but rather a constrained β-turn, comprising only four residues. Therefore, in the current model, the amyloidogenic segment ^{22}NFGAILS^{28} is part of the second β-strand. The formation of a β-strand by these residues is clearly indicated by the observed secondary chemical shifts, which show a typical deviation towards β-structure. Furthermore, cross-peaks of this segment, with 26-Ile as only exception, show a high intensity.

Even if this model represents the classical β-strand-turn-β-strand motif, its plausibility suffers, because the two long β-strands are not favorable from the perspective of stability. Furthermore, this model cannot explain the decreased cross-peak intensities of residues Leu-16, Val-17, Ile-26,

Ser-29, and Thr-30, as mentioned in section 3.7.

Serpentine-fold The second model proposed is a serpentine-fold model of three β-strands. It does not only consider the TALOS-N results, but also takes into consideration the unique Cβ-shift of residue 21-Asn, the high probability of finding serine and asparagine residues in β-turns [124], the scattering observed for the Cβ-shift of residue 29-Ser, as well as the reduced intensity of 30-Thr in PDSD spectra. The resulting model consists of three shorter β-strands, separated by two β-turns. Residue 21-Asn is placed in the first β-turn and residues 29-Ser and 30-Thr are placed in the second β-turn.
A serpentine model of IAPP fibrils has been published in 2005 by Kajava et al. [53]. It is almost identical to the model shown here, only in the former model the first β-strand is shorter and stops at position 18-His. Thus, also the relative arrangement of 1st and 2nd β-strand is shifted by one residue position.
The serpentine fold enables a much more compact packing of shorter β-strands. It provides the segment ^{10}QRLANFLVHS^{19} as a possible interaction surface for a second IAPP molecule. This segment has been shown to be important for IAPP self-association [125]. A symmetric dimer model could be based on two molecules building a shared interface at positions ^{10}QRLANFLVHS^{19}.

Cyana structural model A third model was prepared by a Cyana structure calculation. In this model, two identical molecules *k* and *l* were simulated, stacked on top of each other in an in-register-parallel arrangement. The structure calculation employs the four experimentally derived ambiguous intra-molecular distance restraints, TALOS-N dihedral angles ϕ and ψ, and β-sheet characteristic inter-molecular distance restraints for segments (8-15, 19-20, 23-28, 32-32, 36-36). The two simulated molecules and the restraints are shown in Figure 3.25. The distances in between stacked β-strands of molecule *k* and *l*, are indicated in section B) in the same Figure.
The model shows a fold, which has similarly been proposed in a cryo-EM study on fibrillar Aβ_{40} in 2008 [26]. However, due to the small number of distance restraints used in this model, it must not be overestimated. Rather, the structure calculation serves as an exemplary input for a calculation, when more experimental restraints are found.

3.9 Proposed labelling schemes

Based on the two theoretical structural models described before, ideas for future labelling approaches were generated. It is important, that no overlapping resonances are produced by the labelling strategy. Recombinant expression of the protein is not applicable to implement these labelling schemes, as only single amino acids shall be labelled. Instead, solid-phase synthesis is a method for production of IAPP with specifically labelled spin systems [17].
Two labelling strategies are deduced from each structural model, as shown in Figure 3.26 and listed below. Residues that face each-other in the mating β-strands, are targets for selective la-

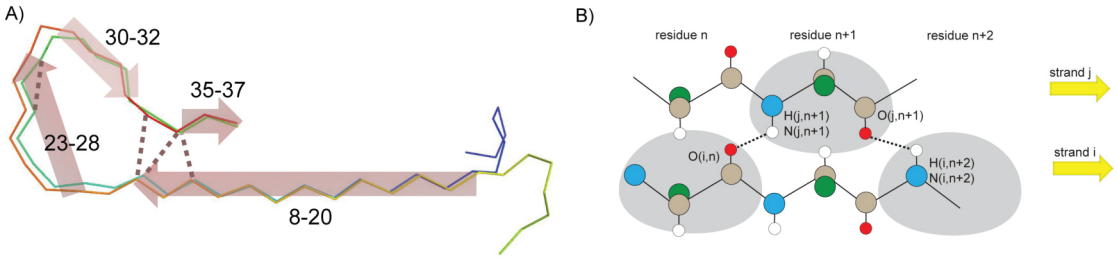

Figure 3.25: *A) Structural model of two identical molecules calculated with Cyana. The simulation was based on four distance restraints, TALOS-N dihedral angles, and inter-molecular distance restraints defining the parallel-in-register β-sheet arrangement. The inter-molecular β-sheet distances are indicated in B). The long fibril axis sticks out of the surface in A) and is parallel to the paper surface in B).*

belling. As the orientation of side-chains is yet unknown, two possibilities for each residue are taken into account. The difference in between the models A) and B) is the orientation of the side-chains in the β-strands.

- 1A) 8-Ala, 14-Asn, 21-Asn, 26-Ile, 28-Ser, 34-Ser, 37-Tyr
- 1B) 11-Arg, 15-Phe, 25-Ala, 27-Leu, 29-Ser, 31-Asn
- 2A) 23-Phe, 25-Ala, 27-Leu, 33-Gly, 35-Asn
- 2B) 24-Gly, 26-Ile, 28-Ser, 32-Val, 34-Ser

Schemes 1A) and 2A) complement each other, as well as 1B) and 2B). The observation of a 14-Asn-28-Ser or 14-Asn-26-Ile cross-peak could arise from model 1A) or 2A). However, 8-Ala-34-Ser points to model 1A), and 21-Asn-37-Tyr points to model 2A).
Equally, the observation of 15-Phe-27-Leu or 15-Phe-25-Ala points to model 1B) or 2B), while 11-Arg-31-Asn or 11-Arg-29-Ser is favored by 1B) and 24-Gly-34-Ser by 2B).
For a decreased ambiguity of the observed cross-peaks, these labelling schemes should be used in diluted samples. One labelled monomer should be mixed with 4 parts of unlabelled monomer before fibrillation, to increase the probability to obtain cross-peaks of intra-molecular origin.

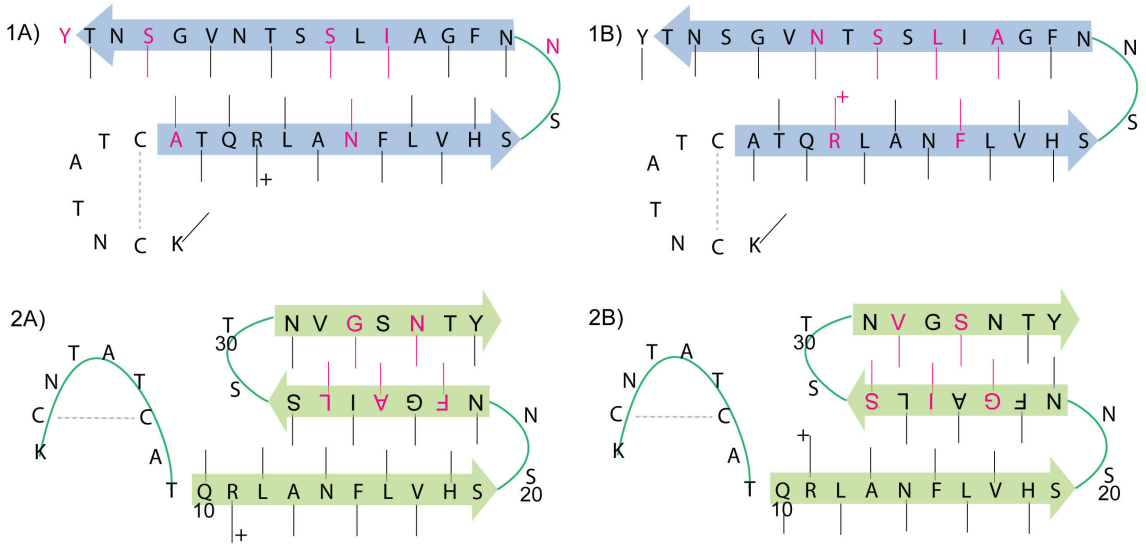

Figure 3.26: *Four different proposed labelling schemes, based on the theoretical structural models. Labelled amino acid residues are indicated by pink letters and side-chains. Strategies 1A) and 2A) complement each other, as well as 1B) and 2B). Such a labelling scheme requires solid-phase synthesis of the peptide and is not realizable with recombinant expression.*

4. Conclusion

The described structural study on IAPP by solid-state NMR provided insights on the secondary structure of the molecules in the fibril and gave indications of a possible tertiary fold. The most important aspect of the secondary structure analysis, based on assigned chemical shifts, was the formation of a β-strand by the amyloidogenic segment (23-28) and the observation of intermediate flexibility of the N-terminal loop (1-8) [19].
Based on further examination of NMR spectra, two theoretical structural models have been proposed and one exemplary structure calculation with the simulated annealing algorithm Cyana was performed.

In the course of the project, four samples with different labelling schemes were produced and examined. Those were an uniformly ^{13}C, ^{15}N labelled sample, a diluted labelled sample (1:4), and two selectively and extensively labelled samples. The fibrillar structure in the samples was reproducible, as cross-peaks appeared at the same chemical shifts values.
The site-specific resonance assignment was done on the uniformly ^{13}C, ^{15}N labelled sample. The experiments that provided the most useful spectra for assignment were PDSD experiments of different mixing times (5 to 200 ms), DREAM, SPC5, PAR, 2D and 3D NCαCβ, and a 3D NCOCX with 80 ms mixing time. PDSD experiments, which were acquired with MAS frequencies close to a rotational resonance condition (9375 Hz at 600 MHz, 12500 Hz at 800 MHz), provided valuable cross-peaks for the assignment of carbonyl resonances (20 ms mixing) and sequential linking (200 ms mixing time).
After the resonance assignment was achieved, mainly long-mixing time PDSD spectra were applied to extract structural information from the spectra. Here, the diluted sample in complement with the uniformly labelled sample provided the most valuable information.
For a structure calculation, the computer program Cyana was applied and provided reproducible results. With a higher number of experimentally obtained distance restraints, the prepared input file will serve to calculate the tertiary structure of fibrillar IAPP.

5. Publications

1.) **Structural Characterization of Fibrils from Recombinant Human Islet Amyloid Polypeptide by Solid-State NMR: The Central FGAILS Segment Is Part of the Beta-Sheet Core**
Franziska Weirich, Lothar Gremer, Ewa A. Mirecka, Stephanie Schiefer, Wolfgang Hoyer, Henrike Heise.
Journal: PLoS One, Impact factor: 3.5 (2016)
Status: published
The contribution to this publication was circa 85 % and the tasks conducted comprise:
Protein expression and purification, Fibrillation, Conduction of solid-state NMR experiments, Site-specific resonance assignment, Analysis of chemical shifts with TALOS, Interpretation of data, Writing of manuscript.
The text of the publication is included in this thesis on pages 23 to 26 and 44 to 61 with minor adaptions in wording and formatting. The Figures of the publication are included in this thesis.

2.) **Methods for Complex Systems - Isotopically Enriched Systems**
Claudia Beumer, Anna König, Daniel Schölzel, Boran Uluca, Franziska Weirich, Henrike Heise.
Chapter in Book: Modern Methods in Solid-State NMR. A Practitioner's Guide
Publisher: Royal Society of Chemistry
Status: accepted. Will be published in autumn 2017
The contribution to this book chapter was circa 15 %.
The book chapter is not included in this thesis.

3.) **Conformational Ensembles of α-synuclein in Different Conformational States Studied by DNP-enhanced ssNMR at Low Temperature**
Boran Uluca, Thibault Viennet, Dusan Petrovic, Hamed Shaykhalishahi, Franziska Weirich, Aysenur Gönülalan, Birgit Strodel, Manuel Etzkorn, Wolfgang Hoyer, Henrike Heise.
Journal: Journal of the American Chemical Society, Impact factor 13.8 (2016)
Status: submitted (July 2017)
The contribution to this publication was circa 20 % and the tasks conducted comprise:
Conducting experiments, Interpretation of data, Writing of manuscript. The publication is not included in this thesis.

6. Supporting Information

6.1 Cyana input file

The cyana input file was created to simulate two identical monomers that are stacked on top of each other. The seven required files are shown underneath.

1. **sequence.seq**

```
LYS 1
CYSS 2
...
TYR 37

PL 98
LL2 99
...
LL2 129
LP 130

LYS 201
CYSS 202
...
TYR 237
```

2. **Calc.cya**

```
name  := IAPP_monomer
prot  := shifts.prot     # input chemical shift list
read upl distances.upl
read lol distances_low.lol
read aco talos.aco
seed=45667
calc_all structures=100 command=anneal steps=10000
overview iapp_monomer.ovw structures=20 pdb
```

3. **init.cya**

```
name := IAPP
welldefined := "8-15,19-20,23-28,31-32,35-36,208-215,219-220,223-228,231-232,235-236"
cyanalib
read seq IAPP.seq
molecules define 1..37 201..237
molecules identity selection="* $welldefined" #info=full
weight_ide=0.15
```

4. **shifts.prot**

```
1 122.971 0.000 N 1
2 54.676 0.269 CA 1
3 999.000 0.000 HA 1
4 32.792 0.242 CB 1
5 999.000 0.000 HB2 1
6 999.000 0.000 HB3 1
7 999.000 0.000 QB 1
8 25.062 0.262 CG 1
9 999.000 0.000 HG2 1
10 999.000 0.000 HG3 1
11 999.000 0.000 QG 1
12 29.682 0.222 CD 1
13 999.000 0.000 HD2 1
14 999.000 0.000 HD3 1
15 999.000 0.000 QD 1
16 41.753 0.250 CE 1
17 999.000 0.000 HE2 1
18 999.000 0.000 HE3 1
19 999.000 0.000 QE 1
20 999.000 0.000 NZ 1
21 999.000 0.000 HZ1 1
22 999.000 0.000 HZ2 1
23 999.000 0.000 HZ3 1
24 999.000 0.000 QZ 1
25 174.101 0.208 C 1
..
1145 122.971 0.000 N 201
1146 54.676 0.269 CA 201
1147 999.000 0.000 HA 201
```

```
1148 32.792 0.242 CB 201
1149 999.000 0.000 HB2 201
1150 999.000 0.000 HB3 201
1151 999.000 0.000 QB 201
1152 25.062 0.262 CG 201
1153 999.000 0.000 HG2 201
1154 999.000 0.000 HG3 201
1155 999.000 0.000 QG 201
1156 29.682 0.222 CD 201
1157 999.000 0.000 HD2 201
1158 999.000 0.000 HD3 201
1159 999.000 0.000 QD 201
1160 41.753 0.250 CE 201
1161 999.000 0.000 HE2 201
1162 999.000 0.000 HE3 201
1163 999.000 0.000 QE 201
1164 999.000 0.000 NZ 201
1165 999.000 0.000 HZ1 201
1166 999.000 0.000 HZ2 201
1167 999.000 0.000 HZ3 201
1168 999.000 0.000 QZ 201
1169 174.101 0.208 C 201
```

5. **talos.aco**

```
8 ALA PHI -160.0 -111.2
8 ALA PSI 120.6 160.8
9 THR PHI -139.4 -82.2
9 THR PSI 108.9 148.9
..
208 ALA PHI -160.0 -111.2
208 ALA PSI 120.6 160.8
209 THR PHI -139.4 -82.2
209 THR PSI 108.9 148.9
..
```

6. **distances.upl**

```
# beta-strand
9 THR N 208 ALA O 3.00
9 THR H 208 ALA O 2.00
9 THR O 210 GLN H 2.00
```

```
9 THR O 210 GLN N 3.00
...
# Disulfide bridge
2 CYSS SG 7 CYSS SG 2.1
2 CYSS SG 7 CYSS CB 3.1
2 CYSS CB 7 CYSS SG 3.1
...
# 1st Ambiguous distance restraint
34 SER CB 20 SER CB 6.5
34 SER CB 28 SER CB 0.0
234 SER CB 220 SER CB 6.5
234 SER CB 228 SER CB 0.0
...
# 3rd ambiguous distance restraint (weight 0.5)
15 PHE CE2 35 ASN CA 6.5 0.5
15 PHE CE2 31 ASN CA 0.0
15 PHE CE2 14 ASN CA 0.0
215 PHE CE2 235 ASN CA 6.5 0.5
215 PHE CE2 231 ASN CA 0.0
215 PHE CE2 214 ASN CA 0.0
# 2nd interpretation of above ambiguous distance restraint (weight 0.5)
37 TYR CD2 35 ASN CA 6.5 0.5
37 TYR CD2 31 ASN CA 0.0
37 TYR CD2 14 ASN CA 0.0
237 TYR CD2 235 ASN CA 6.5 0.5
237 TYR CD2 231 ASN CA 0.0
237 TYR CD2 214 ASN CA 0.0
...
```

7. **distances.lol**

```
9 THR N 208 ALA O 2.70
9 THR H 208 ALA O 1.80
9 THR O 210 GLN H 1.80
9 THR O 210 GLN N 2.70
...
# 1st ambiguous distance restraint
34 SER CB 20 SER CB 1.8
34 SER CB 28 SER CB 0.0
234 SER CB 220 SER CB 1.8
234 SER CB 228 SER CB 0.0
```

```
...
# 3rd ambiguous distance restraint
15 PHE CE2 35 ASN CA 1.8 0.5
15 PHE CE2 31 ASN CA 0.0
15 PHE CE2 14 ASN CA 0.0
215 PHE CE2 235 ASN CA 1.8 0.5
215 PHE CE2 231 ASN CA 0.0
215 PHE CE2 214 ASN CA 0.0
# 2nd interpretation of above restraint
37 TYR CD2 35 ASN CA 1.8 0.5
37 TYR CD2 31 ASN CA 0.0
37 TYR CD2 14 ASN CA 0.0
237 TYR CD2 235 ASN CA 1.8 0.5
237 TYR CD2 231 ASN CA 0.0
237 TYR CD2 214 ASN CA 0.0
```

6.2 Supporting Data

Table S1, Experimental details **Sample 1**										**Sample 2**	**DNP**
	INEPT 1D	PDSD 2D	SPC5_3 2D	DREAM 2D	NHHC 2D	NCaCB 2D	NCaCX 3D	NCaCB 3D	NCOCX DARR 3D	PDSD 2D	SPC5_2 2D
Mixing time		1) 20 ms 2) 200 ms			50 µs		80 ms		80 ms	50 ms	
^{1}H frequency (MHz)	600	800	600	600	600	600	600	600	600	600	600
MAS (Hz)	11000	1) 11000 2) 12500	11000	22000	11000	22000	11000	22000	14000	11000	8000
VT gas temperature	0°C	0°C	0°C	0°C	0°C	0°C	0°C	0°C	-10°C	-10°C	100 Kelvin
Transfer 1	HC-CP	HC-CP	HC-CP	HC-CP	HN-CP	HN-CP	HN-CP	HN-CP	HN-CP	HC-CP	HC-CP
Carrier (ppm)	55	55	40	57	110	120	120	120	120	90	135
Duration of 1st transfer	200 µs	200 µs	600 µs	200 µs	200 µs	400 µs	500 µs	400 µs	400 µs	200 µs	150 µs
Transfer 2		-	-	-	NH-CP	N-CA SPECIFIC CP	N-CA SPECIFIC CP	N-CA SPECIFIC CP	N-CO SPECIFIC CP		
Carrier (ppm)		-	-	-	110	55	55	50	170		
Duration of 2nd transfer					200 µs	1200 µs	1300 µs	1350 µs	1600 µs		
t1 increments	758	750	463	938	463	476	1172	417	537	758	512
t1 spectral width (kHz)	37.8	62.5	46	78.1	46	60	77.7	60	44	37.8	44
t2 increments		240	120	128	16	27	8	12	14	160	160
t2 spectral width (kHz)		40	22	18	4	3.6	2.4	2.4	2.4	33	38
t3 increments							18	18	15		
t3 spectral width (kHz)							4.5	4.5	3		
Number of scans	128	212	256	176	4928	2944	640	352	432	1008	32
Duration	< 1 h	63 h	24 h	24 h	84 h	144 h	216 h	254 h	216 h	187 h	7 h

S1 Table Experimental details.
Sample 1 is fully ^{13}C, ^{15}N-labeled fibrillar IAPP. Sample 2 is fibrillar IAPP with 1 part ^{13}C, ^{15}N-labeled per 4 parts unlabeled peptide. Both samples were expressed and purified equally as described in methods part.

Figure 6.1: *S1 Table. Experimental details of spectra used for site-specific resonance assignment. (PLoS ONE 11(9): e0161243)*

S2 Table, Chemical shifts in ppm

	residue	N	CO	Ca	Cb	Cg	Cd	Ce	Cz
1	K	123.0	174.1	54.6	32.8	25.1	29.7	41.9	
2	c	125.2	173.6	59.2	43.5				
3	N	114.2	176.6	51.3	39.1	176.6			
4	T	119.7	175.8	62.1	66.1	23.9			
5	A	119.3	176.4	51.0	26.8				
6	T	117.1	174.0	61.7	70.2	21.4			
7	c	120.3	173.1	53.2	48.7				
8	A	122.2	175.5	50.7	22.7				
9	T	119.1	172.5	61.8	70.3	21.9			
10	Q	125.8	174.3	54.4	32.2	34.2	179.5		
11	R	125.2	173.5	54.9	30.5	27.3	43.8		159.6
12	L	127.9	172.7	54.8	44.2	29.3	25.1		
13	A	129.4	174.5	51.4	21.2				
14	N	120.5	173.2	52.5	42.8	177.3			
15	F	117.1	173.2	56.6	42.7	137.9	131.6		
16	L	119.2	173.9	56.1	42.0	30.4	25.1/27.6		
17	V	120.7	174.5	60.7	35.8	21.5			
18	H	122.0	175.0	54.3	28.2	131.6			
19	S	124.0	174.0	55.9	64.5				
20	S	124.2	174.7	55.9	64.5				
21	N	127.3	173.0	54.2	36.4				
22	N	118.1	172.2	52.5	42.3				
23	F	121.1	173.7	57.1	40.2	137.8	131.4		
24	G	109.9	171.3	43.9					
25	A	127.9	176.8	50.4	21.8				
26	I	120.4	177.0	60.1	40.5	16.9/27.6	12.4		
27	L	121.5	173.6	54.2	44.5	29.3	23.7/26.8		
28	S	116.3	173.6	55.8	64.5				
29	S	117.5	173.7	58.9	61.7/63.7*				
30	T	114.4	171.4	61.3	74.0	21.3			
31	N	122.3	173.9	52.3	41.3	176.1			
32	V	121.7	174.8	60.5	34.6	20/22.2			
33	G	116.7	174.0	48.0					
34	S	113.1	171.7	58.4	68.4				
35	N	120.0	174.3	52.5	41.9	176.9			
36	T	114.4	173.3	60.7	71.4	21.5			
37	Y	128.5	180.7	60.0	39.5	129.1	132.8	117.8	156.1

S2 Table Chemical shifts in ppm.
Chemical shifts in ppm derived from solid-state NMR experiments and used for TALOS-N predictions and calculation of secondary chemical shifts. Small letters for cysteine residues indicate the oxidized disulfide bridge. The oxidation state is considered by TALOS-N routine. *The second Cβ chemical shift value of 63.7 ppm for S29 corresponds to an additional conformation as observed in the first sample (weak) and in the second sample (strong).

Figure 6.2: *S2 Table. Chemical shifts of recombinant human IAPP in ppm. (PLoS ONE 11(9): e0161243)*

S3 Table, TALOS-N backbone torsion angle predictions						
	residue	φ	ψ	σ_φ	σ_ψ	classification
1	K	-	-	-	-	None
2	C	-69,0	-31,7	9,8	8,8	Warn
3	N	-110,0	129,3	19,8	47,4	Warn
4	T	-66,3	138,5	9,2	13,2	Warn
5	A	-144,5	156,0	11,2	8,2	Strong
6	T	-100,8	134,6	15,8	11,3	Strong
7	C	-138,3	159,4	9,5	8,0	Strong
8	A	-135,6	140,7	12,2	10,0	Strong
9	T	-110,8	128,9	14,3	7,0	Strong
10	Q	-120,1	133,4	10,6	9,4	Strong
11	R	-97,0	124,5	9,9	10,9	Strong
12	L	-118,0	129,1	10,5	7,4	Strong
13	A	-117,9	132,1	10,0	6,6	Strong
14	N	-123,1	141,0	15,0	11,2	Strong
15	F	-136,2	143,5	12,3	11,1	Strong
16	L	-76,4	132,1	11,0	7,9	Strong
17	V	-126,5	134,3	11,6	11,5	Strong
18	H	-91,9	119,3	10,5	7,5	Strong
19	S	-105,5	118,0	10,8	24,8	Strong
20	S	-127,0	132,9	10,0	13,3	Strong
21	N	49,2	47,4	5,2	6,3	Warn
22	N	-131,4	156,0	15,1	12,5	Strong
23	F	-104,8	129,3	15,0	7,7	Strong
24	G	-113,7	148,8	19,0	10,6	Strong
25	A	-119,5	128,3	11,0	6,4	Strong
26	I	-111,7	134,2	12,4	10,7	Strong
27	L	-122,3	131,1	12,2	12,2	Strong
28	S	-125,8	133,6	10,0	9,6	Strong
29	S	50,1	52,3	4,5	8,5	Warn
30	T	-139,3	151,8	8,8	11,4	Strong
31	N	-112,0	129,5	14,6	12,5	Strong
32	V	-122,4	128,5	10,1	13,0	Strong
33	G	-133,3	168,7	45,2	34,9	Warn
34	S	-147,6	152,7	9,4	8,0	Strong
35	N	-128,2	142,2	18,2	10,9	Strong
36	T	-114,1	140,2	17,7	14,7	Strong
37	Y	-	-	-	-	None

S3 Table TALOS-N backbone torsion angle predictions.
Predicted backbone torsion angles for chemical shifts from S2 Table. The Classification describes the consensus of the torsion angle with database values. “Warn” means that there is no consensus in database matches. “Strong” indicates a major consensus in database matches.

Figure 6.3: *S3 Table. TALOS-N backbone torsion angle prediction. (PLoS ONE 11(9): e0161243)*

Bibliography

[1] F. Chiti and C. M. Dobson. Protein misfolding, functional amyloid, and human disease. *Annu. Rev. Biochem.*, 75:333–66, 2006.

[2] T. P. Knowles, M. Vendruscolo, and C. M. Dobson. The amyloid state and its association with protein misfolding diseases. *Nat. Rev. Mol. Cell Biol.*, 15(6):384–96, 2014.

[3] J. D. Sipe and A. S. Cohen. History of the amyloid fibril. *J. Struct. Biol.*, 130:88–98, 2000.

[4] C. M. Dobson. Getting out of shape. *Nature*, 418:729–30, 2002.

[5] M. S. Fernandez. Human IAPP amyloidogenic properties and pancreatic beta-cell death. *Cell Calcium*, 56(5):416–27, 2014.

[6] D. Eisenberg and M. Jucker. The amyloid state of proteins in human diseases. *Cell*, 148:1188–1203, 2016.

[7] D. J. Selkoe. Folding proteins in fatal ways. *Nature*, 426:900–904, 2003.

[8] A. K. Buell, C. M. Dobson, and T. P. Knowles. The physical chemistry of the amyloid phenomenon: Thermodynamics and kinetics of filamentous protein aggregation. *Essays Biochem.*, 56:11–39, 2014.

[9] R. Tycko. Physical and structural basis for polymorphism in amyloid fibrils. *Protein Sci.*, 23(11):1528–39, 2014.

[10] H. Müller, M. Etzkorn, and H. Heise. Solid-state NMR spectroscopy of proteins. *Top. Curr. Chem.*, 335:121–56, 2013.

[11] H. Van Melckebeke, C. Wasmer, A. Lange, E. Ab, A. Loquet, A. Böckmann, and B. H. Meier. Atomic-resolution three-dimensional structure of Het-S(218-289) amyloid fibrils by solid-state NMR spectroscopy. *J. Am. Chem. Soc.*, 132(39):13765–75, 2010.

[12] Y. Xiao, B. Ma, D. McElheny, S. Parthasarathy, F. Long, M. Hoshi, R. Nussinov, and Y. Ishii. Abeta(1-42) fibril structure illuminates self-recognition and replication of amyloid in Alzheimer's disease. *Nat. Struct. Mol. Biol.*, 22(6):499–505, 2015.

[13] M. D. Tuttle, G. Comellas, A. J. Nieuwkoop, D. J. Covell, D. A. Berthold, K. D. Kloepper, J. M. Courtney, J. K. Kim, A. M. Barclay, A. Kendall, W. Wan, G. Stubbs, C. D. Schwieters,

V. M. Lee, J. M. George, and C. M. Rienstra. Solid-state NMR structure of a pathogenic fibril of full-length human alpha-synuclein. *Nat. Struct. Mol. Biol.*, 23(5):409–15, 2016.

[14] M.A. Wälti, F. Ravotti, H. Arai, C.G. Glabe, J.S. Wall, A. Böckmann, P. Güntert, B.H. Meier, and R. Riek. Atomic-resolution structure of a disease-relevant Abeta(1-42) amyloid fibril. *Proc. Natl. Acad. Sci. USA*, 113(34):E4976–84, 2016.

[15] M. T. Colvin, R. Silvers, Q. Z. Ni, T. V. Can, I. Sergeyev, M. Rosay, K. J. Donovan, B. Michael, J. Wall, S. Linse, and R. G. Griffin. Atomic resolution structure of monomorphic Abeta 42 amyloid fibrils. *J. Am. Chem. Soc.*, 138(30):9663–9674, 2016.

[16] M. J. Bayro, M. Huber, R. Ramachandran, T. C. Davenport, B. H. Meier, M. Ernst, and R. G. Griffin. Dipolar truncation in magic-angle spinning NMR recoupling experiments. *J. Chem. Phys.*, 130(11):114506, 2009.

[17] C. Beumer, A. König, D. Schölzel, B. Uluca, F. Weirich, and H. Heise. Methods for complex systems - isotopically enriched systems. In P. Hodgkinson, editor, *Modern Methods in solid-state NMR: a practitioners guide*, volume 12 of *New Developments in NMR*. Royal Society of Chemistry, London, 2017.

[18] S. E. Kahn, S. Andrikopoulos, and C. B. Verchere. Islet amyloid: a long-recognized but underappreciated pathological feature of type 2 diabetes. *Diabetes.*, 48(2):241–253, 1999.

[19] F. Weirich, L. Gremer, E. A. Mirecka, S. Schiefer, W. Hoyer, and H. Heise. Structural characterization of fibrils from recombinant human islet amyloid polypeptide by solid-state NMR: The central FGAILS segment is part of the beta-sheet core. *PLoS One*, 11(9):e0161243, 2016.

[20] P. Güntert and L. Buchner. Combined automated NOE assignment and structure calculation with Cyana. *J. Biomol. NMR*, 62:453–471, 2015.

[21] M. Sunde, L. C. Serpell, M. Bartlam, P. E. Fraser, M. B. Pepys, and C. C. Blake. Common core structure of amyloid fibrils by synchrotron X-ray diffraction. *J. Mol. Biol.*, 273:729–739, 1997.

[22] M. R. Sawaya, S. Sambashivan, R. Nelson, M. I. Ivanova, S. A. Sievers, M. I. Apostol, M. J. Thompson, M. Balbirnie, J. J. Wiltzius, H. T. McFarlane, A. O. Madsen, C. Riekel, and D. Eisenberg. Atomic structures of amyloid cross-beta spines reveal varied steric zippers. *Nature*, 447(7143):453–7, 2007.

[23] R. Tycko. Molecular structure of amyloid fibrils: Insights from solid-state NMR. *Q. Rev. Biophys.*, 39(1):1–55, 2006.

[24] A. Der-Sarkissian, C. C. Jao, J. Chen, and R. Langen. Structural organization of alpha-synuclein fibrils studied by site-directed spin labeling. *J. Biol. Chem.*, 278(39):37530–5, 2003.

[25] S. A. Jayasinghe and R. Langen. Identifying structural features of fibrillar islet amyloid polypeptide using site-directed spin labeling. *J. Biol. Chem.*, 279(46):48420–5, 2004.

[26] C. Sachse, M. Fändrich, and N. Grigorieff. Paired beta-sheet structure of an Abeta(1-40) amyloid fibril revealed by electron microscopy. *Proc. Natl. Acad. Sci. USA*, 105:7462–7466, 2008.

[27] M. Schmidt, A. Rohou, K. Lasker, J. K. Yadav, C. Schiene-Fischer, M. Fändrich, and N. Grigorieff. Peptide dimer structure in Abeta(1-42) fibril visualized with cryo-EM. *Proc. Natl. Acad. Sci. USA*, 112:11858–1186, 2015.

[28] D. E. Otzen, editor. *Amyloid Fibrils and Prefibrillar Aggregates: Molecular and Biological Properties*. Wiley-VCH, Weinheim, Germany, 1st edition, 2013.

[29] R. Riek and D.S. Eisenberg. The activities of amyloids from a structural perspective. *Nature*, 539(1):227–235, 2016.

[30] J. R. Lewandowski, P. C. van der Wel, M. Rigney, N. Grigorieff, and R. G. Griffin. Structural complexity of a composite amyloid fibril. *J. Am. Chem. Soc.*, 133(37):14686–98, 2011.

[31] A. K. Schütz, T. Vagt, M. Huber, O. Y. Ovchinnikova, R. Cadalbert, J. Wall, P. Güntert, A. Böckmann, R. Glockshuber, and B. H. Meier. Atomic-resolution three-dimensional structure of Amyloid beta fibrils bearing the Osaka mutation. *Angew. Chem. Int. Ed. Engl.*, 54(1):331–5, 2015.

[32] S. I. Cohen, M. Vendruscolo, M. E. Welland, C. M. Dobson, E. M. Terentjev, and T. P. Knowles. Nucleated polymerization with secondary pathways. I. Time evolution of the principal moments. *J. Chem. Phys.*, 135:065–105, 2011.

[33] S. Luca, W. M. Yau, R. Leapman, and R. Tycko. Peptide conformation and supramolecular organization in amylin fibrils: Constraints from solid-state NMR. *Biochemistry*, 46(47):13505–22, 2007.

[34] J. X. Lu, W. Qiang, W. M. Yau, C. D. Schwieters, S. C. Meredith, and R. Tycko. Molecular structure of beta-Amyloid fibrils in Alzheimer's disease brain tissue. *Cell*, 154(6):1257–68, 2013.

[35] S. E. Kahn, D. A. D'Alessio, M. W. Schwartz, W. Y. Fujimoto, J. W. Ensinck, G. J. Taborsky, and D. Porte. Evidence of cosecretion of islet amyloid polypeptide and insulin by beta-cells. *Diabetes*, 39(5):634–8, 1990.

[36] T. A. Lutz. Control of energy homeostasis by amylin. *Cell. Mol. Life Sci.*, 69(12):1947–65, 2012.

[37] A. Abedini and A. M. Schmidt. Mechanisms of islet amyloidosis toxicity in type 2 diabetes. *FEBS Lett.*, 587(8):1119–27, 2013.

[38] Q. Qiao, G. R. Bowman, and X. Huang. Dynamics of an intrinsically disordered protein reveal metastable conformations that potentially seed aggregation. *J. Am. Chem. Soc.*, 135(43):16092–101, 2013.

[39] J. D. Knight, J. A. Williamson, and A. D. Miranker. Interaction of membrane-bound islet amyloid polypeptide with soluble and crystalline insulin. *Protein Sci.*, 17(10):1850–1856, 2008.

[40] A. T. Alexandrescu, S. Jha, J. M. Snell, and S. R. Sheftic. The pH-dependence of amylin fibrillization. *Biophys. J.*, 104(2):360a–360a, 2013.

[41] A. Lorenzo, B. Razzaboni, G. C. Weir, and B. A. Yankner. Pancreatic islet cell toxicity of amylin associated with type-2 diabetes mellitus. *Nature*, 368(6473):756–760, 1994.

[42] P. Cao, A. Abedini, and D. P. Raleigh. Aggregation of islet amyloid polypeptide: From physical chemistry to cell biology. *Curr. Opin. Struct. Biol.*, 23(1):82–89, 2013.

[43] P. Westermark, A. Andersson, and G. T. Westermark. Islet amyloid polypeptide, islet amyloid, and diabetes mellitus. *Physiol. Rev.*, 91(3):795–826, 2011.

[44] R. Akter, P. Cao, H. Noor, Z. Ridgway, L. H. Tu, H. Wang, A. G. Wong, X. Zhang, A. Abedini, A. M. Schmidt, and D. P. Raleigh. Islet amyloid polypeptide: Structure, function, and pathophysiology. *J. Diabetes Res.*, 2016:2798269, 2016.

[45] S. M. Butterfield and H. A. Lashuel. Amyloidogenic protein-membrane interactions: Mechanistic insight from model systems. *Angew. Chem. Int. Ed. Engl.*, 49(33):5628–54, 2010.

[46] M. F. Sciacca, F. Lolicato, G. Di Mauro, D. Milardi, L. D'Urso, C. Satriano, A. Ramamoorthy, and C. La Rosa. The role of cholesterol in driving IAPP-membrane interactions. *Biophys. J.*, 111(1):140–51, 2016.

[47] P. Westermark, U. Engstrom, K. H. Johnson, G. T. Westermark, and C. Betsholtz. Islet amyloid polypeptide: Pinpointing amino-acid residues linked to amyloid fibril formation. *Proc. Natl. Acad. Sci. USA*, 87(13):5036–40, 1990.

[48] S. M. Cope, S. Shinde, R. B. Best, G. Ghirlanda, and S. M. Vaiana. Cyclic N-terminal loop of amylin forms non amyloid fibers. *Biophys. J.*, 105(7):1661–9, 2013.

[49] M. R. Nilsson and D. P. Raleigh. Analysis of amylin cleavage products provides new insights into the amyloidogenic region of human amylin. *J. Mol. Biol.*, 294(5):1375–85, 1999.

[50] E. T. Jaikaran, C. E. Higham, L. C. Serpell, J. Zurdo, M. Gross, A. Clark, and P. E. Fraser. Identification of a novel human islet amyloid polypeptide beta-sheet domain and factors influencing fibrillogenesis. *J. Mol. Biol.*, 308(3):515–25, 2001.

[51] O. Sumner-Makin and L. C. Serpell. Structural characterisation of islet amyloid polypeptide fibrils. *J. Mol. Biol.*, 335(5):1279–1288, 2004.

[52] C. S. Goldsbury, G. J. Cooper, K. N. Goldie, S. A. Müller, E. L. Saafi, W. T. Gruijters, M. P. Misur, A. Engel, U. Aebi, and J. Kistler. Polymorphic fibrillar assembly of human amylin. *J. Struct. Biol.*, 119(1):17–27, 1997.

[53] A. V. Kajava, U. Aebi, and A. C. Steven. The parallel superpleated beta-structure as a model for amyloid fibrils of human amylin. *J. Mol. Biol.*, 348(2):247–252, 2005.

[54] J. J. Wiltzius, S. A. Sievers, M. R. Sawaya, D. Cascio, D. Popov, C. Riekel, and D. Eisenberg. Atomic structure of the cross-beta spine of islet amyloid polypeptide (amylin). *Protein Sci.*, 17(9):1467–74, 2008.

[55] S. Bedrood, Y. Li, J. M. Isas, B. G. Hegde, U. Baxa, I. S. Haworth, and R. Langen. Fibril structure of human islet amyloid polypeptide. *J. Biol. Chem.*, 287(8):5235–41, 2012.

[56] A. T. Alexandrescu. Amide proton solvent protection in amylin fibrils probed by quenched hydrogen exchange NMR. *PLoS One*, 8(2):e56467, 2013.

[57] T. Hard. Amyloid fibrils: Formation, polymorphism, and inhibition. *J. Phys. Chem. Lett.*, 5(3):607–14, 2014.

[58] E. A. Mirecka, S. Feuerstein, L. Gremer, G. F. Schröder, M. Stoldt, D. Willbold, and W. Hoyer. Beta-hairpin of islet amyloid polypeptide bound to an aggregation inhibitor. *Sci Rep*, 6:33474, 2016.

[59] E. A. Mirecka, L. Gremer, S. Schiefer, F. Oesterhelt, M. Stoldt, D. Willbold, and W. Hoyer. Engineered aggregation inhibitor fusion for production of highly amyloidogenic human islet amyloid polypeptide. *J. Biotechnol.*, 191:221–7, 2014.

[60] J. Cavanagh, W. J. Fairbrother, A. G. Palmer, M. Rance, and N. J. Skelton. *Protein NMR spectroscopy*. Elsevier Academic Press, 2nd edition, 2007.

[61] M. J. Duer. *Solid-State NMR Spectroscopy*. Blackwell Publishing, Oxford, 2004.

[62] M. H. Levitt. *Spin Dynamics*. Wiley, 2nd edition, 2008.

[63] J. Keeler. *Understanding NMR Spectroscopy*. Wiley, 2nd edition, 2010.

[64] S. Jehle, M. Falb, J. P. Kirkpatrick, H. Oschkinat, B. J. van Rossum, G. Althoff, and T. Carlomagno. Intermolecular protein-RNA interactions revealed by 2D 31P-15N magic angle spinning solid-state NMR spectroscopy. *J. Am. Chem. Soc.*, 132(11):3842–6, 2010.

[65] R. Linser, M. Dasari, M. Hiller, V. Higman, U. Fink, J. M. Lopez del Amo, S. Markovic, L. Handel, B. Kessler, P. Schmieder, D. Oesterhelt, H. Oschkinat, and B. Reif. Proton-detected solid-state NMR spectroscopy of fibrillar and membrane proteins. *Angew. Chem. Int. Ed. Engl.*, 50(19):4508–12, 2011.

[66] A. J. Nieuwkoop, W. T. Franks, K. Rehbein, A. Diehl, U. Akbey, F. Engelke, L. Emsley, G. Pintacuda, and H. Oschkinat. Sensitivity and resolution of proton detected spectra of a deuterated protein at 40 and 60 kHz magic angle spinning. *J. Biomol. NMR.*, 61(2):161–171, 2015.

[67] H. Heise. Solid-state NMR Spectroscopy. In J. K. G. Dhont, G. Gompper, P. R. Lang, D. Richter, M. Ripoll, D. Willbold, and R. Zorn, editors, *Macromolecular Systems in Soft and Living Matter*, volume 20 of *Key Technologies*. Forschungszentrum Jülich, Jülich, Germany, 2011.

[68] N. M. Szeverenyi, M. J. Sullivan, and G. E. Maciel. Observation of spin exchange by two-dimensional fourier transform 13C cross polarization magic-angle spinning. *J. Magn. Reson.*, 47:462–475, 1982.

[69] D. D. Laws, H. M. L. Bitter, and A. Jerschow. Methoden der Festkörper NMR Spektroskopie in der Chemie. *Angew. Chem.*, 114:3224–3259, 2002.

[70] A. Bockmann, M. Ernst, and B. H. Meier. Spinning proteins, the faster, the better? *J. Magn. Reson.*, 253:71–9, 2015.

[71] V. Agarwal, S. Penzel, K. Szekely, R. Cadalbert, E. Testori, A. Oss, J. Past, A. Samoson, M. Ernst, A. Böckmann, and B. H. Meier. De novo 3D structure determination from sub-milligram protein samples by solid-state 100 kHz MAS NMR spectroscopy. *Angew. Chem. Int. Ed. Engl.*, 53(45):12253–6, 2014.

[72] B. M. Fung, A. K. Khitrin, and K. Ermolaev. An improved broadband decoupling sequence for liquid crystals and solids. *J. Magn. Reson.*, 142(1):97–101, 2000.

[73] A. Schütz, C. Wasmer, B. Habenstein, R. Verel, J. Greenwald, R. Riek, A. Böckmann, and B.H. Meier. Protocols for the sequential solid-state NMR spectroscopic assignment of an uniformly labeled 25 kDa protein: Het-S(1-227). *ChemBioChem*, 11(11):1543–51, 2010.

[74] S. B. Wishart DS. The 13C chemical-shift index: A simple method for the identification of protein secondary structure using 13C chemical-shift data. *J. Biomol. NMR*, 4(2):171–180, 1994.

[75] D. S. Wishart, C. G. Bigam, A. Holm, R. S. Hodges, and B. D. Sykes. 1H, 13C and 15N random coil NMR chemical shifts of the common amino acids. I. Investigations of nearest-neighbor effects. *J. Biomol. NMR*, 5(1):67–81, 1995.

[76] E. L. Ulrich, H. Akutsu, J. F. Doreleijers, Y. Harano, Y. E. Ioannidis, J. Lin, M. Livny, S. Mading, D. Maziuk, Z. Miller, E. Nakatani, C. F. Schulte, D. E. Tolmie, R. Kent Wenger, H. Yao, and J. L. Markley. BioMagResBank. *Nucleic Acids Res.*, 36:D402–8, 2008.

[77] H. Zhang, S. Neal, and D. S. Wishart. Refdb: A database of uniformly referenced protein chemical shifts. *J. Biomol. NMR*, 25(3):173–195, 2003.

[78] G. Cornilescu, F. Delaglio, and A. Bax. Protein backbone angle restraints from searching a database for chemical shift and sequence homology. *J. Biomol. NMR*, 13(3):289–302, 1999.

[79] Y. Shen and A. Bax. Protein backbone and sidechain torsion angles predicted from NMR chemical shifts using artificial neural networks. *J. Biomol. NMR*, 56(3):227–241, 2013.

[80] S. Hartmann and E. Hahn. Nuclear double resonance in the rotating frame. *Phys. Rev.*, 128(5):2042–2053, 1962.

[81] M. T. Colvin, R. Silvers, B. Frohm, Y. Su, S. Linse, and R. G. Griffin. High resolution structural characterization of Abeta42 amyloid fibrils by magic angle spinning NMR. *J. Am. Chem. Soc.*, 137(23):7509–18, 2015.

[82] G. A. Morris and R. Freeman. Enhancement of nuclear magnetic-resonance signals by polarization transfer. *J. Am. Chem. Soc.*, 101(3):760–762, 1979.

[83] G. De Paëpe. Dipolar recoupling in magic angle spinning solid-state nuclear magnetic resonance. *Annu. Rev. Phys. Chem.*, 63:661–684, 2012.

[84] K. Takegoshi, S. Nakamura, and T. Terao. 13C-1H dipolar-assisted rotational resonance in magic-angle spinning NMR. *Chem. Phys. Let.*, 344:631–637, 2001.

[85] G. De Paëpe, J. R. Lewandowski, A. Loquet, A. Böckmann, and R. G. Griffin. Proton assisted recoupling and protein structure determination. *J. Chem. Phys.*, 129(24):245101, 2008.

[86] M. Hohwy, C. M. Rienstra, and R. G. Griffin. Band-selective homonuclear dipolar recoupling in rotating solids. *J. Chem. Phys.*, 117(10):4973–4987, 2002.

[87] R. Verel, M. Ernst, and B. H. Meier. Adiabatic dipolar recoupling in solid-state NMR: The DREAM scheme. *J. Magn. Reson.*, 150(1):81–99, 2001.

[88] M. Baldus, A. T. Petkova, J. Herzfeld, and R. G. Griffin. Cross polarization in the tilted frame: Assignment and spectral simplification in heteronuclear spin systems. *Mol. Phys.*, 95(6):1197–1207, 1998.

[89] A. Lange, S. Luca, and M. Baldus. Structural constraints from proton-mediated rare-spin correlation spectroscopy in rotating solids. *J. Am. Chem. Soc.*, 124(33):9704–5, 2002.

[90] F. Delaglio, S. Grzesiek, G. W. Vuister, G. Zhu, J. Pfeifer, and A. Bax. NMRPipe: A multidimensional spectral processing system based on unix pipes. *J. Biomol. NMR*, 6(3):277–93, 1995.

[91] T. J. Stevens, R. H. Fogh, W. Boucher, V. A. Higman, F. Eisenmenger, B. Bardiaux, B. J. van Rossum, H. Oschkinat, and E. D. Laue. A software framework for analysing solid-state MAS NMR data. *J. Biomol. NMR*, 51(4):437–47, 2011.

[92] Q. Z. Ni, E. Daviso, T. V. Can, E. Markhasin, S. K. Jawla, T. M. Swager, R. J. Temkin, J. Herzfeld, and R. G. Griffin. High frequency dynamic nuclear polarization. *Acc. Chem. Res.*, 46(9):1933–1941, 2013.

[93] C. Sauvee, M. Rosay, G. Casano, F. Aussenac, R. T. Weber, O. Ouari, and P. Tordo. Highly efficient, water-soluble polarizing agents for dynamic nuclear polarization at high frequency. *Angew. Chem. Int. Ed. Engl.*, 52(41):10858–10861, 2013.

[94] M. Hohwy, C. M. Rienstra, C. P. Jaroniec, and R. G. Griffin. Fivefold symmetric homonuclear dipolar recoupling in rotating solids: Application to double quantum spectroscopy. *J. Chem. Phys.*, 110(16):7983–7992, 1999.

[95] M. Hong and K. Jakes. Selective and extensive 13C labeling of a membrane protein for solid-state NMR investigations. *J. Biomol. NMR*, 14(1):71–4, 1999.

[96] P. Lundström, K. Teilum, T. Carstensen, I. Bezsonova, S. Wiesner, D. F. Hansen, T. L. Religa, M. Akke, and L. E. Kay. Fractional 13C enrichment of isolated carbons using [1-13C]- or [2- 13C]-glucose facilitates the accurate measurement of dynamics at backbone C-alpha and side-chain methyl positions in proteins. *J. Biomol. NMR*, 38(1):199–212, 2007.

[97] L. Wei, P. Jiang, W. Xu, H. Li, H. Zhang, L. Yan, M. B. Chan-Park, X. W. Liu, K. Tang, Y. Mu, and K. Pervushin. The molecular basis of distinct aggregation pathways of islet amyloid polypeptide. *J. Biol. Chem.*, 286(8):6291–300, 2011.

[98] D. C. R. Camargo, K. Tripsianes, T. G. Kapp, J. Mendes, J. Schubert, B. Cordes, and B. Reif. Cloning, expression and purification of the human islet amyloid polypeptide (hIAPP) from Escherichia coli. *Protein Expr. Purif.*, 106:49–56, 2015.

[99] A. Pines, M. G. Gibby, and J. S. Waugh. Proton-enhanced NMR of dilute spins in solids. *J. Chem. Phys.*, 59(2):569–590, 1973.

[100] H. Heise, W. Hoyer, S. Becker, O. C. Andronesi, D. Riedel, and M. Baldus. Molecular-level secondary structure, polymorphism, and dynamics of full-length alpha-synuclein fibrils studied by solid-state NMR. *Proc. Natl. Acad. Sci. USA*, 102(44):15871–15876, 2005.

[101] I. Kosicka, T. Kristensen, M. Bjerring, K. Thomsen, C. Scavenius, J. J. Enghild, and N. C. Nielsen. Preparation of uniformly 13C, 15N-labeled recombinant human amylin for solid-state NMR investigation. *Protein Expr. Purif.*, 99:119–30, 2014.

[102] A. K. Paravastu, R. D. Leapman, W. M. Yau, and R. Tycko. Molecular structural basis for polymorphism in Alzheimer's beta-Amyloid fibrils. *Proc. Natl. Acad. Sci. USA*, 105(47):18349–54, 2008.

[103] O. C. Andronesi, S. Becker, K. Seidel, H. Heise, H. S. Young, and M. Baldus. Determination of membrane protein structure and dynamics by magic-angle-spinning solid-state NMR spectroscopy. *J. Am. Chem. Soc.*, 127(37):12965–12974, 2005.

[104] K. Seidel, A. Lange, S. Becker, C. E. Hughes, H. Heise, and M. Baldus. Protein solid-state NMR resonance assignments from 13C, 13C correlation spectroscopy. *Phys. Chem. Chem. Phys.*, 6(22):5090, 2004.

[105] D. F. Hansen, P. Neudecker, and L. E. Kay. Determination of isoleucine side-chain conformations in ground and excited states of proteins from chemical shifts. *J. Am. Chem. Soc.*, 132(22):7589–91, 2010.

[106] O. A. Martin, M. E. Villegas, J. A. Vila, and H. A. Scheraga. Analysis of 13C-alpha and 13C-beta chemical shifts of cysteine and cystine residues in proteins: A quantum chemical approach. *J. Biomol. NMR*, 46(3):217–25, 2010.

[107] J. R. Lewandowski. Advances in solid-state relaxation methodology for probing site-specific protein dynamics. *Acc. Chem. Res.*, 46(9):2018–27, 2013.

[108] J. R. Lewandowski, P. C. van der Wel, M. Rigney, N. Grigorieff, and R. G. Griffin. Structural complexity of a composite amyloid fibril. *J. Am. Chem. Soc.*, 133(37):14686–98, 2011.

[109] J. M. Lopez del Amo, M. Schmidt, U. Fink, M. Dasari, M. Fändrich, and B. Reif. An asymmetric dimer as the basic subunit in Alzheimer's disease Amyloid beta fibrils. *Angew. Chem. Int. Ed. Engl.*, 51(25):6136–9, 2012.

[110] H. Saito. Conformation dependent 13C chemical shifts: A new means of conformational characterization as obtained by high-resolution solid-state 13C NMR. *Magn. Reson. Chem.*, 24(10):835–852, 1986.

[111] D. Sharma and K. Rajarathnam. 13C NMR chemical shift can predict disulfide bond formation. *J. Biomol. NMR*, 18(2):165–171, 2000.

[112] M. J. Betts and R. B. Russell. Amino acid properties and consequences of substitutions. In M.R. Barnes and I.C. Gray, editors, *Bioinformatics for Geneticists*. Wiley, New York, 2003.

[113] M. Billeter, W. Braun, and K. Wüthrich. Sequential resonance assignments in protein 1H nuclear magnetic resonance spectra. computation of sterically allowed proton-proton distances and statistical analysis of proton-proton distances in single crystal protein conformations. *J. Mol. Biol.*, 155(3):321–46, 1982.

[114] C. Gardiennet, A. Loquet, M. Etzkorn, H. Heise, M. Baldus, and A. Böckmann. Structural constraints for the Crh protein from solid-state NMR experiments. *J. Biomol. NMR*, 40(4):239–50, 2008.

[115] A. T. Petkova, R. D. Leapman, Z. Guo, W. M. Yau, M. P. Mattson, and R. Tycko. Self-propagating, molecular-level polymorphism in Alzheimer's beta-Amyloid fibrils. *Science*, 307(5707):262–5, 2005.

[116] J. Gath, L. Bousset, B. Habenstein, R. Melki, A. Böckmann, and B. H. Meier. Unlike twins: An NMR comparison of two alpha-synuclein polymorphs featuring different toxicity. *PLoS One*, 9(3):e90659, 2014.

[117] K. Tenidis, M. Waldner, J. Bernhagen, W. Fischle, M. Bergmann, M. Weber, M. L. Merkle, W. Voelter, H. Brunner, and A. Kapurniotu. Identification of a penta- and hexapeptide of islet amyloid polypeptide (IAPP) with amyloidogenic and cytotoxic properties. *J. Mol. Biol.*, 295(4):1055–1071, 2000.

[118] H. LeVine III. Quantification of beta-sheet amyloid fibril structures with Thioflavin T. *Methods Enzymol.*, 309:274–284, 1999.

[119] S. Xu. Aggregation drives "misfolding" in protein amyloid fiber formation. *Amyloid*, 14(2):119–31, 2007.

[120] J. M. Berg, J. L. Tymoczko, and L. Stryer. *Biochemistry*. Freeman, W. H., 5th edition, 2002.

[121] T. Bauer, C. Dotta, L. Balacescu, J. Gath, A. Hunkeler, A. Böckmann, and B. H. Meier. Line-broadening in low-temperature solid-state NMR spectra of fibrils. *J. Biomol. NMR*, 67(1):51–61, 2017.

[122] P. Güntert. Automated protein structure determination from NMR data. In A. J. Dingley and S. M. Pascal, editors, *Biomolecular NMR Spectroscopy*. IOS press, Amsterdam, Netherlands, 2011.

[123] R. Tycko. Solid-state NMR studies of amyloid fibril structure. *Annu. Rev. Phys. Chem.*, 62:279–99, 2011.

[124] E. G. Hutchinson and J. M. Thornton. A revised set of potentials for beta-turn formation in proteins. *Protein Sci.*, 3(12):2207–2216, 1994.

[125] E. Andreetto, E. Malideli, L. M. Yan, M. Kracklauer, K. Farbiarz, M. Tatarek-Nossol, G. Rammes, E. Prade, T. Neumüller, A. Caporale, A. Spanopoulou, M. Bakou, B. Reif, and A. Kapurniotu. A hot-segment-based approach for the design of cross-amyloid interaction surface mimics as inhibitors of amyloid self-assembly. *Angew. Chem. Int. Ed. Engl.*, 54(44):13095–100, 2015.

Abbreviations

aa Amino acid

AFM Atomic force microscopy

DNP Dynamic nuclear polarization

DREAM Dipolar recoupling enhanced by amplitude modulation

EM Electron microscopy

HFIP Hexafluoroisopropanol

IAPP Islet Amyloid Polypeptide, Amylin

INEPT Insensitive nuclei enhanced by polarization transfer

IPTG Isopropyl β-D-1-thiogalactopyranoside

MAS Magic Angle Spinning

PDSD Proton-driven spin diffusion

RP-HPLC Reversed-phase high performance liquid chromatography

ssNMR Solid-state nuclear magnetic resonance

TEASE Ten amino acid extensive and selective labeling

Conference abstracts

2014, Solid state NMR on recombinant fibrillar human islet amyloid polypeptide for site specific assignments. Franziska Weirich, Ewa Mirecka, Lothar Gremer, Wolfgang Hoyer, Henrike Heise. Symposium **talk**. bio-N^{3}MR Netzwerk NRW, Annual meeting 2014, Universität Duisburg-Essen.

2014, Solid state NMR on recombinant fibrillar human islet amyloid polypeptide for site specific assignments. Franziska Weirich, Ewa Mirecka, Lothar Gremer, Wolfgang Hoyer, Henrike Heise. Conference **poster** presentation. 36th FGMR Discussion Meeting of GDCh, Berlin, Germany.

2016, The beta-sheet core of recombinant fibrillar human IAPP includes the centrail FGAILS segment. Franziska Weirich, Ewa Mirecka, Lothar Gremer, Wolfgang Hoyer, Henrike Heise. Conference **poster** presentation. EUROMAR, Aarhus Denmark.

2016, The beta-sheet core of recombinant fibrillar human IAPP includes the centrail FGAILS segment. Franziska Weirich, Ewa Mirecka, Lothar Gremer, Wolfgang Hoyer, Henrike Heise. Conference **talk**. 38th FGMR Discussion Meeting of GDCh, Düsseldorf, Germany.

2017, Structural characterization of recombinant fibrillar Islet Amyloid Polypeptide by solid-state NMR. **Poster presentation**. Symposium *Biophysics of Amyloid Formation* at university of Ulm. Ulm, Germany.

Internship 2015, 2 weeks in Motomasa Tanaka lab, Riken Brain Sciene Institute, Wako, Saitama, Japan.

Danksagung

Meinen besonderen Dank möchte ich an an Frau Prof. Dr. Henrike Heise für das entgegengebrachte Vertrauen und die Möglichkeit, meine Dissertation in ihrer Gruppe durchzuführen, aussprechen.

Zudem möchte ich Herrn Dr. Manuel Etzkorn für die Übernahme der Mentorenschaft und die Zweitkorrektur meiner Dissertation danken.

Ein besonderer Dank geht an Herrn Dr. Rudolf Hartmann für seine Geduld und seine Unterstützung bei allen Fragen bezüglich des Spektrometers.

Besonders danken möchte ich auch Herrn Dr. Lothar Gremer für seine Unterstützung im Labor, seine Ideen und für die Möglichkeit des Austauschs über das Projekt.

Zudem danke ich Herrn Dr. Wolfgang Hoyer für seine fachliche Unterstützung und seine Impulse zur Gestaltung des Projektes.

Ebenso möchte ich mich auch bei meinen direkten Kolleginnen und Kollegen, Anna Köning, Boran Uluca, Claudia Beumer, Daniel Schölzel, Haohong Pei und Timo Piechatzek bedanken. Sie haben mich fachlich und persönlich über den gesamten Zeitraum sehr unterstützt.

Besonders danken möchte ich auch Frau Dr. Ewa A. Mirecka, die mich zu Beginn meiner Promotion im Labor sehr unterstützt hat und mir viel Wissen vermittelt hat.

Ein herzlicher Dank geht an Frau Elke Reinartz für ihre Unterstützung im Labor.

Zuletzt gilt mein besonderer Dank meiner Familie für die durchgehende Unterstützung während der gesamten Erarbeitung der Dissertation.

Eidesstattliche Erklärung

Ich versichere an Eides Statt, dass die Dissertation von mir selbständig und ohne unzulässige fremde Hilfe unter Beachtung der „Grundsätze zur Sicherung guter wissenschaftlicher Praxis an der Heinrich-Heine-Universität Düsseldorf“ erstellt worden ist.

Ferner erkläre ich, dass ich in keinem anderen Dissertationsverfahren mit oder ohne Erfolg versucht habe, diese Dissertation einzureichen.